Alma Mater Studiorum – Università di Bologna

DOTTORATO DI RICERCA IN

CHIMICA

Ciclo XXVIII

Settore Concorsuale di afferenza: 03/C2

Settore Scientifico disciplinare: CHIM/04

UP-GRADE OF CATALYSTS FOR MEDIUM AND HIGH TEMPERATURE WATER GAS SHIFT REACTION

Presentata da: Molinari Chiara

Coordinatore Dottorato	Relatore
Prof. Aldo Roda	Prof. Angelo Vaccari

Esame finale anno 2017

Key Words

Water Gas Shift

Medium-High temperature

Cu/Zn/Al

La-Ce-Zr

Mg-Ba

Methylamines

Ga

Abstract

The Water Gas Shift (WGR) reaction plays a fundamental role in the production of H_2 or syngas, which are widely used in the chemical industry to produce building blocks or fuels. Considering the very large global request of these molecules, each improvement in the WGS processes generates a huge return on investment for the industries and for this reason, this reaction is still under investigation.

This PhD thesis aimed to upgrade the Medium and High Temperature Shift process by improving the catalytic formulations or finely tuning the reaction conditions. For the MTS formulations, the introduction of small amounts of elements such as La, Zr and Ce resulted in a significant improvement of the physical properties, with a corresponding increase, especially in case of Ce, of the CO conversion and the catalyst stability. On the other hand a small amount of Mg increases the stability and the catalytic performances, while the same amount of Ba does not affect the catalytic behavior. Finely, the role of the different reaction parameters on the methylamine formation and, consequently, on the deactivation by carbonaceous deposits was proposed.

Novel catalyst formulations were successfully obtained also in case of HTS, favoring the economic items of this process, with a strong increase of CO conversion and very low deactivation with time-on-stream by addition of very small amounts of Ga. This effect was attributed to the tendency of Ga to favor the formation of spinel-type phases that stabilized the metallic copper, resulting in a decrease in particle sizes. The high stability of Cu- and Ga-containing spinel-type phases and their controlled reduction are the key factors to favor the catalytic activity and reduce the copper sintering, main cause of catalyst deactivation.

Summary

Aim of the work

In the international industrial and energetic scenery, the market of hydrogen plays a crucial role. Considering the very high amount of H_2 consumed in the industrial applications, not only as pure H_2 but also together with different amount of CO to form different syngas formulations, it appears clear that the optimization of the existing processes is fundamental from an economic point of view. Starting from the reforming outlet stream, that represents the main way to produce H_2, it remains crucial the Water Gas Shift reaction, that allows to modulate the H_2/CO ratio or to the production of pure H_2 as a function of catalyst formulations and reaction conditions. In this scenario, the optimization of WGS step in the global chain of H_2 production results economically favorable. The optimization of WGS process may be realized by: 1) modulating the formulations of existing catalysts to work in the same conditions; 2) providing new formulations with increased performances in terms of stability and productivity; 3) studying new catalysts able to work at different conditions favorable to the reduction of energy costs.

With this premise, the present PhD work aims to realize the implementation of WGS process acting on the catalytic formulation and opportunely adjusting the reaction conditions. The main topics on which the present work aims to focalize the attention are the Medium and High Temperature Shift. The study is realized analyzing in depth the main problems of the two above mentioned shift processes, first modifying the formulation of MTS catalysts, with particular attention to deactivation phenomena, then introducing opportune dopants to the HTS catalysts in order to propose an alternative to the current industrial catalysts.

1 Introduction

The hydrogen production play an important role in the industrial processes and energy economy, used as energy carrier for fuel cell applications [1].

Hydrogen is an abundant element and it can be found in many substances in nature (i.e. hydrogen sulfide, fresh water, biomass and fossil fuels) [2, 3].

It is an important chemical, fundamental in many crucial industrial processes (manufacturing of plastics, foods, fertilizers, synthetic fuels, metallurgical procedures etc) [4]. In fact, despite the increasing use for energy applications, the main part of the hydrogen production is employed in the industrial processes.

At present, the majority of hydrogen is produced by fuel processing. Fuel processing technologies convert a hydrogen containing material into a hydrogen rich stream.

Nearly 96% of the hydrogen is derived from fossil fuels, with natural gas used with an estimated 49%, followed by liquid hydrocarbons at 29%, 18% from coal, and about 4% from electrolysis and other by-product sources of hydrogen [5]. Ideally, from an ecological perspective, hydrogen should be generated through electrolysis of water, using energy from renewable resources, preferably solar or wind energy.

On the contrary, because of the low cost and wide availability of fossil fuels, the rout via reforming reaction is now the cheapest.

The environmental success for hydrogen production route will only be possible if carbon dioxide is sequestered safely and economically.

Steam reforming of coal and natural gas are two major methods for producing large volumes of hydrogen. Hydrogen produced by these two methods is used mainly in the production of ammonia and methanol. In fact, ammonia, petroleum refining, and methanol are the three largest individual markets for hydrogen.

Refineries are large-volume producers and consumers of hydrogen for distillate. In general, environmental regulations implemented in most industrialized countries result in increased hydrogen requirements at refineries for gasoline and diesel desulfurization because of increased demand for cleaner fuels and tighter engine manufacturer specifications.

Overall global demand for hydrogen is expected to increase by around 5-6% during the next five years, primarily as a result of demand from petroleum refinery operations, and the production of ammonia and methanol.

Furthermore, considering the transition period toward hydrogen economy, hydrocarbon fuels remain an important source of hydrogen also for energy application.

The current world primary energy supply [4], is majorly based on fossil fuels. The use of fossil feed-stocks for process heat and electricity generation creates an environmental un-balance. In fact, in addition to deplete the oxygen from the atmospheric air, it is an unsustainable economy, which can lead to an irreversible environmental impact. Therefore, the world economy is increasingly focused on the reduction of CO_2 emissions and tackled the limited and unstable supply of fossil fuels by prioritizing the diversification of energy resources. Furthermore, the world dependence on conventional fossil fuels resources, which are mostly concentrated in Asia, is a source of geopolitical conflicts and is should be a problem for the access of future generation to a convenient energy supply and a clean and healthy environment [3].

The global energy landscape is changing quickly as a result of economic shifts and technological advancements. "Game-changers" such as the unconventional oil and gas revolutions, or the rapid retreat from nuclear power in some countries, will further accelerate this change.

Recent years showed an increase of the energy production starting from non-fossil feedstock but the total primary energy supply (TPES) is still dominated by fossil fuels as energy sources (Figure 1.1, Figure 1.2).

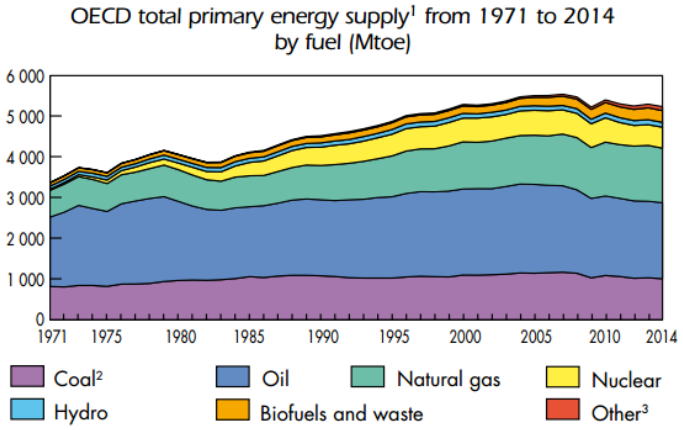

Figure 1.1 Trend of the Total Primary Energy Supply of the OECD members from 1971 to 2015 by fuel (Mtoe) (defined as energy production plus energy imports, minus energy exports, minus international bunkers, then plus or minus stock changes) [6].

The amount of fossil fuel came to about 80% in 2014, with an oil contribution of 35.7 % (Figure 1.2). Moreover, oil is the most versatile of the fossil fuels, with high energy density and ease of transportation.

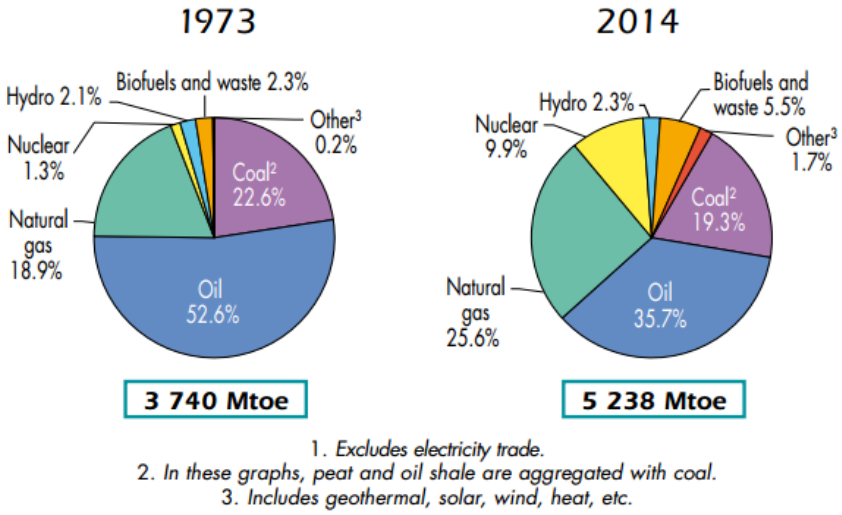

Figure 1.2 The 1973 and 2015 fuel shares of TPES [6].

From this data it is clear that, from industries there is a high interest in the improving of the existent industrial processes, in order to maximize the hydrogen production reducing both costs and environmental impact.

1.1 Water Gas Shift reaction

The Water Gas Shift reaction (WGSr) is traditionally used for the production of hydrogen from synthesis gas, further used for ammonia production and in petroleum refineries for a variety of operations. The earliest industrial process dates back to 1888 [7] and its prominence came with the Haber ammonia synthesis process and development of catalyst by Bosch and Wilde in 1912 [8]

The WGS reaction is an important step in the hydrogen production in the steam reforming process (Figure 1.3 [9]), the most important hydrogen production pathway. Depending on the use of the gas stream, it is used to remove the remaining CO or to to increase the H_2 content for Fisher-Tropsch or other reactions [8].

It consist in the oxidation of CO by steam to obtain H_2 (reaction 2.1).

$CO + H_2O \rightleftarrows CO_2 + H_2$ ΔH = -41.2 Kj/mol (reaction 2.1)

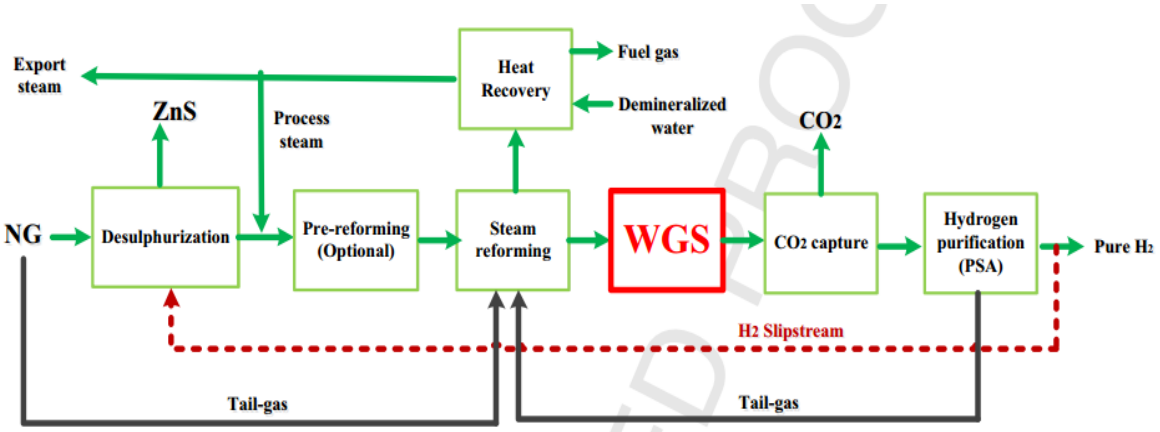

Figure 1.3 Steam reforming of natural gas [9].

1.2 Thermodinamic

The reaction is moderately exothermic with an equilibrium constant that favor the conversion at low temperature. The effect of the temperature on the reaction can be illustrated by the decrease and sign change of the Gibbs free energy and the decreasing of the equilibrium constant by increasing of the temperature (Figure 1.4).

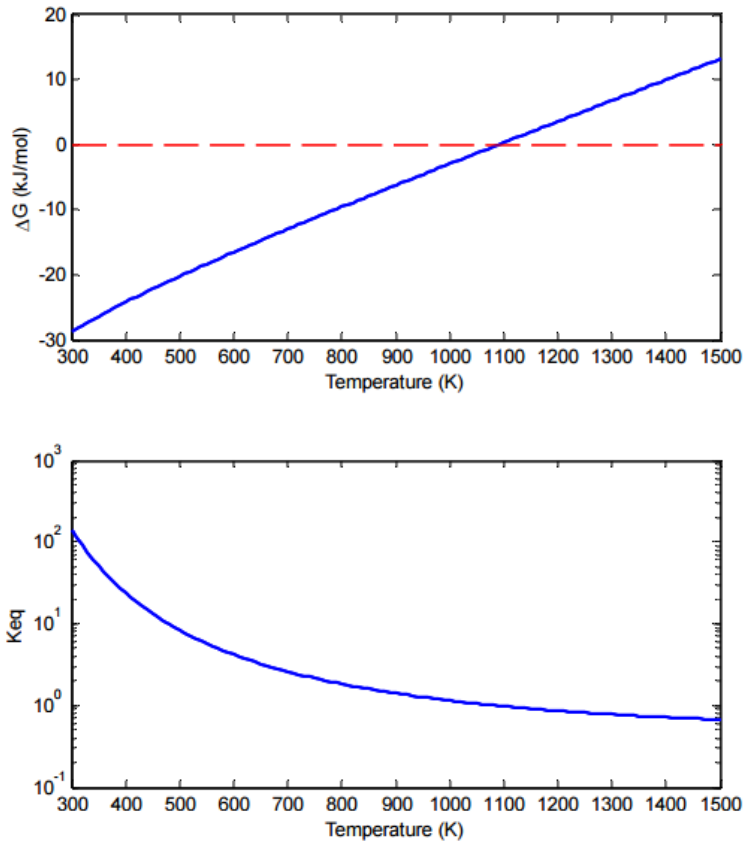

Figure 1.4 Thermodynamic equilibrium of the WGS reaction as described by the Gibbs free energy change and the equilibrium constant of the reaction as function of temperature [10].

The equilibrium constant can be derived using different equations.

Equation a is formulated taking into account the thermodynamic properties. Equation b is the Marschner e Moeller equation, calculated with correlation for fugacity coefficients of carbon monoxide and carbon dioxide in a gas mixture (11).

Furthermore, it can also be described with a simpler model, like proposed by Moe (Equation c [12]).

$$K_{eq} = e^{(Z(Z(0.63508-0.29353Z)+4.1778)+0.31688} \quad \text{(Equation a)}$$

where $Z = \left(\frac{1000}{T}\right) - 1$

$$Ln(K_{eq}) = \frac{5693.5}{T} + 1.077\ln T + 5.44 * 10^{-4}T - 1.125 * 10^{-7}T^2 - \frac{49170}{T^2} - 13.148 \quad \text{(Equation b)}$$

Considering that; $Keq \sim \frac{P_{CO_2} * P_{H_2}}{P_{H_2O} * P_{CO}}$

$$K_{eq} = e^{\frac{4577.8}{T} - 4.33} \quad \text{(Equation c)}$$

In Figure 1.5 is plotted the CO equilibrium concentration as a function of temperature and the inlet composition with different inlet steam contents [13].

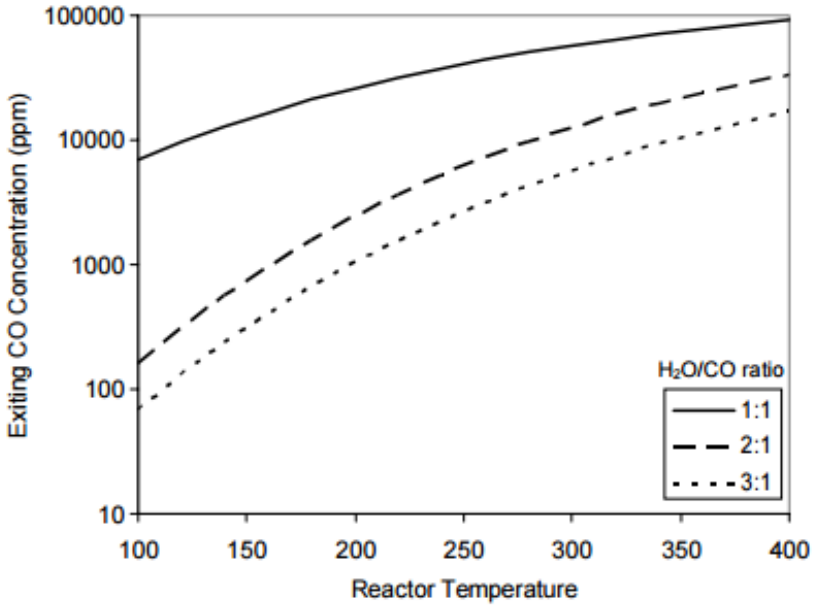

Figure 1.5 CO exiting concentration for equilibrium conversion of water gas shift reaction with various inlet H_2O/CO mole ratios, 1 atm, feed H_2/CO = 2.0 [13].

Considering that the reaction is equimolar, the equilibrium is virtually unaffected by pressure variations under industrial conditions (P = 0.1– 5.0 MPa) [14]. The use of higher pressures lead to increases the reaction rate, allowing for the use of smaller reactors. In industrial applications contact time is generally 3-9 s under normal pressures, but may be around 1 s for higher operation pressures [15].

An important increase in the steam respect to the stoichiometric value give rise to a higher CO conversion.

1.3 Industrial configurations

Starting from the thermodynamic considerations, in order to improve the performances of the shift unit plant, industrial plants can be divided in two different configurations.

1.3.1 Two step configuration

The most used is a two-bed configuration, which involves two reactors operating at different temperature (Figure 1.6 and Figure 1.7).

The high temperature of the gas stream, using an adiabatic single bed reactor, the exothermicity of the reaction limits the possible CO conversion.

The thermodynamic limitations can be reduced by using of a second catalytic bed at lower temperature, with inter-stage cooling to obtain higher conversions and to achieve carbon monoxide level lower than 1% [8].

Generally, in industrial applications, it can be identified a first step at higher temperature. A High Temperature shift (HTS) reaction is conducted as first stage with a temperature range of 350°C-600°C. The inlet temperature must be maintained at about 350°C in order to achieve an adequate reaction rate [14]. For this application, the catalyst used consists of magnetite crystallites with the addition of chromium oxide to improve the thermal stability [8]. Doping catalyst (with Cu, Rh, V etc.) could reduce the effect of side reactions. Iron based catalysts needs high S/C ratio in order to avoid the reduction of the active phase (magnetite to metallic iron), that should catalyze Fischer-Tropsch reaction and carbon formation.

Furthermore, the presence of Cr should give the formation of CrO_3.

The second stage, named Low Temperature shift (LTS) occurs with a temperature range of 150°C to 300°C. Cu-based catalysts are employed in the LTS, because of the

conventional Fe-based catalysts are not active enough. CO concentration in the outlet gas of 0.1-0.3% is reached.

This kind of catalyst, that generally content about 30% of Cu, undergo to sintering phenomena because of the relatively low melting temperature of the metal (1084,62°C) [10].

To reduce the temperature for the LTS reactor, it is necessary to cool the process gas from the first stage. Inter-bed cooling step is usually achieved by heat exchange, which may be used to heat boiler feedwater or to rise steam [8].

The best results can be obtained using the lower possible temperature at the inlet of the second reactor, in general correlated to the dew-point [8].

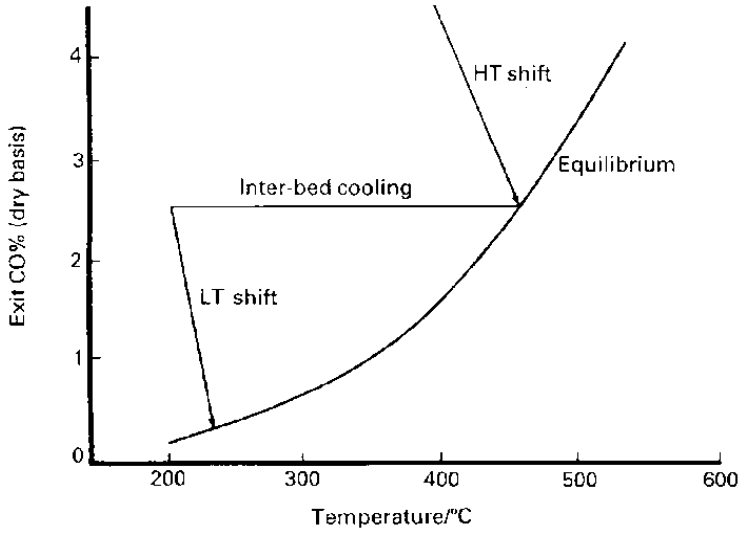

Figure 1.6 Typical variations of CO levels in HTS and LTS catalyst bed [8].

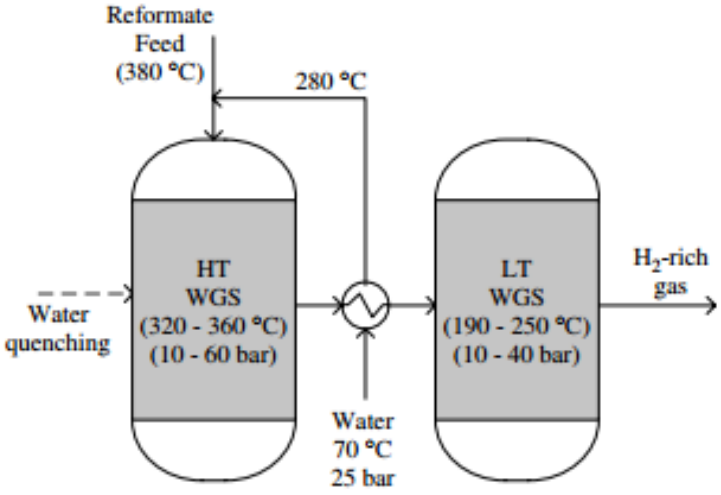

Figure 1.7 Conventional two-stage process diagram of the WGS reaction unit [16].

1.3.2 One step configuration

To optimize the plant efficiency it also possible to use only one-step at medium temperature in place of the two-step configuration, named Medium Temperature Shift (MTS), with a temperature range of 300-350°C. Advanced MTS catalysts offer benefits in achieving incremental hydrogen (lower CO-slip).

This set of the plant show other several advantages in terms of plant configuration and problems correlated to the use of the catalysts [17]:

- Only one reactor is required.
- Use of catalysts without chromium.
- A lower S/C ratio in the reformer can be used avoiding sintering and Fisher-Tropsch-side reactions.
- No bypass control in the Process Gas (PG) boiler is needed; this control is prone to metal dusting problems.

1.4 Mechanism and kinetic

Because of the industrial importance of the WGS reaction, many researchers have investigated the mechanism involved. From the discovery that the reaction may be catalyzed by a number of metal a lot of studies have been carried out attempting to identify the elementary steps involved in the process and to develop models to try to explain the behavior observed with the different catalysts.

Regardless the number of publications, nowadays a wholly satisfactory and universally accepted mechanistic description of the WGS reaction fails to exist for all the catalysts. In fact although the reaction is not complex the catalysts behaviors are susceptible to small changes in operating conditions and this complicates the study of this process.

The results of several of these investigations suggest that the WGS reaction largely occurs via four specific mechanisms:

1) The redox mechanism [18,19,20 ,21,22,23,24,25].

2) The formate mechanism [20, 24, 26, 27, 28].

3) The associative mechanism (or Langmuir-Hinshelwood mechanism) [7, 29, 30].

4) The carbonate mechanism [21,31,32,33].

1.4.1 The redox mechanism

The redox mechanism implies the oxidation of the reactive surface site by H_2O forming H_2; then the oxidized site is involved in the oxidation of CO to CO_2.

S represents the surface site.

$H_2O + S \rightleftarrows O{\cdot}S + H_2$

$O{\cdot}S + CO \rightleftarrows CO_2 + S$

A two-step redox mechanism is was proposed by Temkin [23]. His work has been focused on the HTS reaction using a Cr_2O_3-Fe_2O_3. In this mechanism the key surface intermediate is the adsorbed atomic oxygen. From the experimental results, the forward reaction rate was determined:

$$r = \frac{kP_{CO}P_{H_2O}}{\chi P_{H_2O} + P_{CO_2}}$$

where *k* and χ are temperature dependent constants.

$$log\chi = -\frac{8800}{4.57T} + 2.31$$

$$logk = -\frac{3400}{4.57T} + 10.3$$

The same rate equation was experimentally validated in LTS reaction using a ZnO-Cr_2O_3-CuO, suggesting that the mechanism is the same for both conditions.

In the case of LTS χ and *k* have different correlations with the temperature.

$$\chi = 2.5 * 10^9 \exp\left(-\frac{21500}{R_{gas}T}\right)$$

$$k = 6.0 * 10^{11} \exp\left(-\frac{26800}{R_{gas}T}\right)$$

Nakamura, et al. [18] studied the kinetics and mechanism of the reaction on Cu(110) in comparison with Cu(111). They have defined a different mechanism, reported below.

The adsorbed hydroxyl groups dissociate to O·S and the adsorbed atomic oxygen reacts with CO to produce CO_2 rather than produce surface formate. The hydroxyl dissociation

to water and adsorbed atomic oxygen occurs rapidly, thus resulting in the redox mechanism.

$H_2O + S \rightleftarrows H_2O{\cdot}S$

$H_2O{\cdot}S + S \rightleftarrows HO{\cdot}S + H{\cdot}S$

$2HO{\cdot}S \rightleftarrows H_2O{\cdot}S + O{\cdot}S$

$HO{\cdot}S + S \rightleftarrows O{\cdot}S + H{\cdot}S$

$2H{\cdot}S \rightleftarrows H_2 + 2S$

$CO + S \rightleftarrows CO{\cdot}S$

$CO{\cdot}S + O{\cdot}S \rightleftarrows CO_2{\cdot}S + S$

$CO_2{\cdot}S \rightleftarrows CO_2 + S$

Ovesen, et al. [19, 20] proposed a redox mechanism, considering an 8-step mechanism and excluding the formation of formate species. The water dissociation and the oxidation of CO were both plausible rate-limiting steps. The redox mechanism needs the complete surface dissociation of H_2O to adsorbed atomic oxygen and hydrogen to combine with CO to form CO_2.

The increase of pressure lead to obtain the formate intermediate. Surface studies suggested that formate formation may be include into the mechanism via the reactions:

$CO_2{\cdot}S + H{\cdot}S \rightleftarrows HCOO{\cdot}S + S$

$HCOO{\cdot}S + H{\cdot}S \rightleftarrows H_2COO{\cdot}S + S$

$H_2COO{\cdot}S + 4H{\cdot}S \rightleftarrows CH_3OH_{(g)} + H_2O_{(g)} + 5S$

Askgaard, et al [26] indicated that the third reaction is not very important because of the low coverage of $H_2COO{\cdot}S$. Ovesen, et al [20] suggested that, in the 11-step mechanism, formate is a “dead end” reaction. In fact, regardless it may be found on the catalyst surface, it do not participate into the conversion of CO to CO_2, furthermore blocking the active sites. The rate of reaction may then be written as an algebraic expression in terms of the partial pressure of reactants, products, equilibrium constants and rate constants.

1.4.2 The formate mechanism

In the formate mechanism, correlated to the redox mechanism, adsorbed water dissociates into an adsorbed hydroxyl group and adsorbed atomic hydrogen. Then the OH

group combines with adsorbed CO to form adsorbed formate. The decomposition of formate gives rise to the formation of CO_2 and H_2.

$H_2O{\cdot}S + S \rightleftarrows HO{\cdot}S + H{\cdot}S$

$CO{\cdot}S + OH{\cdot}S \rightleftarrows HCOO{\cdot}S + S$

$HCOO{\cdot}S + S \rightleftarrows CO_2{\cdot}S + H{\cdot}S$

In their work Campbell and Daube [24], performing experiments on a single Cu crystal within a micro-reactor studied the formate mechanism, identifying the elementary reactions reported below.

$CO + S \rightleftarrows CO{\cdot}S$

$H_2O + S \rightleftarrows H_2O{\cdot}S$

$H_2O{\cdot}S + S \rightleftarrows OH{\cdot}S + H{\cdot}S$

$CO{\cdot}S + OH{\cdot}S \rightleftarrows HCOO{\cdot}S + S$

$HCOO{\cdot}S \rightleftarrows CO_2 + H{\cdot}S$

$2H{\cdot}S \rightleftarrows H_2 + 2{\cdot}S$

Results suggest that the WGS reaction may occur on an oxygen-free surface and that water both adsorbs and desorbs molecularly on a clean copper surface. Furthermore, CO and H_2O coverages are very low under reaction conditions, resulting in a rate of the reaction nearly independent to the partial pressure of CO, while it shows a strong increase with the partial pressure of H_2O. This result may be explained by the inclusion of a hydroxyl intermediate formed from the dissociation of adsorbed water. It can be derived that the dissociation of water into OH and H adsorbed groups is the rate-limiting step. The surface hydroxyl groups react with adsorbed CO forming the formate intermediate. The kinetics is modified by the increase of the pressure; in fact, working at high pressure the rate-determinant step is the decomposition of formates. They also noted that in presence of adsorbed oxygen the reaction may be enhanced the WGS reaction by a different reaction path-way:

$H_2O{\cdot}S + O{\cdot}S \rightleftarrows OH{\cdot}S + OH{\cdot}S$

They considered a surface redox mechanism in which the OH·S produced in step 3 of the formate mechanism further dissociates into O·S and H·S. Then the O·S may react with adsorbed CO following the reaction reported below.

$CO{\cdot}S + O{\cdot}S \rightleftarrows CO_2 + 2S.$

Also in this mechanism the step 3 may be identified as the rate-limiting step.
Considering the different path ways reported in literature for the formate mechanism, a global scheme of the single reaction steps is reported in (Figure 1.8).

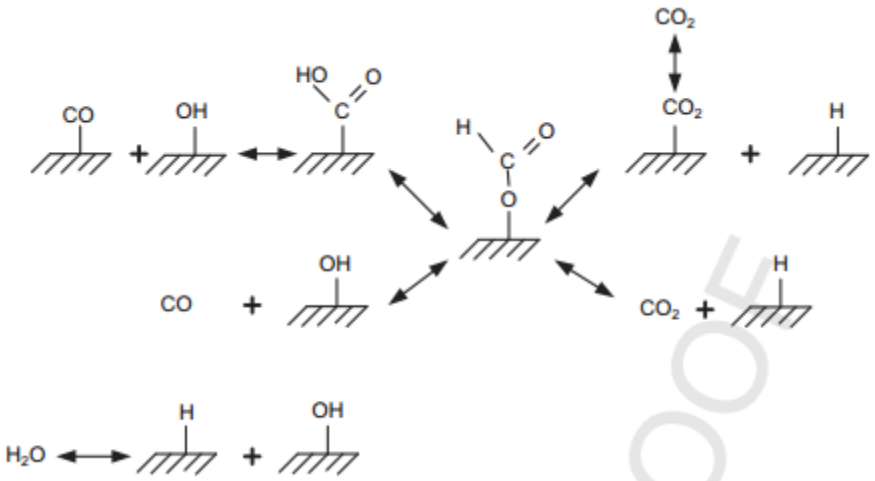

Figure 1.8 Water–gas shift mechanism via formate intermediate [9].

Campbell and Daube [24] have used the analytical expression proposed earlier by Van Hewijnen and De Jong [28] to correlate and predict their experimental results accurately. Van Hewijnen and De Jong have worked to evidence the formate mechanism studying the forward and reverse WGS reactions. They started analyzing different kinetics models identified by other groups, reported in Table 1.1.The Van Hewijnen and De Jong equation, based on the results feeding only CO and H_2O, showed that the rate has a low dependence on feed composition at low temperature, while at higher temperatures the maximum rate can be observed with lower feed concentration of water than at lower temperatures [34]. Shido and Iwasawa [26] studied the reverse WGS reaction to evidence the presence of formates on the catalyst surface and the elementary reaction steps involved. They observed that the water molecule adsorbed dissociates to hydroxyl group, which form the formate. Then the intermediate does not decompose to H_2 or CO_2 like Campbell and co-workers demonstrated [35]. The 70% of the formates gives OH and CO adsorbed group,

but then tend to reform formate. Only the remaining 30% decomposes into the desired products [27].

Research group	Rate equation
Campbell et al. [35]	$r = \frac{kP_{CO}P_{H_2O}}{\left(1 + K_1P_{CO} + K_2P_{H_2O} + K_3P_{CO_2} + K_4P_{H_2+}\right)^2}(1 - \beta)$
Moe et al. [12]	$r = kP_{CO}P_{H_2O}(1 - \beta)$
Shchibya et al. [36]	$r = \frac{kP_{CO}P_{H_2O}}{AP_{CO} + P_{CO_2}}(1 - \beta)$
Kul'kova-Temkin [37]	$r = P_{CO}\left(\frac{P_{H_2O}}{P_{H_2}}\right)^{\frac{1}{2}}(1 - \beta)$
Goodridge-Quazi [38]	$r = kP_{CO}^{a}P_{H_2O}^{b}P_{CO_2}^{c}P_{H_2}^{d}$
Van Hewijnen and De Jong [34]	$r = \frac{25.8 * 10^3 \exp(-16000/k_bT)P_{CO}P_{H_2O}}{1 + 127P_{CO}P_{H_2O} + 26P_{CO}}$

Table 1.1 Potential water-gas shift reaction rate expressions [34].

where: $\beta = \frac{P_{CO_2}P_{H_2}}{KP_{CO}P_{H_2O}}$

1.4.3 The associative or "Langmuir-Hinshelwood" mechanism

The associative mechanism is an adsorption–desorption model. It defines that CO_2 and H_2 are produced by the decomposition of an intermediate, that derive from the interaction of the two adsorbed species [19]. The aforementioned reaction is shown below.

$H_2O_{(g)} + CO_{(g)} \rightleftarrows$ intermediate $\rightleftarrows CO_{2(g)} + H_{2(g)}$

Many research groups studied this kind of mechanism, but actually the kind of intermediate is already no well defined. In fact no definitive evidence exists about the nature of the intermediate involved in the associative mechanism. Formate and carboxyl intermediates seem to be the leading candidates.

A Langmuir–Hinshelwood mechanism has been studied by Rhodes [7]. The reaction between either a hydroxyl species or water and CO produces a formate species. The

decomposition of the H_2O adsorbed on the surface leads to the formation of the hydroxyl intermediate, which may react with either adsorbed or gaseous CO_2 similarly to what observed in formate mechanism (Figure 1.8).

Grenoble et al. [39] suggested that formic acid was the intermediate for the process, considering that both reactants and products were obtained during the acid decomposition.

Ovesen et al. extended the eight-step redox mechanism to the associative mechanism, adding 3 extra steps to take into account the formate production [19]. In its studies Sun et al. [40] found that the best fitting of the Langmuir Hinshelwood model in WGS reactions is for precious metals. Keiski [41] studied the HTS WGS reaction using both steady state and transient techniques; he determined that the rate determining steps in the transient investigations were CO adsorption, CO_2 desorption and H_2 formation. Fishtik and Dutta [29] determined that at higher temperatures, the reaction was governed by the redox mechanism while the associative and formate mechanisms were significant in the low-temperature region.

For the adsorptive mechanism the rate expression may be derived from Yang–Hougen Table [42] when the surface reaction is the rate determining step.

The rate equation has been defined using experimental results [43,44].

$$r_{CO} = k\frac{P_{CO}P_{H_2O} - P_{CO_2}P_{H_2}/K_p}{(1 + K_{CO}P_{CO} + K_{H_2O}P_{H_2O} + K_{H_2}P_{H_2} + K_{CO_2}P_{CO_2}}$$

1.4.4 The carbonate mechanism

Besides the already discussed mechanisms, researchers have also proposed a carbonate mechanism.

Millar, et al. [25] have defined a carbonate mechanism on the basis of the experimental IR spectroscopy results performed on a Cu/SiO_2 catalyst. In fact, they observed a band corresponding to “symmetrical” carbonate ions on the catalyst surface.

The peaks observed support the ideas that CO oxidation on copper may proceed via a polydentate carbonate structure named “surface malachite type” species. The carbonate production increase the availability of surface carbonate forming formate species on the

surface. Lund, et al. [31, 32, 33] have investigated this mechanism, identifying the single reaction steps involved:

$CO + 2O{\cdot}S \rightleftarrows CO_3{\cdot}S_2$

$CO_3{\cdot}S_2 \rightleftarrows CO_3{\cdot}S + S$

$CO_3{\cdot}S \rightleftarrows CO_2 + O{\cdot}S$

$H_2O + S \rightleftarrows H_2O{\cdot}S$

$H_2O{\cdot}S + O{\cdot}S \rightleftarrows 2OH{\cdot}S$

$2OH{\cdot}S \rightleftarrows 2O{\cdot}S + H_2$

$H_2O{\cdot}S + S \rightleftarrows OH{\cdot}S + H{\cdot}S$

$2H{\cdot}S \rightleftarrows H_2 + 2S$

It may be noted that only steps from 1 to 6 are needed to describe the catalyst behavior. Steps 7 and 8 have been added by Lund to indicate a path for generating surface oxygen from steam.

The transition state theory was used to derive an expression for the rate of each elementary reaction step.

The rate equation defined by Lund, using Bohlbro's kinetic data [45] is reported below.

$$r_p = C_t \Lambda_\rho \exp\left(-\frac{E_p}{R_{gas}T}\right)\left[\underset{\sigma_\rho}{\rightarrow}\prod_{i=1}^{l} a_i^{\overrightarrow{-\nu_{\rho i}}} - \frac{\underset{\sigma_\rho}{\leftarrow}\prod_{i=1}^{l} a_i^{\overleftarrow{-\nu_{\rho i}}}}{\exp\left(\frac{\Delta S_\rho\,(T)}{R_{gas}}\right)\exp\left(\frac{\Delta H_\rho\,(T)}{R_{gas}T}\right)}\right]$$

$\underset{\sigma}{\rightarrow}$ and $\underset{\sigma}{\leftarrow}$ are geometric factors associated with the forward and reverse reaction, respectively.

1.4.5 Reaction mechanism: a function of reaction conditions

In order to model and predict the real behavior of the WGS reaction many researchers considered more general mechanisms, often comprising elementary reaction steps from the more recognized mechanisms. Even if the redox mechanism is accepted for the HTS catalysts, there is considerable uncertainty about the operative mechanism at low temperatures, over the Cu-based catalysts [7]. It depend to the ability of H_2O to re-oxidize the partially-reduced supported oxide at temperatures below 250 °C, especially in the presence of significant amounts of H_2, as the case of fuel cell applications [46]. The

fundamental difference between the redox and the associative mechanism is that in redox mechanism the oxidation of CO is carried out by adsorbed O atoms, while CO_2 is formed by the decomposition of an intermediate or by the reaction of this last one with an OH group.

Different mechanisms can be predominant on the same catalyst under different reactant concentration, temperature and pressure, especially in the WGS reaction that is equilibrium-limited at high temperature and kinetically limited at low temperature.

It is possible to hypothesize three situations in the reaction mechanism [47,48,49]:

- At low temperature, especially in presence of a substantial amount of CO_2 (very low Steam/CO_2 ratio), the carbonate decomposition is the rate-determining step.
- At intermediate temperature, especially in presence of a large concentration of H_2O (high S/CO_2 ratio), the formate decomposition step is slow and rate-determining.
- At high temperature, where desorption and/or decomposition of intermediates is very fast, the redox processes is expected to be predominant, mainly in the presence of a high concentration of H_2O (intermediate S/CO_2 ratio), when the surface is covered to a significant extent by OH groups.

From the studies performed by Ovesen et al. [19], considering the surface redox mechanism under industrial conditions and the Cu-based catalysts, the following conclusions have been achieved:

- at low pressure (0.1 MPa), hydrogen and hydroxide are the dominating intermediates;
- at high pressure (2.0 MPa), hydrogen and formates are the dominating intermediates.

1.5 Catalysts formulations

1.5.1 HTS catalysts

The HTS reaction is carried out at 350-400°C. Catalysts for HTS reaction have been used for more than 80 years and modified in order to optimize hydrogen efficiency in synthesis-gas production. The catalyst used for this application is generally a magnetite (Fe_3O_4, or

Fe(II)O $Fe(III)_2O_3$) based catalyst as active phase stabilized by the addition of cromia [8]. Pure magnetite is active in HTS conditions, but catalysts rapidly lose activity as a result of the reduction in surface area given by sintering phenomena [50].

The catalyst precursor is composed by hematite (Fe_2O_3) with 5-10% of cromia (Cr_2O_3) [51,52]. The active phase is obtained by partial reduction of Fe^{3+} to form the spinel phase. Cr^{3+} partial substitutes the Fe^{3+} in the octaedrical sites, with a distortion of the lattice that lead to an increase in the covalent behavior of the bond [53,54,55,56,57]. Experiments carried out on the ternary Fe–Cr–O system showed that the Cr^{3+} ions displaced equal amounts of Fe^{2+} and Fe^{3+} from the octahedral sites in the oxygen sub-lattice and that the displaced Fe^{2+} ions transferred to the tetrahedral sites to maintain charge balance [57].

After the doping an increase in the physical properties of the catalyst is observed [20] because of magnetite crystallites are stabilized by the addition of refractory oxide. Furthermore, Domka et al. [58] found that the surface area of the Cr-containing catalysts was higher respect to the non-Cr-containing one, also after reduction (8 m^2/g for the pure Fe_3O_4, 40 m^2/g for the Fe_3O_4/8 wt.% Cr_2O_3). Cromia concentration higher than 14 wt.% Cr_2O_3 gave rise to a further resistance to sintering, but it is followed by a lower activity [59]; in fact when the cromia concentration exceeded 14 wt.%, Cr_2O_3 may be found as discrete grains [60].

Chromium-stabilized catalysts can be used for 2–10 years before being substituted and its end may be indicated by a rise in pressure drop caused by catalyst breakage, an accumulation of deposits or, simply, by a decreased activity. Combined physical characterization and reactor studies of the Fe_3O_4/Cr_2O_3 catalysts [61,62] showed that deactivation was mainly given by sintering rather than poisoning or coking. The most important deactivation phenomena affect the first 150 h of use, followed by a low/rate deactivation period. The initial fast deactivation can be correlated to the sintering of the magnetite particles that are in contact. Further sintering then requires the modification of these Cr_2O_3 grains or the bulk transport of Fe_3O_4 which corresponds to the second, slower, activity reduction step.

The magnetite based catalysts are generally prepared by precipitation technique, starting from of an aqueous solution containing iron and modifier (Cr) salts by addition of a base [51]. Chlorides or sulphates are preferred because of the lower cost of the row materials [51**,** 53]. The base used is an alkali metal aqueous solution, like hydroxide or carbonate.

The precipitation is carried out at 30-80 °C with a pH of 6-9 and the precipitate is normally filtered, washed and dried. After filtration, it is very important to wash the precipitate in order to fully remove traces of sulphates; during the reduction, they may be converted to H_2S during reduction [8]. The iron based catalysts could also be prepared by coprecipitation method in microemulsion, leading to control the size and shape of nanoparticles [63].

The calcination temperate must remain under 200°C to avoid the oxidation of the magnetite, which can be directly co-precipitated during the synthesis [51]. Furthermore the oxidation must be carefully controlled to limit the formation of CrO_3 by oxidation of Cr_2O_3 [8].

$$2\ Cr_2O_3 + 3\ O_2 \rightarrow 4\ CrO_3$$

In addition Cr^{6+} are potential health hazard. Furthermore, the oxidation of Cr^{3+} is exothermic, increasing the temperature in the catalytic bed.

For these reasons, there is an interest in the development of Cr-free catalysts for HTS reaction, but nowadays the alternative systems shows problems like complex production process, high costs and introduction of new pollutant [64].

An interesting improvement in the Fe-based catalyst formulation is the addition of first row transition metal oxide as promoters. In particular Andreev et. al. [65] studied the effect of the addition of CuO, CoO and ZnO (5 wt%) on the CO conversion.

After doping, a higher activity at lower temperature was observed. Other studies evaluated the effect of the addition of Pb, Co, Mg, Zn [66,67].

In particular, the Cu doped catalyst showed the higher activity in the larger temperature range. If it is well defined that Cr^{3+} substitute Fe^{2+} in the octaedrical site in the spinel structure, instead Cu^{2+} does not [70]. In fact its stabilization energy, related to its higher electronegativity, lead to have weaker Cu-O bond respect to Fe-O bond. In Cr-free catalyst Cu tend to migrate in the surface , while with Cr it can be find no-uniformly distributed in the structure [68]. The presence of Cu crystals, already with a 5 wt%, seems to provide a similar reaction mechanism observed for the LTS cupper based catalysts [69]. At the same time, Quadro *et al.* [70] concluded that Cu acts as a structural promoter in Fe-based catalysts, whereas Cr leads to a decrease in the intrinsic activity.

The high activity obtained after Cu addition lead to use this systems in more severe industrial conditions with a larger operating flexibility. In fact it is possible to reduce the S/C ratio without the reduction of magnetite to metallic iron (and without hydrocarbon formation) [51,70], reduce the reactor volume and require a lower reaction temperature. On the contrary, the presence of Cu, incorporated in the Fe-containing phase, favor the sintering phenomena reducing the thermal stability.

The Fe–Al–Cu catalysts exhibited low stability when the copper content increased. Ni could substitute copper, since it has higher thermal stability at high temperatures and is active in WGS reaction [71]. Furthermore Ba-promoted Fe_2O_3–Al_2O_3–NiO catalyst shows low methanation activity in HTS conditions.

In order to be active in WGS reaction, Fe_2O_3 must be reduced to Fe_3O_4 [8]. The reduction is carried out using directly process gas, having care to avoid a further reduction to metallic iron, which promotes methanation, which could give rise to a dangerous temperature Runaway, and CO disproportionation (Boudouard's reaction) [8,10,14,72]. The undesired reductions that should be catalyzed by Fe^0 are reported below.

$2CO \rightleftarrows C + CO_2$

$CO + H_2 \rightleftarrows C + H_2O$

$CO_2 + 2H_2 \rightleftarrows C + 2H_2O$

$2CO + 2H_2 \rightleftarrows CO_2 + CH_4$

$CO + 3H_2 \rightleftarrows CH_4 + H_2O$

$CO_2 + 4H_2 \rightleftarrows CH_4 + 2H_2O$

$C + 2H_2 \rightleftarrows CH_4$

$4CO + 2H_2 \rightleftarrows CH_4 + 3CO_2$

$CH_4 + 2CO \rightleftarrows 3C + 2H_2O$

$CH_4 + CO_2 \rightleftarrows 2C + 2H_2O$

The formation of carbon blocks the catalyst sites causing catalyst deactivation and an increase in the pressure drop across the bed caused by plugging or fouling of the reactor. The formation of methane may consume hydrogen and alter the product composition causing potential difficulties in subsequent processes.

Generally, in industrial applications, the over-reduction of Fe_2O_3 is avoid by using a high Steam/Dry Gas ratio, increasing the operative costs correlated to the production and the condensation of the unconverted steam [70].

From the H_2-TPR analysis [73] it is possible to observe a peak at 400 °C, attributed to the reduction of Fe_2O_3 to Fe_3O_4 (390-430 °C) and Cr_2O_3 to CrO (385°C). A broad peak at higher temperatures (500-900 °C) is related to the reduction of Fe_3O_4 to Fe, via FeO. In the HTS process the active phase is obtained by partial reduction at 400 °C [73,78].

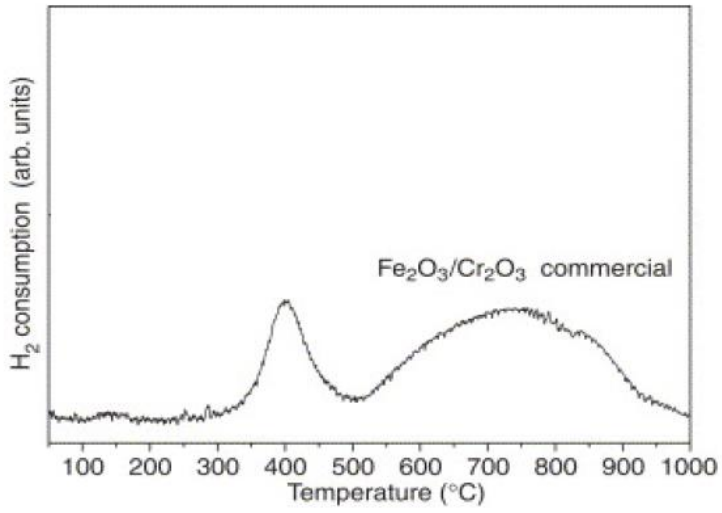

Figure 1.9 H_2-TPR profiles for a Fe_2O_3/Cr_2O_3 commercial catalyst [73].

The heat of the reduction of the catalyst depends on the H_2/CO ratio of the gas, as it is possible to see in the equation reported below. The reduction of the Fe_2O_3 is less exothermic respect to that of CrO_3 .

In order to avoid the magnetite reduction, the Steam/H_2 and CO_2/CO ratios must be optimized [8]; at 450 °C, the gas in equilibrium with the two phases contains 96.0 % H_2O and 4.0 % H_2, 99.5% CO_2 and 0.5% CO.

$3\ Fe_2O_3 + H_2 \rightarrow 2\ Fe_3O_4 + H_2O$ $\quad \Delta H^0_{298} = -16.3\ kJ\ mol^{-1}$

$3\ Fe_2O_3 + CO \rightarrow 2\ Fe_3O_4 + CO_2$ $\quad \Delta H^0_{298} = +24.8\ kJ\ mol^{-1}$

$2\ CrO_3 + 3H_2 \rightarrow Cr_2O_3 + 3\ H_2O$ $\quad \Delta H^0_{298} = -684.7\ kJ\ mol^{-1}$

$2\ CrO_3 + 3\ CO \rightarrow Cr_2O_3 + 3\ CO_2$ $\quad \Delta H^0_{298} = -808.2\ kJ\ mol^{-1}$

In the range of 300-565 °C Fe_3O_4 is stable but at 400 °C if the S/H_2 ratio exceeds 0.09 or the CO_2/CO ratio exceeds 1.16, while at 550 °C these ratios are 0.28 and 1.00. Under some conditions, further unwanted reduction of Fe active phase may occur. If the reduction

capacities are higher, an over-reduction should be occurs. Above 565°C FeO is the stable phase. The effect of the S/H_2 ratio and temperature on the stable phase composition in the iron/iron oxide system is shown in Figure 1.9 [72].

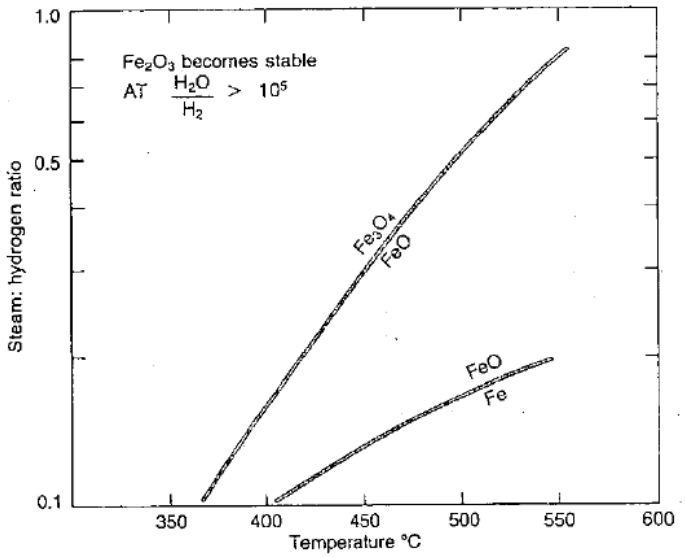

Figure 1.10 Minimum Steam/H_2 ratio for the reduction of conventional HTS catalysts [72].

Pure H_2 or H_2-rich mixtures must not be used for the reduction of the catalysts, to avid the iron formation.

Fe-based catalysts show a high resistance to poisoning phenomena. Considering plants for steam reforming of hydrocarbons, primary reforming and LTS step are more poison-susceptible, so generally the gas streams inlet at the HTSr are virtually poison-free.

However, if hydrogen sulphide is present in the process gas in large amount this will not seriously affect activity of the HTS catalyst which, depending on the concentration of the hydrogen sulphide, may being sulphide [8].

HTS catalysts can be affected by halides, but they are rarely encountered at sufficiently high level to cause major problems.

Sintering of iron based catalysts, the main cause of deactivation, lowers the surface area, reducing porosity and increasing the particle size. In particular it decreases the number of pores smaller than 30 nm which mostly contribute to the shift reaction [74]. Also arsenic compounds, phosphorous compounds or silica in small concentrations could causes deactivation of iron catalysts.

An interesting alternative to the traditional iron-based system in the HTS reaction, is the use of noble metals.

Platinum group metals (PGM) are very attracting. These catalysts are generally supported upon ceria [75,76]. Neither ceria nor PGM metals alone (e.g. deposited on silica or alumina) have important activity in WGS [63]. Pt/CeO_2 catalysts show 15 times higher activity than Pt/Al_2O_3 catalysts [77]; this results may be explained by the formation of surface defect on ceria after the introduction of noble metals, which promote the decomposition of the intermediates [78]. This leads to a similar reaction mechanism as for ZnO [66]. Kolb et al.[79] tested different mono and bimetallic catalysts using Pt/Rh/Pd/Ru metals on both CeO_2 and Al_2O_3 supports, with a gas composition that try to simulate the industrial conditions (46.47% H_2, 8.74% CO_2, 7.94% CO and 36.84% H_2O v/v %). The best performance was obtained with a Pt/CeO_2-Al_2O_3 catalyst. Thinon et. al. [80] performed similar tests with similar results: $Pt/CeO_2/Al_2O_3$ and Pt/TiO_2 catalysts were the most active formulations also for MTS reaction. Also Rh and Ru based catalysts are active, but produced significant amounts of methane.

Regardless the better results can be obtained with CeO_2 as support, the addition of Al_2O_3 as additive leads to more stable formulations compared to the supported catalysts. On Pt/CeO_2 catalysts, deactivation was attributed to the formation of carbon species mostly on the ceria that partial losses its re-oxidizing potential [81,82]. The carbon species formation could be reduced by alumina doping [83].

Some authors [81,82] observed an increase of the ceria crystallite size when the catalyst was exposed to reformate, which decreased the BET surface area. Others [84] attribute the deactivation of Pt/CeO_2 catalysts to the reduction of ceria by high amounts of hydrogen. This result was rejected by another work [85], because high temperature reduction in hydrogen was found to have no effect on catalyst activity, but it may be attributed to a decrease of metal dispersion, observed after exposition of the catalyst to pure CO at 400°C. Otherwise the ceria crystallite size remained constant during this treatment.

Also Zn, Cu, Fe and Co on CeO_2 and $Ni–CeO_2$ have shown an interesting activity in HTS reaction [86]. In particular, $Co–CeO_2$ showed the best catalytic performances, together with the largest deviation in the unit cell parameter of ceria that increase the oxygen vacancy and Ce^{3+} ions concentration.

Studying the effect of the support on the activity of Pt catalysts [87], supported on single (MOx) and composite (MOx/Al_2O_3, MOx/TiO_2) metal oxide carriers, where M = Ti, V, Cr,

Mn, Fe, Co, Ni, Cu, Y, Zr, La, Ce, Nd, Sm, Eu, Gd, Ho, Er, Tm, it was determined that the activity of $Pt/MO_x/Al_2O_3$ catalysts at 250 °C, depending on the nature of M in MOx.

In particular the following activity order can be described:

Ce > Co > Ti > Ho > Nd ≈ Cu > Gd ≈ La ≈ Eu ≈ Y ≈ Zr > Ni > Sm > Tm > V > Er > Fe > Cr ≈ Mn > Al_2O_3.

The rate of reaction for $Pt/CeOx/Al_2O_3$ catalyst is one order of magnitude higher compared to that for Pt/Al_2O_3. The addition of Ce increased the BET surface area and pore volume, enhancing the capability of water adsorption and splitting into O and OH species [88]. In fact a mechanism based upon redox reactions is generally considered for the WGS reaction over Pt–ceria [89,90,91,92].

Ni based bimetallic Pt catalysts were prepared by Çağlayan et al. [93], and tested in the temperature range 200–450 °C, with an inlet gas composition of 3.0% CO and 6.0%–10.0% H_2O balanced by N_2 (vol.%). They observed the higher activity and stability at lower temperatures by increasing of Ni content and H_2O/CO ratio.

Other works [94,95] report the activity of bimetallic Pt-Ni catalyst supported on CeO_2 and Al_2O_3; the CO conversion and H_2 yield can be increased by 15% and 10% compared with Pt/Al_2O_3 catalyst under the same operating conditions.

Also gold catalysts supported on CeO_2 were tested; La, Sm, Gd, Yb, and Y [96] are reported as doping elements introduced by co-precipitation and mechanochemical activation methods. The most interesting results were obtained with the catalysts doped by Yb and Sm.

Unfortunately the high cost of noble metals remain a big problem for the industrial applications [97,98].

Assuming the redox mechanism mentioned above, the noble metal particle size determines the metal–ceria interface, which is crucial for catalyst performances. At the same time it is known that non-metallic platinum species on the surface ceria are responsible for the activity, at least when nano-particles are introduced onto the catalyst carrier [99].

1.5.2 LTS catalysts

The industrial WGS process was revolutionized by the use of Cu-based catalysts because the enhancement obtained in the process allows higher CO conversions and yields in the production of H_2.

The composition of LTS catalyst need to be optimized in order to obtain active and stable catalysts in a temperature range of 180-250°C [100].

The catalysts composition is very important to provide high activity and selectivity. In fact, in LTS conditions, methanation of CO and CO_2 is thermodynamically favored. These side reactions give rise to a hydrogen consumption and an important increase of the temperature.

$CO + 3H_2 \rightarrow CH_4 + H_2O$ $\Delta H^0_{298} = -206.2$ kJ/mol

$CO_2 + 4H_2 \rightarrow CH_4 + 2H_2O$ $\Delta H^0_{298} = -165.0$ kJ/mol

Since first applications [8] Cu formulations have been employed in the LT-WGS stage. These catalysts have a good activity in LTS conditions, leading to obtain an equilibrium outlet CO lower than 0.3 % [7], and have no methanation activity.

However, the relatively low melting temperature of Cu lead to obtain systems particularly prone to sintering phenomena via surface migration, reducing the fully active catalyst life [16].

Nevertheless reaction temperatures is generally below 300 ◦C [101], in order to improve the catalyst stability, in the Cu-based systems are added components, acting as structural spacers, which decrease the aggregation of Cu crystallites during operation.

The addition of ZnO and Al_2O_3 stabilizes the copper crystallites to the sintering and minimize shrinkage [8].

Cu-based catalysts are prepared by co-precipitation in aqueous solutions of nitrates by a sodium carbonates solution at 30-60 °C and pH of 7-9. The precipitates are filtered, washed with deionized water, dried in air at 100 °C and calcined from 300 to 500 °C [102, 103].

The synthesis conditions are very important to determine the physical properties and the activity of the catalyst. Figueiredo *et al.* [104] showed that the Cu dispersion may be modulated modifying the sequence of the precursor salt precipitation. If the precursor

are precipitated together, the best results in terms of Cu dispersion and catalyst activity is obtained.

Besides their role as structural promoters, zinc and aluminum oxides also seem to act as chemical promoters. Several authors observed that Cu supported on ZnO show an enhanced activity as a result of the improved covalence between the different oxidation states of Cu in the metal lattice [105, 106]. Moving from a binary Cu/ZnO system to a $Cu/ZnO/Al_2O_3$ catalysts an improvement in the catalytic activity may be observed [107].

It is known that the WGS reaction is a structure-sensitive reaction on a Cu catalysts [108] and the stabilization of the activity is correlated to the inhibition of the sintering tendency of the Cu crystallites to form progressively larger crystallites with smaller surface area. At the same time the kind of the precursor influence the morphology and the structure of the crystalline phase [102].

The Al addition contribute to the formation of hydrotalcite phase, leading to obtain low crystalline oxides and a higher activity [107].

The correlation between activity to some catalyst characteristics, like Cu content, metal surface area and metallic Cu dispersion/dimension are very important. The activity may be correlated to the surface area of the metal. A high Cu load could give rise to an initial important activity, which rapidly decreased as a result of the metal particles sintering. A similar effect is observed increasing the calcination temperature [109].

The or turnover frequency (TOF) increases with the dispersion of metallic Cu on the catalyst surface, as a result of the structural sensitivity of the Cu-based systems [8].

Other studies report that, over a certain range of metallic Cu dispersions, CuO loading, calcination temperature and Al/Zn atomic ratio, the TOF is essentially constant and structural insensitive [107]. A similar effect can be observed in Mn-promoted Cu/Al_2O_3 [110].

Cu-based catalysts are prone to poisoning phenomena. In fact, the low temperatures favor exothermic adsorption of poisons [8].

The change of feedstock from coal to naphtha or natural gas and the improved feedstock desulfurization units opened the way to the general use of Cu-based catalysts. Cu-based catalysts may be active for 2-4 years without deactivation [8, 101] but In order to limit poisoning, a small amount of ZnO in a separate bed in the LTS converter is used [8]. Also a small bed of alkalized alumina on the top of the LTS converter may be introduced to

remove HCl before it enters the LTS catalyst [8]. To use a separate reactor containing the LTS catalyst is the best way to prevent the poison of the catalytic bed.

Cu react with sulphur, as HS, forming stable sulphides deactivating the catalyst. ZnO traps HS by the formation of zinc sulphide, more stable than copper sulphide [8]. The sulphur is preferentially adsorbed onto the small Cu crystallites (≈ 5 nm) and then transferred to ZnO, where it reacts to form the thermodynamically more stable zinc sulphide [8].

$2\ Cu + H_2S \rightleftarrows Cu_2S + H_2$ $\Delta H^0_{298} = -59.4$ kJ/mol

$ZnO + H_2S \rightleftarrows ZnS + H_2O$ $\Delta H^0_{298} = -76.6$ kJ/mol

The presence of HCl in the feed lead to the formation of cuprous chloride and Zinc chloride.

$Cu + HCl \rightleftarrows CuCl + ½\ H_2$ $\Delta H^0_{298} = -43.5$ kJ/mol

$ZnO + 2\ HCl \rightleftarrows ZnCl_2 + H_2O$ $\Delta H^0_{298} = -125.0$ kJ/mol

The low melting point of CuCl (430 °C) results in a high mobility under LTS conditions, leading to a surface-migration sintering mechanism of the Cu crystallites and an irreversible deactivation of the catalyst [8].

Zinc chloride species determines structural changes, decreasing the thermal stability [8]. These species are soluble in hot water and it is therefore important to avoid the condensation, otherwise condensate could wash chlorides further into the bed [8].

The presence of silicon may generate silica on the catalyst surface, blocking the pore and the active sites [8]. At the same time, it react with ZnO, reducing the stability of the catalyst [8].

Similar to Fe–Cr catalysts, to activate Cu-based a reduction treatment mast be performed, at temperatures between 180 and 260 °C, during the LT-WGS reactor startup [111].

The reducing reaction is highly exothermic so it is necessary to carefully control the reaction in order to limit the increase of the temperature [8]. In fact, heating above 260 °C causes the catalyst sintering and the loss of activity [8]. The reaction is carried out in situ by adding small amounts of H_2 and/or CO to an inert gas (nitrogen or natural gas) with a range temperature of 225-230°C. This temperature lead to reduce CuO keeping dispersing it into a large surface area [27].

$CuO + H_2 \rightleftarrows Cu + H_2O$ $\Delta H^0_{298} = -80.8$ kJ/mol

In the LTS reaction both Cu^+ and Cu^0 are active and the support may control the Cu^+/Cu^0 ratio, determining the activity of the catalyst[112]. It seems that ZnO acts as a reservoir for H_2 and to promotes the H_2 spill-over [113,114]. At the same time, ZnO favors the reduction of Cu-containing phases. The Cu homogeneously dispersed into the ZnO phase is more active due to the strong interaction with the oxide surface [115]. The presence of Cu dispersed in the ZnO may be verified with TPR-TPO cycles. In fact, it is possible to see a progressive increase in the Cu/ZnO ratio given by the migration of Cu to form bigger particles [116].

Dow et al. [117] have reported that the shift of the reduction temperature of CuO was related with the crystalline size of CuO; the reducibility of CuO being promoted by decreasing the crystalline size of CuO. At the same time, the reduction temperature is correlated to the interaction with Al_2O_3 phase [118]. In studies performed on CuO and ZnO supported on Al_2O_3, it is possible to see that in catalyst with higher surface (Figure 1.11 b and d) the copper oxide shows the higher reduction temperature, followed by a lower catalytic activity.

As shown in Figure 1.11, a large peak in the range 400–550 K was observed for CuO-ZnO catalysts supported on Al_2O_3, which may be attributed to the reduction of CuO species because no reduction for ZnO happens in the temperature range 373–750 K. Generally, the reduction of Cu containing species is completed below 550 K.

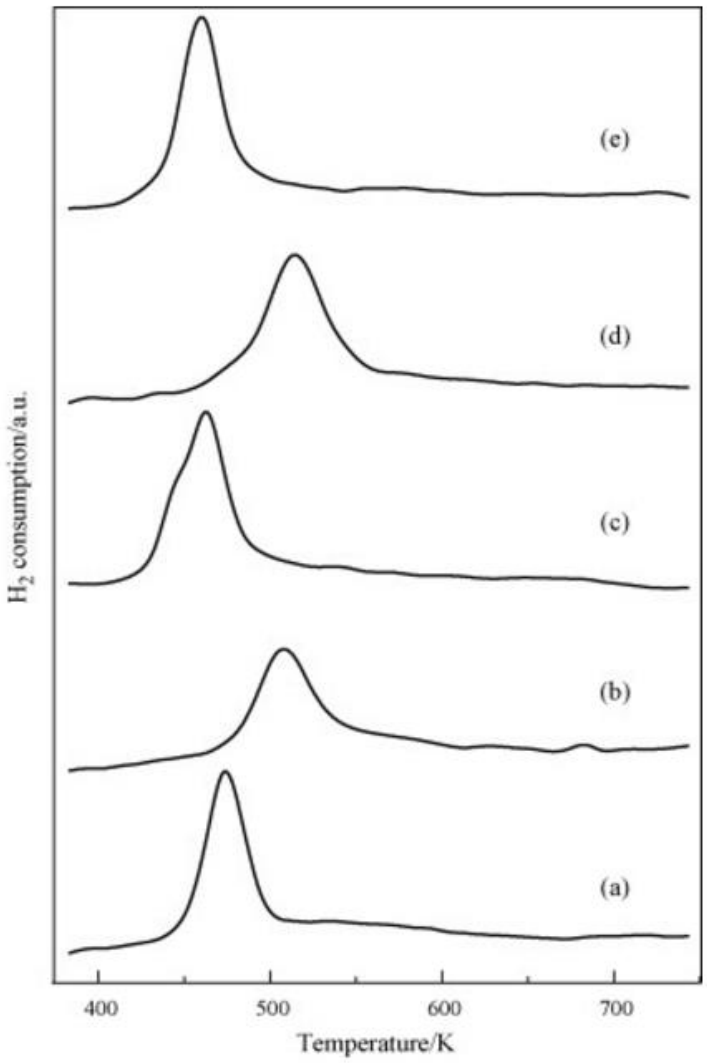

Figure 1.11 H_2-TPR profiles of CuO (5 wt.%)-ZnO(5 wt.%)/Al_2O_3 catalysts [118].

The reduction profile is strictly correlated to the preparation method [115]. In TPR profiles of the Cu/ZnO/Al_2O_3 catalyst different Cu^{2+} species may be identified [116]: copper into the ZnO lattice, amorphous and crystalline CuO and Cu^{2}+ in the Al_2O_3 phase. At 160-170 °C is reduced Cu^{2+} to Cu^{1+} and Cu^{2+} and/or Cu^{1+} to Cu^{0} species in the oxides phases, while at 210°C is reduced the copper species interacting with the Al-containing phases.
Reduced LTS catalysts are potentially pyrophoric and uncontrolled oxidation in air could result in a temperature raise between 800 and 900 °C. To avoid it, generally the reactor is discharge the catalyst under a N_2 flow [8].

$Cu + ½ O_2 \rightleftarrows CuO$ $\Delta H^0_{298} = - 157.2$ kJ/mol

To improve the catalytic activity and the stability, many studies have been performed and several elements were tested and evaluated as doping elements for LTS catalyst.

Some researchers have been focused their attention on Cu–Mn oxide catalysts, that show good activity and heat stability compared to the conventional Cu-based materials [110,119,120]. The electron-accepting potential of the catalyst and the facilitated covalency between the Cu oxidation states seems to be the reasons given for the activity enhancement.

Sekizawa *et al.* [121] tried different compositions for the commercial mixed oxides catalyst, substituting ZnO with Al, Ce, Co, Cr, Fe, Mg, Mn, Sn, Zn, and Zr showing the following sequence of the catalytic activity:

$$Zn > Al > Cr > Mn > Mg > Ce > Zr > Fe > Co$$

SiO_2 can be added to the Cu containing catalyst in order to reduce the sintering phenomena and to increase the thermal stability in reaction conditions [122].

The addition of MgO to CuO/ZnO samples has shown an increased activity attributed to the higher Cu^0 surface area followed by a BET surface area decreases [123]. The MgO addition favor the formation of Cu^+ species stabilized on the surface, also suggesting that Al_2O_3 may suppress the formation of Cu^+ species [124].

In addition, Al, Mn and Fe cupper spinels have been used in LTS reaction, prepared via co-precipitation method [119]. $CuMn_2O_4$, reduced at 250°C, shows an activity similar to the commercial catalysts in LTS conditions, but $CuFe_2O_4$ has high activity only by increasing the temperature.

The promoted Cu/Mn/B samples (where B is Al, Fe, Zr, Ce, Zn, and Cr) prepared via sol gel with the citric acid method were calcined at 900 °C in air and reduced at 250 °C [125]. The modified spinels obtained showed higher activity because of an increase in the reducibility of the cupper species.

Also ceria is an interesting support for the Cu-containing catalysts. In its studies Li showed, for Cu supported on Ce_2O_3, an activity similar to those reported for commercial systems [126].

Respect to the alumina supported systems, the ceria supported one show low surface area, but an higher Cu dispersion, leading to smaller metal particles [100]. The reducible CeO_2 support can supply active oxygen species to oxidize CO into CO_2 by temporarily reducing Ce^{4+}/Ce^{3+}, and then is oxidized again by taking oxygen from H_2O in WGS reaction.

Furthermore, ceria has a high oxygen storage capacity (OSC) and surface oxygen diffusion (280 times higher than γ-Al_2O_3 and 100 times higher than ZrO_2) [127]. Thus, this system shows higher activity respect to the alumina supported one.

A similar increased in the activity is observed by substituting Al_2O_3 with ZrO_2 and MgO.

Nobles metals supported on high surface area oxides are well known to be active in WGS reaction. The synergy of metal and oxide at the reaction interface plays an essential role in tuning both activity and selectivity [127]. For Pt/CeO_2 catalyst, there are several important characteristics to obtain good performances, like high ceria surface area, high Pt dispersion, the presence of ionic Pt rather than metallic Pt, non-stoichiometry of ceria and mesoporosity in the ceria support. It was determinate that the CO adsorption happens at Pt–ceria interface [128]. Formation of OH, surface formate, surface carbonates, CO–Ce^{4+} and CO–Ce^{3+}species were seen by in-situ DRIFTS studies, proving the mechanism involved [127].

Also gold-based catalysts are good catalysts for LTS reaction, supported on different oxides like Fe_2O_3 [129], CeO_2 [130], Al_2O_3 [131] and ZrO_2 [132]. In particular, Au/TiO2 catalysts have been used with great success since it has low cost, very good chemical stability, and is non-toxic; the catalytic activities are related also with the Au nanoparticle size distribution and the Au nanoparticles dispersion [133].

In recent years also metals supported on metal-carbides have been studied in LT-WGS reaction, and it was found that Pt/Mo_2C catalysts exhibited an activity that was 4–8 times higher than that found for a commercial Cu/ZnO/Al_2O_3 catalyst [134].

A correlation between the ability of the surfaces to partially dissociate water and their catalytic activity has been found [135].

Regardless the activity observed for the noble metal supported catalysts, the relatively high cost and limited availability of these metals may inhibit their large-scale applications. Thus, design and synthesis of more cost-effective and affordable precious metal-free catalysts are of particular interest [136].

1.5.3 MTS catalysts

Several metals, like Pt, Pd, Ru, Au, and Cu, supported on reducible nano-sized oxides (CeO_2, TiO_2 and $Ce_{(1-x)}Zr_{(x)}O_2$) have been reported active for MTS reaction, studied to achieve high activity/stability [137,138,139,140].

In particular, ceria supported systems show interesting performances in MTS reaction. The reducibility of this oxide and the high oxygen storage capacity, lead to obtain active systems in MTS temperature range.

Copper–ceria showed a good performance in low temperature WGS as well as high temperature WGS reaction, as reported in the previous sections. In 150–360 °C range Cu supported catalysts showed an activity which increases with copper loading in the range of 20–80 wt% [141].

Several studies have identified Pt/CeO_2 as a promising catalyst, showing that Ce–PtO*x* type species are active in the reaction [142] and stabilized by nano-ceria. Pt based catalysts can be preferred over other metal based catalysts because of their higher CO conversion turnover rate [143,144]. Synthetic route may be strictly correlated to the activity properties of the catalysts, in particular tuning the surface area properties [145].

Furthermore, it is also reported that nano-sized Pt particles help to stabilize CeO_2 supports against sintering or loss of surface area [142].

Si-modified Pt/CeO_2 show a higher number of oxygen defects in the support, which is associated to lower valence state cerium [146]. The Si addition gives rise to an increase in the density of hydroxyl groups on the surface of ceria, increasing the concentration of surface formate species and the activity.

Nanoparticles of gold supported on CeO_2, CeO_2-Al_2O_3, CeO_2-ZrO_2, showed interesting activity, with better results in the mixed oxides systems [147].

In case of Pt/ZrO_2 systems, it was found that zirconia polymorphism determines the catalyst activity with better performances with the monoclinic structure [148]. This behavior is due to the presence of hydroxyl surface groups, which have been claimed to be involved in the formation of important reaction intermediates. The deactivation is associated with the decrease of platinum dispersion [148].

1.5.4 Membrane reactors

In the last three decades, an important study on membrane catalysis has been carried out [149]. A Membrane Reactor (MR) is an apparatus for simultaneously carrying out the reaction and the separation in the same physical device. Therefore, the membrane not only plays the role of a separator, but also takes part in the reaction itself. A MR is an engineering apparatus that selectively removes a product from or introduces a reactant

into the reaction system, giving the possibility of better performance than a traditional reactor (TR). This improvement in performance due to the membrane effect could be achieved by shifting the equilibrium-limited reaction toward the reaction products by selectively removing a reaction product from the reaction side to the permeate side.
Some of the significant advantages of using MR's with respect to TR's can be summarized as follows:

- Conversion enhancement in equilibrium-limited reactions;
- Enhancement of the hydrogen yield and selectivity (in the field of MRs used for hydrogen production);
- Achievement of the same performance obtained in the TR at milder operating conditions or, instead, achievement of better performance at the same operating conditions;
- Reduced capital costs due to the combination of reaction and separation in only one system.

Due to the possibility to have both reaction and gas separation/purification in the same device, MR's are currently considered as good candidates for replacing TRs. MR represents an interesting possibility to reduced capital and downstream separation costs, as well as enhance yields and selectivities. In WGS reaction, it is possible to obtain higher conversion respect those obtained with TR working under the same operating conditions, or the same conversion as a TR, but working under milder operative conditions. The membrane composition may be optimized to improve the activity in WGS reaction. Many studies reported in literature are focused on hydrogen recovery from a catalytic shift MR, either using Pd-based [150,151,152,153,154] or silica membranes [155, 156].

References

1 J.R. Rostrup-Nielsen, *Catal. Rev.* **46** (2004) 247.
2 I. Dincer, C. Acar, *Int J Hydr Energy* **34** (2015) 11094.
3 I. Dincer, C. Zamfirescu, *Int J Hydr Energy* **37** (2012) 16266.
4 https://data.oecd.org/energy/primary-energy-supply.htm#indicator-chart.
5 https://www.ihs.com/products/hydrogen-chemical-economics-handbook.html.
6 https://www.iea.org/publications/freepublications/publication/KeyWorld_Statistics_2015.pdf
7 C. Rhodes, G.J. Hutchings, A.M. Ward *Catal. Today* **23** (1995) 43.
8 M.V Twigg Catalyst Handbook, 2nd ed., Wolf, London (UK), 1996.

9 S. Saeidi, F. Fazollahic, S. Najarid, D. Iranshahia, J. J. Klemeš, L. L. Baxter, *J Ind Eng Chem* (2016) 10.1016/j.jiec.2016.12.003
10 C. A. Callaghan, Chemical Engineering PhD thesis, Worcester Polytechnic Institute, 2006.
11 G.C. Chinchen, P.J. Denny, J.R. Jennings, M.S. Spencer, K.C. Waugh, *Appl. Catal.* **36** (1988) 1.
12 J.M. Moe, *Chem. Eng. Prog.* **58** (1962) 33.
13 Y. Choi, H.G. Stenger, *J Power Sources* **124** (2003) 432.
14 P. de Molliens In Technique de l'Ingénieur, Traité Génie des Procédés; Editions T.I. Vol. J 4 080, p 1.
15 C.N. Satterfield, Heterogeneous Catalysis in Industrial Practice, 2nd ed.; McGraw-Hill: New York, 1991
16 D. Mendes, A. Mendes, L. M. Madeira, A. Iulianelli, J.M. Sousa, A. Basile, *Asia-Pac. J. Chem. Eng.* **5** (2010) 111.
17 S. Ratan, C.F. Vales, *Hydr Process*, March (2002) 64.
18 J. Nakamura, J.M. Campbell, C.T. Campbell, *J. Chem. Soc. Faraday Trans.* **86** (1990) 2725.
19 C.V. Ovesen, P. Stoltze, J.K. Norskov, C.T. Campbell, *J. Catal.* **134** (1992) 445.
20 C.V. Ovesen, B.S. Clausen, B.S. Hammershoi, G. Steffensen, T. Askgaard, I. Chorkendorff, J.T. Norskov, P.B. Rasmussen, P. Stoltze, P. Taylor, *J. Catal.* **158** (1996) 170.
21 E. Tserpe, K.C. Waugh In Dynamics of Surfaces and Reaction Kinetics in Heterogeneous Catalysis, G. F. Froment, K. C. W., Ed.; Elsevier: Amsterdam, 1997; p 401.
22 K.C. Waugh, *Catal Today* **53** (1999) 161.
23 M.I. Temkin, In Advances in Catalysis; Eley, D. D., Pines, H., Weisz, P. B., Eds.; Academic Press: New York, 1979; Vol. 28; p 173.
24 C.T. Campbell, K.A. Daube, *J. Catal.* **104** (1987) 109.
25 N. Schumacher, A. Boisen, S. Dahl, A.A. Gokhale, S. Kandoi, L.C. Grabow, J.A. Dumesic, M. Mavrikakis, I. Chorkendorff, *J. Catal.* **229** (2005) 265.
26 T.S. Askgaard, J.K. Nørskov, C.V. Ovesen, P. Stoltze, *J. Catal.* **156** (1995) 229.
27 T. Shido, T. Iwasawa, *J. Catal.**140 (***1993) 575.
28 T. Van Herwijnen, W.A. De Jong, *J. Catal.***63** (1980) 83.
29 I. Fishtik, R. Datta, *Surf. Sci. **152** (*2002) 229.
30 C.A. Callaghan, I. Fishtik, R. Datta, M. Carpenter, M. Chmielewski, *Surf. Sci.* **541** (2003) 21.
31 C.R.F. Lund, M. S. Thesis, University at Buffalo, SUNY, Dept. of Chemical Engineering (2001).
32 G.J. Millar, C.H. Rochester, C. Howe, K.C. Waugh, *Mol Physics* **76** (1991) 833.
33 D. Ma, C.R.F. Lund, *Ind. Eng. Chem. Res.* **42** (2003) 711.
34 T. Van Herwijnen, W.A. De Jong, *J. Catal.***63** (1980)83.
35 J.S. Campbell, P. Craven, P.W. Young, Catalyst Handbook; Wolfe; 1970.
36 G.G. Shchibrya, N.M. Morozov, M.I. Temkin, *Kinet. Catal. USSR* **6** (1965) 1057.
37 N.V. Kul'kova, M.I. Temkin, *Zh. Fiz. Khim.* **23** (1939) 695.
38 F. Goodridge, H.A. Quazi, *Trans. Inst. Chem. Eng.* **45** (1967) T274.
39 D.C. Grenoble, M.M. Estadt, D.F. Ollis, *J. Catal.* **67** (1981) 90.
40 J. Sun, J. DesJardins, J. Buglass, K. Liu, *Int. J. Hydrogen Energy* **30** (2005) 1259.
41 R.L. Keiski, T. Salmi, P. Niemistö, J. Ainassaari, V.J. Pohjola, *Appl. Catal. **A** **137** (1996) 349.
42 G.F. Froment, K.B. Bischoff, Chemical Reactor: Analysis and Design, 2nd ed.; Wiley: New York [US].
43 J.S. Campbell, *I.E.&C. Proc. Res. Dev.* **9** (1970) 588.
44 N. Amadeo, M. Laborde, *Int. J. Hydrogen Energy* **20** (1995) 949.
45 H. Bohlbro, An investigation on the kinetics of the conversion of carbon monoxide with water vapour over iron oxide based catalysts : A contribution from The Haldor Topsøe Research Laboratory, Gjellerup, Copenhagen, 1969.
46 C. Ratnasamy, L.P. Wagner, *Catal Rev.* **51** (2009) 325.
47 H. Nishimura, T. Yatsu, T. Fujitami, T. Uchijima, J. Nakamura, *J. Mol. Catal. A* **155** (2000) 3.
48 H.S. Taylor, *J. Phys. Chem.* **30** (1926) 145.

49 R. Burch, *Phys. Chem.* **8** (2006) 5483.
50 M.A. Edwards, D.M. Whittle, C. Rhodes, A.M. Ward, D. Rohan, M.D. Shannon, G.J. Hutchings, C.J. Kiely, *Phys. Chem. Chem. Phys.* **4** (2002) 3902.
51 A. M. Ward, S. A. Axon, P. J. Murrai, WO Patent 2003,022,427 to Johnson Matthey.
52 R.J. Byron Smith, M. Loganathan, M.S. Shantha, *Int. J. Chem React. Eng.* **8** (2010) 1.
53 R. O'Brein, X.D. Hu, R. Tuell, Y. Cai, WO Patent 2005,019,099, 2005 to Sud-Chemie Inc.
54 H. Topsoe, M.J. Boudart, *J. Catal.* **31** (1973) 364.
55 M.C. Rangel, R.M. Sassaki, F. Galembeck, *Catal. Lett.* **33** (1995) 237.
56 M. Tinkle, J.A. Dumesic, *J. Catal.* **103** (1987) 65.
57 M. Robbins, K.G. Wertheim, R.C Sherwood, D.N.E. Buchanan, *J. Phys. Chem. Solids* **32** *(*1971) 717.
58 F. Domka, A. Basinska and R. Fieldcrow, *Surf. Technol.* **18** (1983) 275.
59 M.A. Edwards, D.M. Whittle, C. Rhodes, D. Rohan, M.D. Shannon, G.J. Hutchings, C. Kiely, *J. Phys. Chem. Chem. Phys.* **4** (2002) 3902.
60 M.I. Markina, G.K. Boreskov, F. P. Ivanowski, L. Yudkovskaya, *Kinet. Katal* **2** (1961) 867.
61 A. Andreev, I. Mitov, T. Tomov S. Asenov, *Proc. 10th Int. Congress. Catal*. (1992) 1523.
62 R. L. Keiski, T. Salmi *Appl. Catal.* **A 87** (1992) 61.
63 F. Meshkani, M. Rezaei, M. H. A., Shiraz *Chem. Eng. Res. Des.* **113** (2016) 9.
64 K. Wei, Q. Zheng, J. Xu, X. Ling, US Patent 6,569,804, 2003.
65 A. Andreev, V. Idakiev, D. Mihajlova, D. Shopov, *Appl. Catal.* **2** (1986) 385.
66 F. Meshkani, M. Rezaei, J. *Ind. Eng. Chem.* **20** (2014) 3297.
67 C. Rhodes, B.P. Williams, F. King, G.J. Hutchings, *Catal. Commun.* **3** (2002) 381.
68 P.S. Sidhu, R.J Gilkes, A.M. Posner, *J. Inorg. Nucl. Chem.* **40** (1978) 429.
69 V. Idakiev, A. D. Mihajlo, B. Kanev, A. Andreev, *React. Kinet. Catal. Lett.* **33** (1987) 119.
70 E.B. Quadro, M.R. Dias, A.M.M. Amorim, M.C.J. Rangel, *Braz. Chem. Soc.* **10** (1999) 51.
71 F. Meshkani, M. Rezaei, *Catal. Commun*. **58** (2015) 26.
72 P.N. Hawker, *Hydr Process.* **61** (1982) 183.
73 M.S. Batista, E.M. Assaf, J.M. Assaf, E.A. Ticianelli, *Inter. J. Hydrogen Energy* **31** (2006) 1204.
74 R.L. Keiski,T. Salmi, *Appl. Catal.* **87** (1992) 61.
75 S. Hilaire, X. Wang, T. Luo, R.J. Gorte, J. Wagner, *Appl. Catal.* **A 215** (2001) 271.
76 L. Mendelovici, M. Steinberg, *J. Catal.* **96** (1985) 285.
77 N. Koryabkina, F. Ribeiro, W. Ruettinger, Fuel cell technology: opportunities and challenges. Presented at AICHE Spring Meet. New Orleans. p 92. New York: Am. Inst. Chem. Eng.
78 T. Shido, Y. Iwasawa, *J. Catal.* **141** (1993) 71.
79 G. Kolb, H. Pennemann, R. Zapf, *Catal. Today* **110** (2005) 121.
80 O. Thinon, F. Diehl, P. Avenier, Y. Schuurman *Catal. Today* **137** (2008) 29.
81 A.F. Ghenciu, Curr. Opin., *Solid State Mater. Sci*. **6** (2002) 389.
82 A. Goguet, F. Meunier, J.P. Breen, R. Burch, M.I. Petch, A.F. Ghenciu, *J. Catal*. **226** (2004) 382.
83 R. Burch, A. Goguet, F.C. Meunier, *Appl. Catal.* **A 409–410** (2011) 3.
84 J.M. Zalc, V. Sokolovskii, D.G. Lo¨ffler, *J. Catal.* **206** (2002) 169.
85 X. Wang, R.J. Gorte, J.P. Wagner, *J. Catal.* **212** (2002) 225.
86 A. Jha, D.W. Jeong, Y.L. Lee, W.J. Jang, J.O. Shim, K.W. Jeon, C.V. Rode, H.S. Roh, *Appl. Catal.* **A 522** (2016) 21.
87 P. Panagiotopoulou, D.I. Kondarides, *Catal. Today* 127 (2007) 319.
88 J. Lilong, Y.E. Binghuo, W.E.I. Kemei, *J. Rare Earth* **26** (2008) 352.
89 S. Hilaire, X. Wang, T. Luo, R.J. Gorte, J. Wagner, *Appl. Catal. **A*** **258** (2004) 271.
90 R. Jain, R. Maric, *Appl. Catal.* **A 475** (2014) 461.
91 T. Bunluesin, R.J. Gorte, G.W. Graham, *Appl. Catal.* **B 15** (1998) 107.
92 Y. Li, Q. Fu, M. Flytzani-Stephanopoulos, *Appl. Catal.* **B 27** (2000) 179.
93 B.S. Çağlayan, A.E. Aksoylu, *Turk. J. Chem.* **33** (2009) 249.
94 R.Y. Chein, Y.H. Lin, Y.C. Chen, Y.P. Chyou, J.N. Chung, *Int. J. Hydrogen Energy* **39** (2014) 18854.

95 S. Zeng, H. Su, Y. Liu, Y. Wang, D. Wang, *J. Rare Earths* **29** (2011) 69.
96 D. Andreeva, I. Ivanov, L. Ilieva, M.V. Abrashev, R. Zanella, J.W. Sobczak, W. Lisowski, M. Kantcheva, G. Avdeev, K. Petrov, *Appl. Catal.* **A 357** (2009) 159.
97 X. Xu, Q. Fu, X. B. Chin, *J. Catal.* **36** (2015) 750.
98 S.Y. Choung, M. Ferrandon, T. Krause, *Catal. Today* **99** (2005) 257.
99 Y. Li, Q. Fu, M. Flytzani-Stephanopoulos, *Science* **301** (2003) 935.
100 D. W. Jeong, W. J. Jang, J. O. Shim, W. B. Han, H. S. Roh, U. H. Jung, W. L. Yoon, *Renew Energ* **65** (2014) 102.
101 M.V. Twigg, M.S. Spencer, *Appl. Catal.* **A 212** (2001) 161.
102 M.J.L Ginés, N. Amadeo, M. Laborde, C.R. Apesteguf*a*, *Appl. Catal.* **131** (1995) 283.
103 A.A.G. Lima, M. Nele, E.L. Moreno, H.M.C. Andrade, *Appl. Catal.* **171** (1998) 31.
104 R.T. Figueiredo, H.M.C. Andrade, J.L.G. Fierro, *Braz. J. Chem. Eng.* **15** (1998) 168.
105 T.M. Yurieva, T.P. Minyukova, *React. Kinet. Catal. Lett.*, **29** (1985) 55.
106 Y. Kanai, T. Watanabe, T. Fujitani, M. Saito, J. Nakamura, T. Uchijima, *Catal. Lett.* **27** (1994) 67.
107 C.R. Apesteguia, M.J.L. Gines, N. Amadeo, M. Laborde, *Appl. Catal.* **131** (1995) 283.
108 G.C. Chinchen, M.S. Spencer, *Catal Today* **10** (1991) 293.
109 Y. Tanaka, T. Utaka, R. Kikuchi, K. Sasaki, K. Eguchi, *Appl. Catal.* **A 238** (2003) 11.
110 D.C. Yeragi, N.C. Pradhan, A.K. Dalai, *Catal. Lett.* **112** (2006) 139.
111 W.F. Ruettinger, O. Ilinich, In Encyclopedia of Chemical Processing (Ed.: S. Lee), Taylor & Francis: 2006; p 3205.
112 J. Patt, D.J. Moon, C. Phillips, L. Thompson, *Catal. Lett.* **65** (2000) 193.
113 R. Burch, S.E. Golunski, M.S. Spencer, *Catal. Lett.* **5** (1990) 55.
114 R. Burch, S.E. Golunski, M.S. Spencer, *J. Chem. Soc. Faraday Trans.* **86** (1990) 2683.
115 G. Fierro, M.L. Jacono, M. Invers, P. Porta, F. Cioci, R. Lavecchia, *Appl. Catal.***137** (1996) 327.
116 R.T. Figueiredo, A.L.D. Ramos, H.M.C. Andrade, J.L.G. Fierro, *Catal. Today* **671** (2005) 107.
117 W.P. Dow, Y.P. Wang, T.J. Huang, *J. Catal.* **160** (1996) 155.
118 H. Yahiro, K. Murawaki, K. Saiki, T. Yamamoto, H. Yamaura, *Catal. Today* **126** (2007) 436.
119 Y. Tanaka, T. Utaka, R. Kikuchi, K. Sasaki, K. Eguchi, *Appl. Catal.*, **242** (2003) 287.
120 F.M. Gottschalk, G.J. Hutchings, *Appl. Catal*. **51** (1989) 127.
121 K. Sekizawa, S. Yano, K. Eguchi, H. Arai, *Appl. Catal.* **169** (1998) 291.
122 M.J.L. Ginés, N. Amadeo, M. Laborde, C.R. Apesteguia, *Appl. Catal.* **131** (1995) 283.
123 T. Shishido, M. Yamamoto, I. Atake, D. Li, Y. Tian, H. Morioka, M. Honda, T. Sano, K. Takehira, *J. Mol. Catal.* **A 253** (2006) 270.
124 T. Shishido, M. Yamamoto, D. Li, Y. Tian, H. Morioka, M. Honda, T. Sano, K. Takehira, *Appl. Chem.* **A 303** (2006) 62.
125 Y. Tanaka, T. Takeguchi, R. Kikuchi, K. Eguchi, *Appl. Catal.* **A 279** (2005) 59.
126 Y. Li, Q. Fu, M. Flytzani- Stephanopoulos, *Appl. Catal.* **27** (2000) 179.
127 R. Jaina, A. S. Poyraz, D. P. Gamliel, J. Vallac, S. L. Suibb, R. Maric, *Appl. Catal.* **A 507** (2015) 1.
128 S. Aranifard, S.C. Ammal, A. Heyden, *J. Catal*. **309** (2014) 314.
129 M.A. Soria, P. Pérez, S.A.C. Carabineiro, F.J. Maldonado-Hódar, A. Mendes, L.M. Madeira, *Appl Catal* **A 470** (2014) 45.
130 W. Deng, A.I. Frenkel, R. Si, M. Flytzani-Stephanopoulos, *J Phys Chem C* **112** (2008) 12834.
131 M. Shekhar, J. Wang, W.-S. Lee, W.D. Williams, S.M. Kim, E.A. Stach, *J Am Chem Soc*. **134** (2012) 4700.
132 Y.J. Zhang, Y.Y. Zhan, C.Q. Chen, Y.N. Cao, X.Y. Lin, Q. Zheng, *Int J Hydr Energy* **37** (2012) 12292.
133 P. Perez, M. A. Soria, S.A.C. Carabineiro, F. J. Maldonado-Hodar, A. Mendes, L. M. Madeira, *Int J Hydrogen Energy* **41** (2016) 4670.
134 K. D. Sabnis, Y. Cui, M. C. Akatay, M. Shekhar, W.S. Lee, J. T. Miller, W. N. Delgass, F.H. Ribeiro, J. Catal. **331** (2015) 162.
135 A. Rodriguez, P.J. Ramírez, R.A. Gutierrez, *Catal. Today* (2016) http://dx.doi.org/10.1016/j.cattod.2016.09.020.

136 F. Marino, C. Descorme, D. Duprez, *Appl Catal* **B 58** (2005) 175.
137 Y. Bi, H. Xu, W. Li, A. Goldbach, Int. J. Hydr Energy **34** (2009) 2965.
138 P. Panagitopoulou, D.I. Kondarides, *J. Catal.* **225** (2004) 327.
139 G. Jacobs, L. Williams, U. Graham, G.A. Thomas, D.E. Sparks, B.H. Davis, *Appl. Catal.* **A 252** (2003) 107.
140 F. Meunier, A. Goguet, C. Hardacre, R. Burch, D. Thompsett, *J. Catal*. **252** (2007) 18.
141 P.V.D.S. Gunawardana, H.C. Lee, D.H. Kim, *Int J Hydr Energy* **34** (2009) 1336.
142 X. Wang, R.J. Gorte, *Appl. Catal.* **A 247** (2003) 157.
143 P. Panagiotopoulou, D.I. Kondarides, *Catal. Today* **112** (2006) 49.
144 G.G. Olympiou, C.M. Kalamaras, C.D. Zeinalipour-Yazdi, A.M. Efstathiou, *Catal. Today* **127** (2007) 304.
145 H.S. Roh, H.S. Potdar, D.W. Jeong, K.S. Kim, J.O. Shim, W.J. Jang, K.Y. Koo, W.L. Yoon, *Catal, Today* **185** (2012) 113.
146 K.R. Hwang, J.S. Park, S.K. Ihm, *Int J Hydr Energy* **36** (2011) 9685.
147 C. Galletti. S. Specchia, G. Saracco, V. Specchia, *Top Catal* **52** (2009) 688.
148 C.A. Franchini, A.M. Duarte de Farias, E.M. Albuquerque, R. dos Santos, M.A. Fraga, *Appl. Catal.* **A 117–118** (2012) 302.
149 D. Mendes, A. Mendes, L. M. Madeira, A. Iulianelli, J. M. Sousa, A. Basile, *Asia-Pac. J. Chem. Eng.* **5** (2010) 111.
150 S. Uemiya, N. Sato, H. Ando, E. Kikuchi, *Ind. Eng. Chem. Res*. **30** (1991) 585.
151 A. Basile, G. Chiappetta, S. Tosti, V. Violante, *Sep. Purif. Technol.* **25** (2001) 549.
152 S. Tosti, V. Violante, A. Basile, G. Chiappetta, S. Castelli, M. De Francesco, S. Scaglione, F. Sarto, *Fusion Eng. Des.*, **49** (2000) 953.
153 A. Brunetti, G. Barbieri, E. Drioli, K.H. Lee, B. Sea, D.W. Lee, *Chem. Eng. Prog.* **46** (2007) 119.
154 O. Iyoha, R. Enick, R. Killmeyer, B. Howard, B. Morreale, M. Ciocco, *J. Memb. Sci.* **298** (2007) 14.
155 S. Giessler, L. Jordan, J.C. Diniz da Costa, G.Q. Lu, *Sep. Purif. Technol.* **32** (2003) 255.
156 S. Battersby, M.C. Duke, S. Liu, V. Rudolph, J.C. Diniz da Costa, *J. Memb. Sci.* **316** (2008) 46.

2 Experimental session

2.1 Catalysts preparation

The catalysts used during this research work can be divided in two different classes.

The first one consists of mixed oxides prepared by co-precipitation technique, starting from hydrotalcite phase as precursor.

The second one consists of pure spinels materials; this class of catalyst was prepared via sol-gel technique.

2.1.1 Synthesis by co-precipitation: hydrotalcite-type structures.

Hydrotalcite (Ht) is an anionic structure, also called Layered Double Hydroxide (LDH). The morphology of the material derives from the brucite $Mg(OH)_2$, in which Mg^{2+} cations are octahedrally coordinated by hydroxyl ions, sharing the edges and forming layers of octahedral. The partial substitution of M^{2+} with M^{3+} with similar radius (like Al^{3+} for Mg^{2+}) produces a positive charge in the hydroxyl layer. This net positive charge is compensated by anions (for example, CO_3^{2-}), which are located between two brucite-type sheets (Figure 2.1).

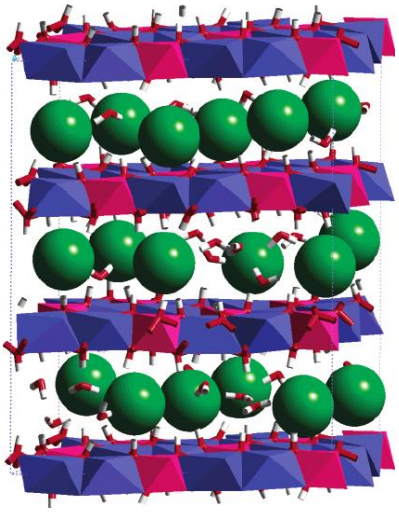

Figure 2.1 Crystal structure of hydrotalcite type precursor.

HT-type compounds have the general formula:

$$[M^{2+}_{1-x}\, M^{3+}_{x}(OH)_2]^{x+}A^{n-}_{x/n}\cdot mH_2O$$

where M^{2+} is a divalent cation (Mg^{2+}, Ni^{2+}, Zn^{2+}, Cu^{2+}, etc.), while M^{3+} is a trivalent cation (Al^{3+}, Cr^{3+}, Fe^{3+}, etc.), and $A^{n-}_{b/n}$ is an anion (CO_3^{2-}, SiO_4^{4-}, NO_3^{-}, Cl^{-}, SO_4^{2-}, etc.).

Hydrotalcite-type compounds are formed with x value in the range of 0.1-0.5, while pure hydrotalcite type compounds may be obtained only for $0.20 \leq x \leq 0.33$. X values outside this range lead to a too high density of neighboring M^{3+} in the brucite-type layer sheet, forming metal hydroxides side phases [1].

Cations having ionic radii similar to Mg^{2+} may form HT-type compounds. In case of Cu^{2+} ions, hydrotalcite type compounds may be formed only with another bivalent cation (Table 2.1).

M^{2+}	Mg^{2+}	Cu^{2+}	Ni^{2+}	Co^{2+}	Zn^{2+}	Fe^{2+}	Mn^{2+}	Cd^{2+}
Ionic radius (Å)	0.65	0.69	0.72	0.74	0.74	0.76	0.80	0.97
M^{3+}	Al^{3+}	Ga^{3+}	Ni^{3+}	Co^{3+}	Fe^{3+}	Mn^{3+}	Cr^{3+}	In^{3+}
Ionic radius (Å)	0.50	0.62	0.62	0.63	0.64	0.66	0.69	0.81

Table 2.1 Ionic radius of some cations [1].

Hydrotalcite phases are used as catalysts precursors because, after calcination, mixed oxides obtained have several advantages:

1) High surface area;
2) Chemical homogeneity and strong Lewis basic sites;
3) Very small crystal size, stable to thermal treatments, which may form thermally stable metal crystallites by reduction;
4) ‘‘Memory effect’’, which allows the reconstruction, under mild conditions, of the original HT-type structure when the product of the thermal treatment is put in contact with water solutions containing various anions.

The catalysts Ht-type precursors, reported, in were prepared following the procedure reported below.

1) Preparation of 2M nitrate solution of M^{2+} and M^{3+} ions and 1M solution of sodium hydrocarbonate as precipitant.
2) Co-precipitation by drop wise addition of the metal nitrate solution into sodium hydrocarbonate solution, stirred at 60 °C. The pH was carefully kept at 9.0 with 3M NaOH solution.
3) The precipitate was then aged at 60 °C for 45 min.

4) The obtained precipitate was filtered, washed carefully by a large amount of distilled water (500 mL/g Ht) at 70 °C, and dried for 12 h at 70 °C.
5) The Ht type precipitate was then ground into powder and calcined at 550 °C for 6h.

The formulations of the catalysts tested in medium (MTS) and high temperature shift (HTS) reaction are reported in Table 2.2 and Table 2.3.

The name of the catalyst is derived from the following equation, which lead to directly get the catalyst composition; ZnAlCuXYcR

X = Cu wt%; Y = M^{2+}/M^{3+} mol/mol; c = precipitated by carbonates;

R = doping element

If R is M^{2+} n= Zn/R mol/mol; if R is M^{3+} n= Al/R mol/mol

Catalyst	Cu (wt %)	Zn (wt %)	Mg-Ba (wt%)	Al (wt%)	La-Zr-Ce (wt%)
ZAC22c	20.0	41.0	/	13.0	/
ZAC23c	20.0	46.3	/	9.2	/
ZAC23cLa50	20.0	45.8	/	8.9	0.9
ZAC23cZr50	20.0	46.0	/	9.0	0.6
ZAC23cCe50	20.0	45.8	/	8.9	0.9
ZAC23cM4	20.0	40.4	3.75	9.2	/
ZAC23cM1	20.0	29.3	10.87	9.8	/
ZAC23cM0.65	20.0	24.4	13.96	10.9	/
ZAC23cM0.5	20.0	21.4	15.89	11.3	/
ZAC23cB4	20.0	32,29	16,96	8,38	/

Table 2.2 Weigh percentage composition of the medium temperature shift calcined catalysts.

Catalyst	Cu (wt%)	Zn (wt%)	Al (wt%)	In-La-Ga (wt%)
ZAC041c	4.0	45.3	20.4	0
ZAC041cIn50	4.0	42.7	17.7	6.9
ZAC041cLa50	4.0	42.1	17.5	8.2
ZAC041cGa200	4.0	45.2	20.3	0.3
ZAC041cGa50	4.0	45.0	19.9	1.0
ZAC041cGa28	4.0	44.8	19.5	1.8
ZAC041cGa20	4.0	44.6	19.1	2.4
ZAC041cGa14	4.0	44.3	18.6	3.4
ZAC041cGa11	4.0	44.1	18.2	4.25

Table 2.3 Weigh percentage composition of the high temperature shift reaction calcined catalysts.

2.2 Synthesis via sol-gel: spinel structures

The sol-gel technique is a very versatile methodology, which lead to obtain highly pure materials.

The process consists of three main steps.

1) Preparation of precursores solution
2) Gelification of the solution
3) Thermal treatment of the obtained gel

Different procedures can be distinguished by the gelling agent. In the method used citric acid was used [2]. The synthesis procedure is:

1) Dissolution of metal nitrates into de-ionized water
2) Addition of citric acid (Ac/Me= 3)
3) Aging at 70°C for 30 min
4) PH adjust at 3
5) Aging at 100°C for 12 h
6) Calcination of the obtained gel

2.3 Industrial catalysts

To compare performances of synthesized catalysts with commercial systems, two commercial catalysts were tested under MTS conditions.

Compositions are reported in Table 2.4.

Catalyst	Element	Weight content (%wt/wt)
CAT1	Cu	26
	Zn	31
	Al	19
CAT2	Cu	16
	Zn	26
	Cr	32

Table 2.4 Weigh content of CAT1 and CAT2 catalysts.

2.4 Characterization methods

2.4.1 X-Ray Diffraction Analysis

The XRD powder analysis was carried out using a Philips PW1050/81 diffractometer equipped with a graphite monochromator in the diffracted beam and controlled by a PW1710 unit (Cu K_α, λ = 0.15418 nm). A 2θ range from 5° to 80° was investigated, using a step size of 0.1° and a time per step of 2 sec.

2.4.2 Temperature programmed analysis (TPR)

The reduction profiles have been measured using a Micromeritics AutoChem II Chemisorption Analyzer, equipped by a Thermal Conductivity Detector (TCD). The analysis was carried out loading 0.08 g of sample and using two different procedures for fresh and spent catalyst.

On fresh catalysts:

1) Pre-treatment: the sample was pre-treated under He (20 mL/min) from room temperature to 150 °C (20 °C/min) and hold for 30 min at 150 °C.
2) Reduction: after cooling until 60 °C, the reduction analysis was performed using a 5%v/v H_2/Ar gas mixture (20 mL/min) up to 750 °C (10 °C/min) and hold for 60 min at this temperature.

3) Oxidation: after cooling until 60 °C, the oxidation analysis was performed using a 5 % v/v O_2/Ar gas mixture (20 mL/min) up to 750 °C (10 °C/min) and hold for 60 min at this temperature.
4) Reduction: after cooling until 60 °C, the reduction analysis was performed using a 5 % v/v H_2/Ar gas mixture (20 mL/min) up to 750 °C (10 °C/min) and hold for 60 min at this temperature.

On spent catalysts:

5) Pre-treatment: the sample was pre-treated under N_2 (20 mL/min) from room temperature to 150 °C (20 °C/min) and hold for 30 min at 150 °C.
6) Reduction: after cooling until 60 °C, the reduction analysis was performed using a 5 % v/v H_2/Ar gas mixture (20 mL/min) up to 550 °C (10 °C/min) and hold for 60 min at this temperature.

2.4.3 Surface area analysis

The surface area values of the catalysts were determined by N_2-physisorption at – 196 °C by the Brunauer-Emmet-Teller (BET) method using a Carlo Erba Sopty instrument. The sample (0.5 g) was pre-treated at 150 °C under vacuum to eliminate impurities and water superficial adsorbed; subsequently, it was analyzed in a liquid N_2 bath.

2.4.4 Determination of the specific Cu surface area

The specific Cu surface area was measured using N_2O-chemisorption on the Cu metal surface [3,4,5,6,7]. The amounts of un-reacted N_2O and formed N_2 were determined by a Pulse Chromatography (PC) [5,6].

The analysis was carried out on 0,10g of sample loaded into a micro-reactor in an Agilent Technologies 7890B GC System, equipped with a GS-CARBONPLOT (Carrier gas= He, 30mm x 0,53mm x 3 μm) column for N_2/N_2O separation and a TCD detector.

The analysis procedure consists of:

1) Reduction step with a H_2/N_2 = 5:95 v/v stream. Temperature ramp consists of 10°C/min from 40 to 350 °C for HTS catalyst formulations and from 40 to 220 °C for MTS catalysts, followed by 1 h of isotherm.

2) H_2 desorption, with He stream for 20 min at the final temperature and cooling until 60°C (10 °C/min).
3) The analysis was carried out by introducing successive pulses of 1.0 mL of N_2O until the N_2O area was constant (10 pulses ca.).

2.4.5 FT-IR analysis

For FT-IR a Bruker FTIR Equinox 55 was used, equipped with a MCT detector working with a 2 cm^{-1} resolution. The catalyst powder was pressed and loaded on an Au sample holder. The sample holder was positioned inside a cell equipped with KBR windows.
The sample was firstly degassed at 150°C under vacuum (residual pressure < 10^{-1} Pa). Then the sample was heated under H_2 pressure (2.66 x 10^4 Pa) until 300°C and maintained at final temperature for 1h. Analyses were performed with CO as probe molecules at -196°C, using liquid N_2. FTIR spectra were acquired increasing the P_{CO} (from $6 \cdot 10^1$ to $4 \cdot 10^3$ Pa).

2.5 NH_3 leaching

Catalysts prepared via sol-gel technique were treated with NH_3 30% v/v to remove Cu by formation of cupro-ammonia complex. The complete metal leaching was verified by UV-Vis analysis performed on the used ammonia solution.

2.6 Catalyst shape

The catalysts obtained by calcination of the dried Ht type precursors and the spinels were pressed at 10 tons for 15 min to obtain a tablet, crashed and pelletized to 30-40 mesh to optimize the radial temperature gradient, reducing the diffusion effect ($d_{reactor}/d_{catalyst} \geq 5$).

2.7 Reduction step

Before the catalytic test, catalysts were activated by reduction.
The activation procedure is different for MTS and HTS .
For MTS catalysts it was performed feeding a mixture of H_2/N_2 at 10 bars and a Gas Hourly Space Velocity (GHSV) between 300 and 400 h^{-1}. The reduction is described by the following procedure:

1) O_2 present in the reactor was removed completely using flow of N_2 and heating up to 175 °C (1 °C/min) in 90 min.
2) At 175 °C, the reduction started using a flow of 1.2 % v/v H_2/N_2 and hold for 2 h at this temperature.
3) The temperature was then increased to 220 °C (1 °C/min) without changing the composition of the flow gas.
4) At 220 °C, H_2 was added up to 4 % v/v H_2/N_2 and hold for 20 h.

For HTS catalysts the reduction was performed feeding the reaction mixture (CO 16,8 %v/v, CH_4 4.1 %v/v, CO_2 4,1 % and H_2 75 %v/v) and steam (S/DG= 0.55) at 10 bar and a GHSV of 1200 h^{-1}.

1) O_2 present in the reactor was removed completely using flow of N_2 and heating up to 275 °C (10 °C/min).
2) At 275 °C the reduction started using the reaction mixture.
3) The reactor is heated until 350 °C (0.5°C/min).

2.8 Lab-scale Pilot Plant

The catalytic tests were carried out in a laboratory pilot plant, reported in Figure 2.2.
The feed section consisted of three gas lines [N_2, H_2 and Dry Gas (CO, CH_4 and CO_2)] and one line to feed H_2O. Gas flow rates were controlled by thermal mass flow controllers, while distilled H_2O was fed by a HPLC pump.
Before being mixed with the gas flow, H_2O is vaporized at 215 °C.
The reaction section is composed by a fixed bed tubular reactor (INCOLOY 800HT: 19-23% Cr/30-35% Ni/39.5% Fe/0.06-0.1% C) with an internal diameter of 10 mm, vertically placed into an electric oven.
The temperature profile of catalyst is measured with a cromel/alumel thermocouple (d = 0.8 mm) inserted inside the reactor. The catalyst was loaded in the isothermal zone, between two layers of inert material (corundum 20 mesh).
The unreacted water is completely separated from the outlet stream by a cooled gas-liquid separator maintained at 0 °C.
The pressure was controlled by a pressure controller placed after the condenser.

The outlet gas stream is measured by a drum-type gas meter, followed by a water trap system filled with drierite.

Finally, the outlet stream was analyzed by a Agilent Technology 7890 GC equipped with GS CARBON PLOT (Carrier gas= H_2, 30m, 530um, 3um) and a CP-Volamine 5A (Carrier gas= N_2, 50m, 25m, 530 um) and two TCD detectors.

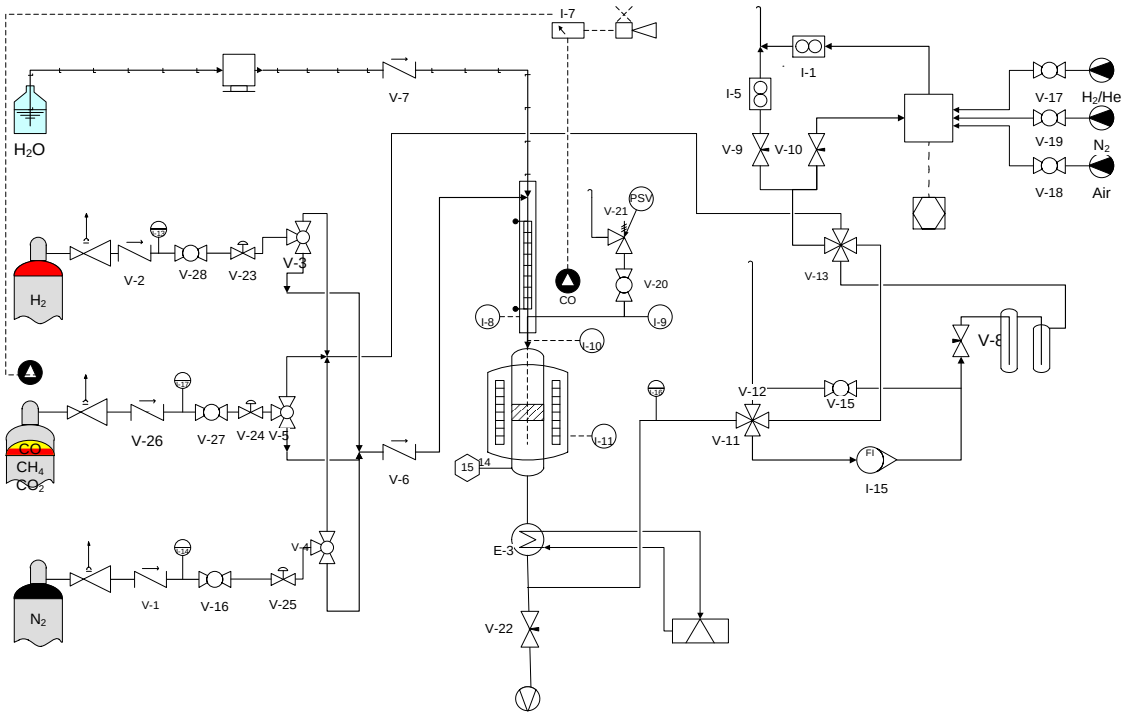

Figure 2.2 Process flow diagram of the lab-scale pilot plant.

2.9 Activity Tests

The activity tests simulated the industrial conditions, studying the effect of different parameters on the catalytic activity. The study was also focused to optimize the reaction conditions with low S/DG ratio and contact time values, thus ensuring a lower overhead of the plant. Activity test conditions used are different for MTS (Table 2.5) and HTS catalysts (Table 2.6).

Test	T (°C)	P (°C)	S/DG (v/v)	τ (s)
1	250	15	0,55	0,50
2	250	15	0,55	1,00
3	250	15	0,25	1,00
4	300	15	0,55	0,50

5	300	15	0,55	1,00
6	300	15	0,25	1,00
7	300	15	0,55	0,50
8	350	15	0,55	1,00
9	350	15	0,25	1,00

Table 2.5 List of the tests carried out for the MT-WGS reaction.

Test	T (°C)	P (bar)	S/DG (v/v)	τ (s)
Screening conditions	430	20	0,55	3
1	350	15	0,55	0,25
2	350	15	0,55	0,50
3	350	15	0,55	1,00
4	400	15	0,55	0,50
7	400	15	0,55	1,00
6	450	15	0,55	0,50
7	450	15	0,55	1,00
8	350	15	0,65	0,50
9	350	15	0,65	1,00
10	400	15	0,65	0,50
11	400	15	0,65	1,00
12	450	15	0,65	0,50
13	450	15	0,65	1,00

Table 2.6 List of the tests carried out for the HT-WGS reaction.

2.10 Data elaboration

The data obtained from the GC analysis showing the DG composition after reaction, together with the total amount of condensed water, allow to calculate the conversion (χ), selectivity (S), yield (ϒ) and mass balance ($C_{OUT/IN}$) values, by using the following formulas:

CO conversion

$$\chi_{CO} = \frac{[CO]^{IN} - [CO]^{OUT}}{[CO]^{IN}} 100 = 1 - \frac{[CO]^{OUT}}{[CO]^{IN}} 100 = \left(1 - \frac{\%CO^{OUT} F_{DG}^{OUT}}{\%CO^{IN} F_{DG}^{IN}}\right) 100$$

H_2O conversion

$$\chi_{H2O} = \frac{[H2O]^{IN} - [H2O]^{OUT}}{[H2O]^{IN}} 100 = 1 - \frac{[H2O]^{OUT}}{[H2O]^{IN}} 100$$

$$= \left(1 - \frac{V_{H2O}^{OUT}\ 1{,}006}{F_{H2O}^{IN} t_{STREAM}}\right) 100$$

Selectivity

$$S_j = \frac{[j]}{[CO]^{IN} - [CO]^{OUT}} 100 = \frac{[j]^{OUT} - [j]^{IN}}{[CO]^{IN} - [CO]^{OUT}} 100$$

$$= \left(\frac{\%j^{OUT} F_{DG}^{OUT} - \%j^{IN} F_{DG}^{IN}}{\%CO^{IN} F_{DG}^{IN} - \%CO^{OUT} F_{DG}^{OUT}}\right) 100$$

where j = CO_2,CH_4,H_2

H_2 yield

$$\gamma_{H2} = \frac{[H2]}{[CO]^{IN}} 100 = \frac{[H2]^{OUT} - [H2]^{IN}}{[CO]^{IN}} 100$$

$$= \left(\frac{\%H2^{OUT} F_{DG}^{OUT} - \%H2^{IN} F_{DG}^{IN}}{\%CO^{IN} F_{DG}^{IN}}\right) 100$$

$$\gamma_{H2} = \frac{[H2]}{[CO]^{IN}} 100 = \frac{[H2]}{[CO]^{IN} - [CO]^{OUT}} \frac{[CO]^{IN} - [CO]^{OUT}}{[CO]^{IN}} 100 = \frac{\chi_{CO} S_{H2}}{100}$$

C balance

$$\%C_{OUT/IN} = \frac{[CO]^{OUT} + [CH4]^{OUT} + [CO2]^{OUT}}{[CO]^{IN} + [CH4]^{IN} + [CO2]^{IN}} 100$$

$$= \left(\frac{\%CO^{OUT} + \%CH4^{OUT} + \%CO2^{OUT}}{\%CO^{IN} + \%CH4^{IN} + \%CO2^{IN}} \frac{F_{DG}^{OUT}}{F_{DG}^{IN}}\right) 100$$

Nomenclature

$\%CO^{IN}$ = Inlet percentage of CO

$\%CO^{OUT}$ = Outlet percentage of CO

$\%CH_4^{IN}$ = Inlet percentage of CH_4

$\%CH_4^{OUT}$ = Outlet percentage of CH_4

$\%CO_2^{IN}$ = Inlet percentage of CO_2

$\%CO_2^{OUT}$ = Outlet percentage of CO_2

$\%H_2^{IN}$ = Inlet percentage of H_2

$\%H_2^{OUT}$ = Outlet percentage of H_2

F_{DG}^{IN} = Inlet flow of Dry Gas

F_{DG}^{OUT} = Outlet flow of Dry Gas

F_{H2O}^{IN} = Inlet flow of H_2O

V_{H2O}^{OUT} = Outlet volume of H_2O

t_{STREAM} = time of stream

2.11 Determination of by-products concentration in collected water

The by-products obtained during the reaction were collected with the unreacted in the cooled gas-liquid separator. To determinate the concentrations, the aqueous solutions were analyzed by a Agilent Technology 7890A GC equipped with a CP-Volamine 5A (Carrier gas= H_2, 50m, 25m, 530 um) and a FID detector. Samples were stocked at 3°C to avoid solute loss. Lower detection limits are reported in Table 2.7.

Reaction by-products	Lower Detection Limit [ppm]
Methanol	10
Ethanol	10
Mono methyl amine	1500
Di methyl amine	300
Tri Methyl amine	150

Table 2.7 Lower detection limits determinate for the reaction by-products.

References

1 F. Cavani, F. Trifirò, A. Vaccari, *Catal. Today* **11** (1991) 173.
2 B.K. Kwak, D.S. Park, Y.S. Yun, J. Yi, *Catal. Comm.* **24** (2012) 90.
[3]3 T.J. Osinga, B.G. Linsen, W.P. van Beek, *J. Catal.* **7** (1967) 277.
4 B. Dvořák, J. Pašek, *J. Catal.* **18** (1970) 108.
5 J.J.F. Scholten, J.A. Konvalinka, *Trans. Farad. Soc.* **65** (1969) 2465.
6 J.W. Evans, N.W. Cant, D.L. Trimm, M.S. Wainwright*, App.l Catal.* **6** (1983) 355.
7 Narita, N. Takezawa, H. Kobayashi, I. Toyoshima, *React. Kinet. Catal. Lett.* **19** (1982) 91.

3 Result and discussion

3.1 Medium Temperature Shift: improve of the performances

An interesting alternative to the two steps WGS reaction, is a single step operating at Medium Temperature (MTS).

Starting from the work carried out in the last years [1], the study was developed to optimize and improve the performances of the catalyst for the industrial applications.

For this purpose, different doping elements were added to a Cu/Zn/Al catalyst.

At the same time, it was carried out a specific study to point out the key parameters who have to be controlled to improve the whole process efficiencies.

3.1.1 Effect of La, Zr and Ce addition on Cu-based catalysts

During the last years, an active catalyst in MTS reaction conditions was developed and patented by our research group [2]. The catalyst formulation is reported in Table 3.1 and is characterized by a Me^{3+}/Me^{2+} ratio of 3 and synthesized by co-precipitation method.

The name of the catalyst is derived from the following equation, which leads to directly get the catalyst composition;

ZnAlCuXYc, X = Cu wt%; Y = M^{2+}/M^{3+}; mol/mol; c = precipitated by carbonates

ZAC23c	Zn	Al	Cu
wt %	46,27	9,19	20,00

Table 3.1 ZAC23c composition.

The XRD pattern (Figure 3.1) of the catalyst precursor evidences only the peaks related to the hydrotalcite-type phase (Ht). After calcination, it is possible to observe the formation of ZnO, Zn or Cu aluminates and CuO.

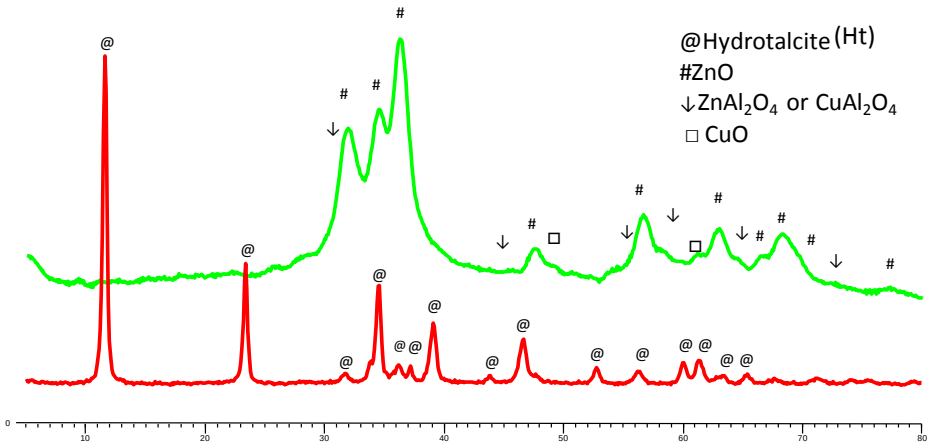

Figure 3.1 XRD pattern of the precursor and calcined ZAC23c catalyst.

Calcined sample was tested as WGS catalyst using the following reaction conditions: temperature range (250-300-350°C); contact time (0,5 and 1s) and steam to dry gas (0,25 and 0,5 v/v). In Figure 3.2 are reported the CO conversion obtained in each test, compared with the equilibrium value.

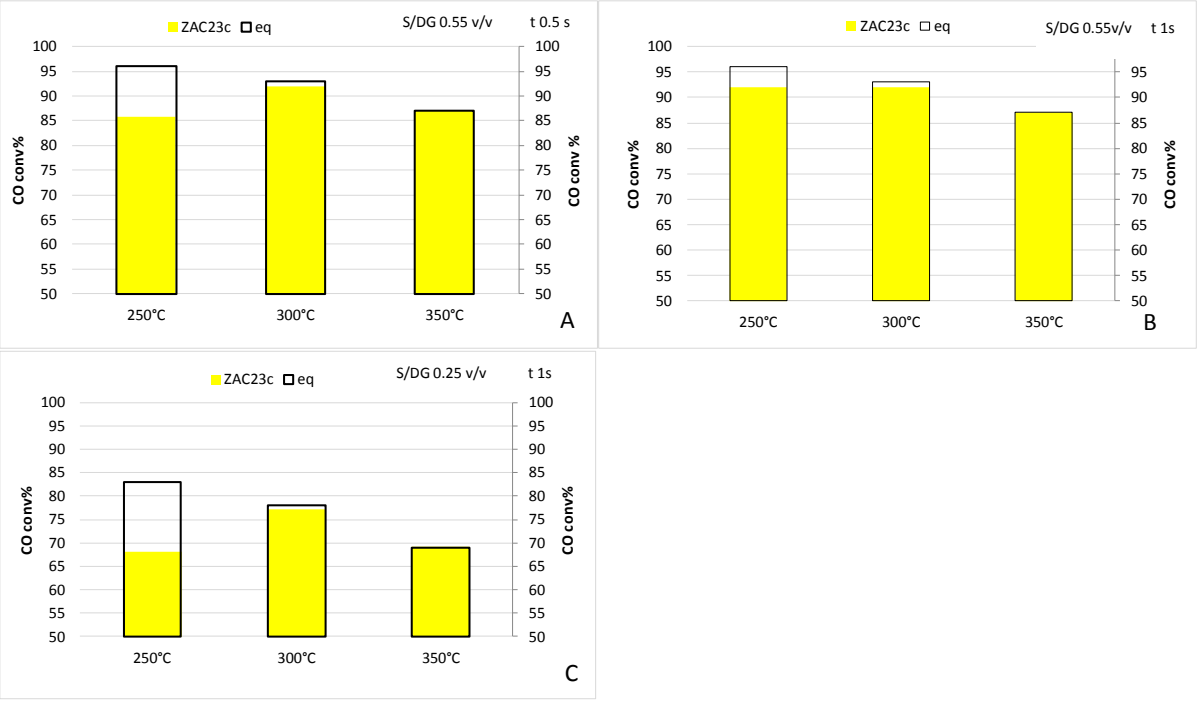

Figure 3.2 Activity obtained in the tests on ZAC23c; effect of temperature at different reaction conditions.

Figure A; S/DG= 0.55v/v, t= 0.5s

Figure B; S/DG = 0.55v/v, t= 1s

Figure C; S/DG = 0.25v/v, t= 1s

In figure 3.2 A are reported the results of the catalytic tests in reference conditions, pointing out the effect of temperature in the tests performed with S/DG of 0.55v/v and contact time of 0.5s.

Comparing Figure 3.2 A and B it is possible to observe the effect of contact time on the CO conversion Finally, in Figure 3.2 C are reported the results obtained in the most stressing conditions; in fact, in these tests the vapor content is decreased, with a S/DG value of 0.25v/v. At 300°C equilibrium values are reached for all reaction conditions (Figure 3.2); while at 250°C the CO conversion do not reach equilibrium values, rising by increasing the contact time and vapor content.

At the end of the whole reactivity cycle, the initial test was repeated and a decrease of 5% in the CO conversion was observed.

To improve the activity already at lower temperature and to increase the stability of the ZAC23c catalyst, it was doped by La, Zr and Ce, respectively.

It is reported in literature that La and Zr improve the physical properties, but without any evidence to increase the catalytic performances [3]. Furthermore, CeO_2 is an oxide already studied in LTS reaction [4].

The doped catalysts were synthesized using an Al/Me ratio of 50 (composition reported in Table 3.2).

All the precursors were characterized by XRD, showing the presence of a hydrotalcite-type (Ht) phase (Figure 3.3). In the doped catalysts, also the presence of aurichalcite phase may be observed.

Catalyst	Cu(wt%)	Zn(wt%)	Al(wt%)	R(wt%)
ZAC23c	20.00	46.27	9.19	/
ZAC23cLa50	20.00	45.78	8.95	0.92
ZAC23cZr50	20.00	45.99	8.98	0.61
ZAC23cCe50	20.00	45.77	8.95	0.93

Table 3.2 Metal content in the ZAC catalysts.

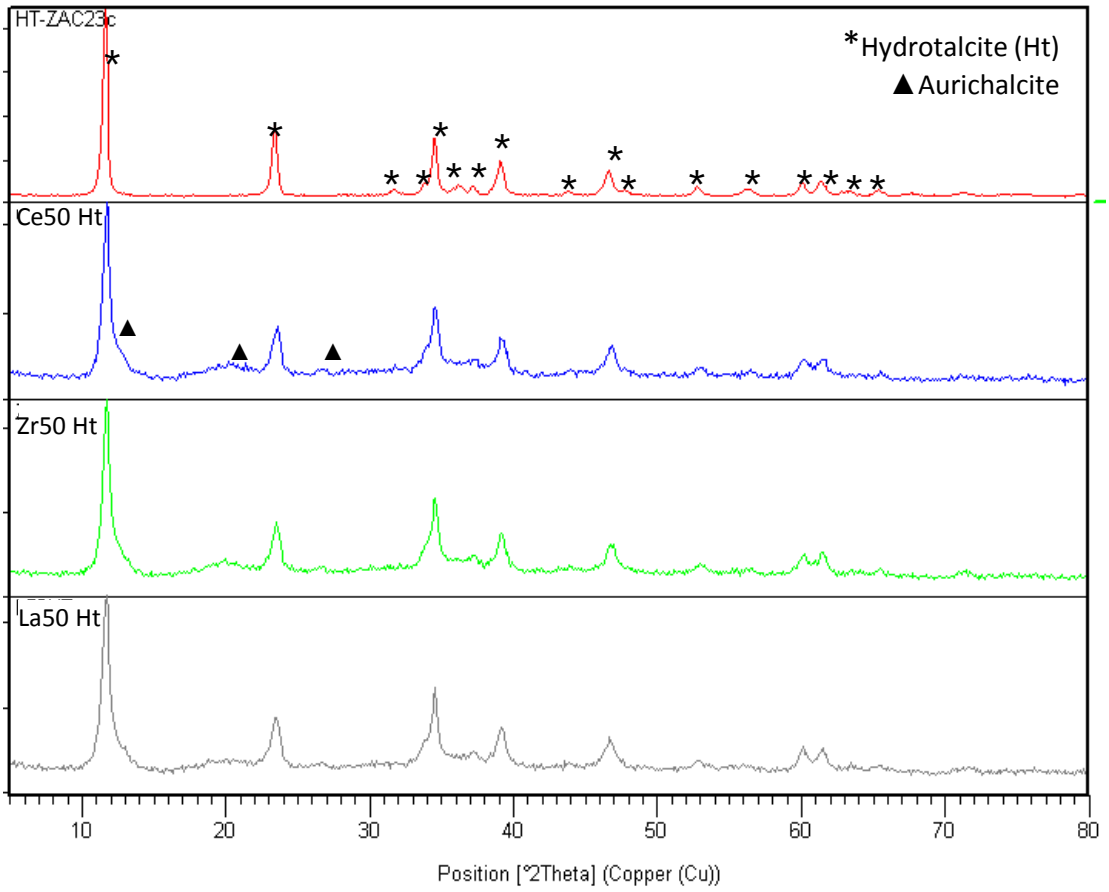

Figure 3.3 XRD pattern of the ZAC23c dried precursors compared to those of the Ce, Zr and La doped systems.

After calcination at 550°C, in all cases the precursors evolve to ZnO, Cu/Zn aluminate and CuO. The addition of doping elements gives rise to a decrease in the crystallinity of the phases obtained (Figure 3.4).

The lower crystallinity measured is accompanied by an improvement of the physical properties. In fact, after doping an increase of the surface area is observed (Table 3.3). Furthermore, all doped catalysts show higher Cu dispersions.

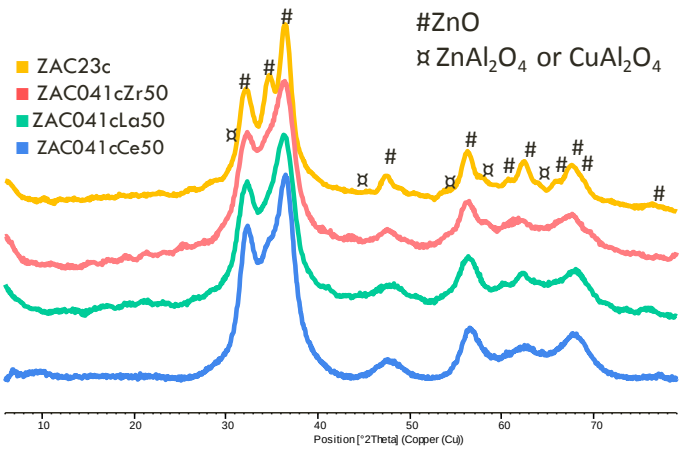

Figure 3.4 XRD pattern of the calcined doped catalysts, compared to those of ZAC23c catalyst.

Sample	BET Surface area (m^2/g)	Cu surface area (m^2/g_{cat})	Cu surface area (m^2/g_{Cu})	D_{Cu} (%)	Cu particle size (nm)	Pore volume (cm^3/g)	Pore size (nm)
ZAC23c	48	4.9	24.5	3.8	27	0.35	28
ZAC23cLa50	70	8.5	42.4	6.5	16	0.36	16
ZAC23cCe50	58	8.3	41.1	6.3	16	0.35	19
ZAC23cZr50	76	9.1	45.7	7.0	15	0.39	20

Table 3.3 Physical properties of the doped catalysts, compared to those of ZAC23c catalyst.

These results are confirmed by TPR analysis, performed on the calcined catalysts (Figure 3.5). The temperature of the observed peaks may be correlated to the reduction of Cu-containing species based on the literature (Table 3.4).

Species	T [°C]	Description	Reduction steps
Low interacting CuO	160-250	Small particles highly dispersed	$Cu^{2+} \rightarrow Cu^{+}$
			Cu^{2+} or $Cu^{+} \rightarrow Cu^{0}$
CuO	250-350	CuO strongly bounded with ZnO or big CuO particles	Cu^{2+} or $Cu^{+} \rightarrow Cu^{0}$
Cu-containing spinel	400-700	Cu^{2+} in oxides matrix	$Cu^{2+} \rightarrow Cu^{0}$

Table 3.4 Cu-species temperature reduction.

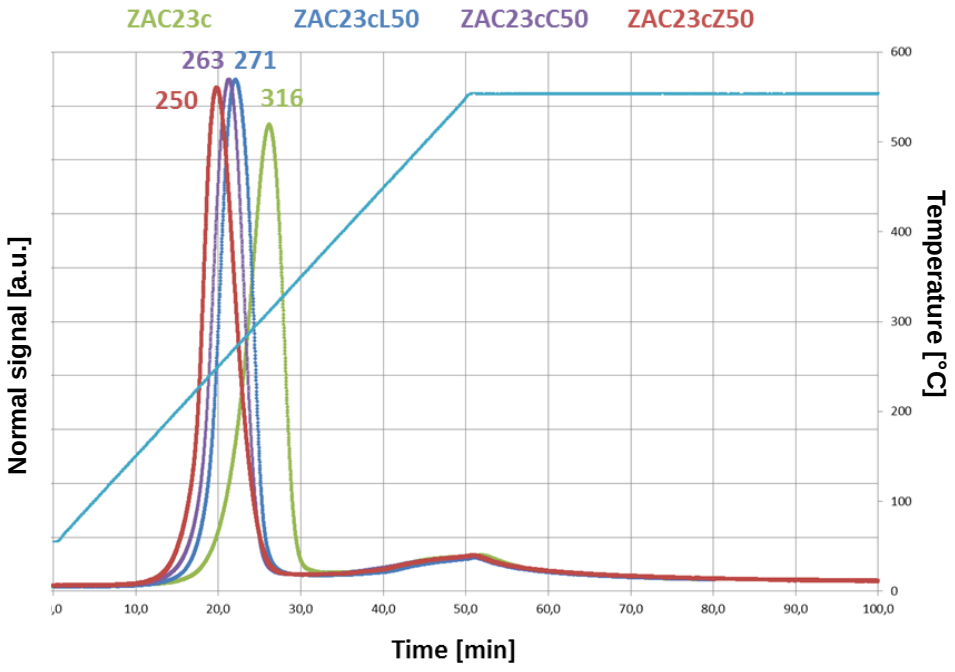

Figure 3.5 TPR analysis results of the calcined doped catalysts, compared with that of ZAC23c.

In the TPR analysis of ZAC23c catalyst it is possible to observe a single peak centered at 316°C corresponding to the reduction of CuO particles on the catalyst surface. In the doped systems, a decrease in the reduction temperature is observed, that may be correlated to the reduction of CuO particles characterized (such as verified by N_2O chemisorption analysis) by lower size, i.e. to a higher Cu dispersion obtained by doping.

To point out the effect of the addition of La, Zr and Ce on the thermal stability, all the samples were calcined at increasing temperature. In Figure 3.6 are reported the values of the surface areas as a function of the calcination temperature for the doped catalysts, compared to the undoped one. As already observed for the samples calcined at 550°C, doped catalysts show higher surface area values compared to ZAC23c catalyst. The surface area decreases by increasing calcination temperature until 650° with different rates: surface area of samples doped with La and Zr decrease faster than those of the sample doped with Ce and the reference one. At 950°C all the samples show the same surface area, while in the range of temperature between 650 and 950°C, Ce doped and reference catalysts maintain surface area values higher than La and Zr doped ones.

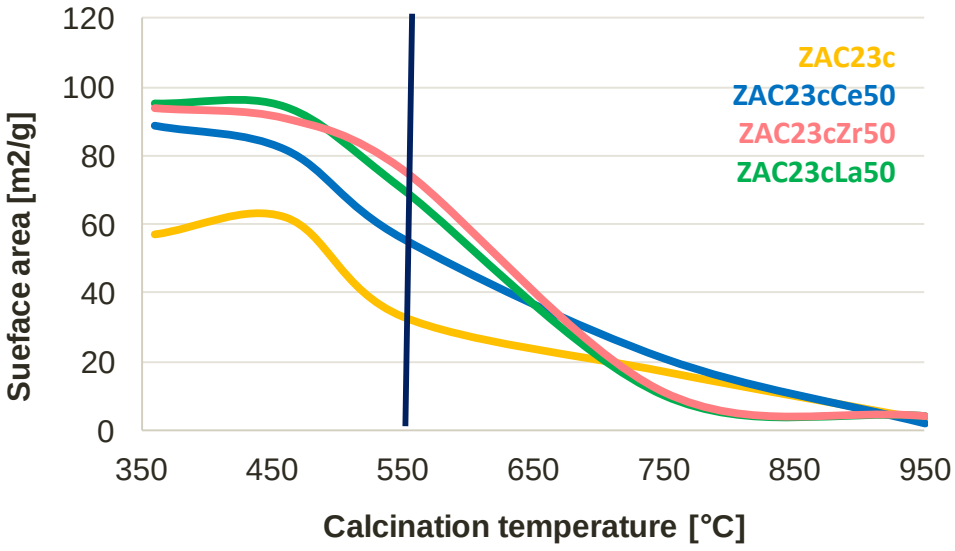

Figure 3.6 Surface areas measured for the different undoped and doped catalysts as a function of the calcination temperature.

All the catalysts tested in MTS reactions have been calcined at 550°C.

In Figure 3.7 are reported the CO conversion values obtained in each test for all the catalysts, by increasing the temperature with a S/DG value of 0.55v/v and a contact time of 0.5 s. All the doped catalysts show higher activities respect to that of the reference catalyst ZAC23c. By increasing of temperature until 300°C all the catalysts reach equilibrium conditions.

Best results at 250°C have been observed with the Ce doped catalyst. By increasing of the contact time (figure 3.7 C) a general increase in the CO conversion is observed for all the catalysts.

In figure 3.7 B are reported the results of the tests performed in the most stressing conditions, with the S/DG value of 0.25v/v. In this case, the effect of dopant addition changes as a function of the element added. In case of ZAC23cZr50 catalyst, the catalytic performances remain comparable with those of the reference catalyst, while La leads to a detrimental effect on the CO conversion. Only the sample containing Ce shows an increase in activity, mostly at 250°C.

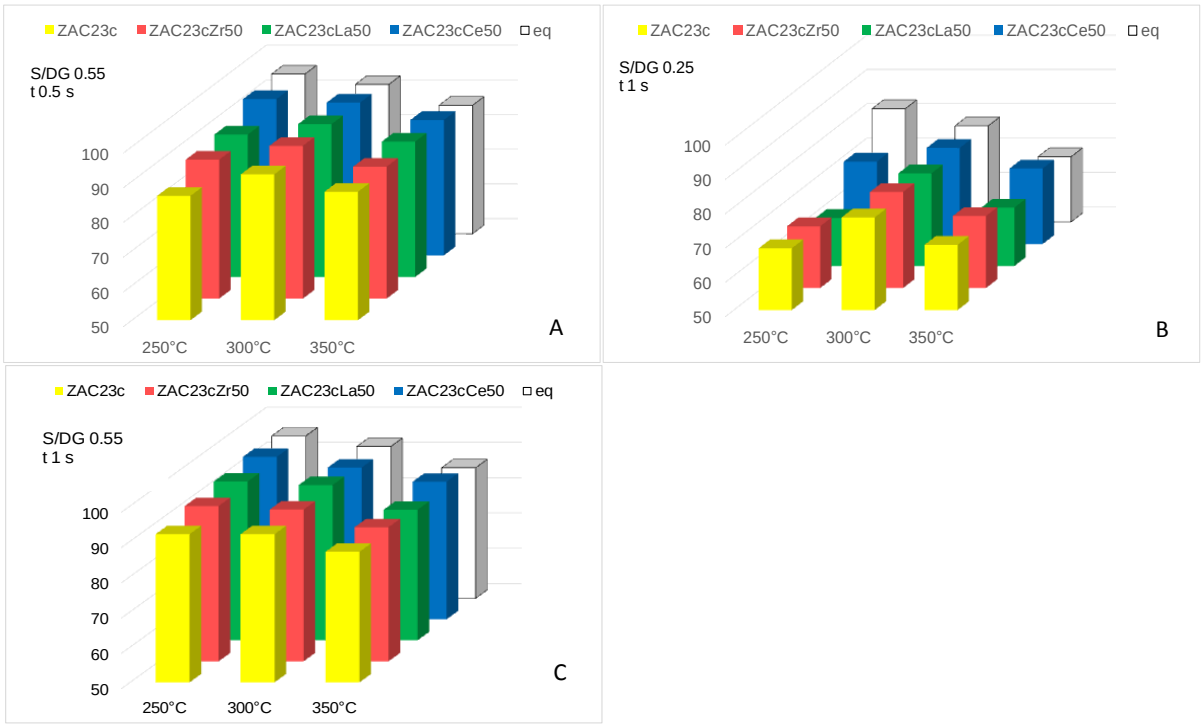

Figure 3.7 Activity and deactivation of ZAC23c doped catalysts compared to the reference one.
A S/DG= 0.55v/v, t= 0.5s
B S/DG = 0.55v/v, t= 1s
C S/DG = 0.25v/v, t= 1s

The improvement in the catalyst performances may be correlated both to the physical and chemical properties. In fact, the doped catalysts are characterized by higher surface area and Cu dispersion, which may justify the increase in the CO conversion.

At the same time, the addition of Ce results in a best catalytic behavior compared to Zr and La, although in the former case the surface area is lower and the distribution of Cu particle size comparable.

The increase in the activity observed for the doped catalysts is strictly correlated to the stabilization of the Cu particles (Figure 3.8).

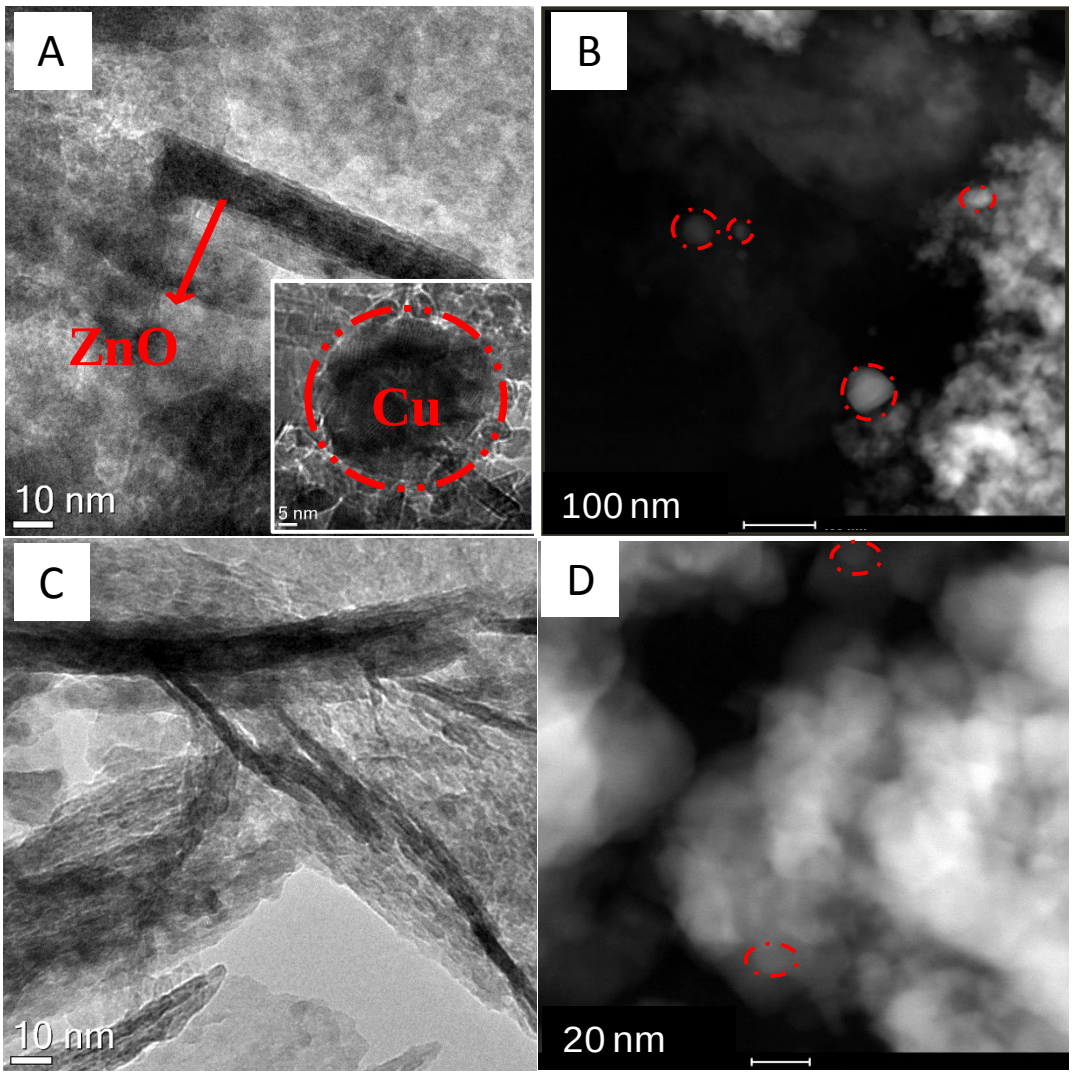

Figure 3.8 TEM analysis performed on ZAC23c calcined (A) and spent (B) compared with ZAC23cLa50 calcined (C) and spent (D).

As observed by TEM analyses, calcined reference catalyst (Figure 3.8 A) is characterized by very crystalline ZnO accompanied by CuO particles of about 20 nm. The introduction of La (Figure 3.8C), as well as Zr and Ce (not reported), leads to a better dispersion of Cu, and CuO particles are not more detected (Figure 3.8C).

The presence of a layered oxide phase, derived by topotactic decomposition of the hydrotalcite-type precursor (Figure 3.8C) may be detected. After reaction, the Cu particles of the doped systems remain smaller than those of the un-doped one (Figure 3.8B and D). The ZnO takes part to the WGS reaction stabilizing the intermediates formed on the metal surface by spillover and increasing the TOF. The high metal dispersion gives rise to an improved interaction between Cu and ZnO, which contributes to increase the catalyst activity.

The increase in the crystallinity of ZnO domains may negatively affects its role in the reaction pathway and the resulting specific surface area.

The role of Ce in increasing the activity of the Zn/Al/Cu system may be ascribed to the peculiarity of CeO_2 of intra-lattice oxygen mobility and its high oxygen storage capacity. The presence of a Ce^{4+}/Ce^{3+} redox pair may have beneficial effect in WGS reaction promoting the redox mechanism. Oxygen atoms may be easily transferred in the surface Ce oxide structures via the quick and reversible redox couple. The redox mechanism, which generally occurs at high temperature, may be favored also at low temperature by the presence of Ce cations in the catalyst lattice. Furthermore, the formate decomposition may be realized on catalysts with higher O-mobility [5]. Several studies show that the addition of Ce increases the capability of water adsorption and splitting into –O and –OH species [6].

The high catalytic activity at low temperature of doped systems are not enough for a possible industrial scale up if not accompanied with a long-term stability. Accelerated thermal aging test, consisting in a multiple heating-cooling reaction cycles have been carried out (Figure 3.9) in order to obtain information about the stability of the catalysts. Starting at 300°C, the catalyst undergoes to reaction for 1h with a S/DG of 0.25v/v then it is heated until 500°C and hold for 1h. After this first reaction step the reactor was cooled until the starting temperature under nitrogen flow, then keeping constant conditions for 1h again. This heating-cooling step was repeated for a total of 24h. To evaluate the deactivation, the CO conversion was measured at the beginning and at the end of the whole cycle.

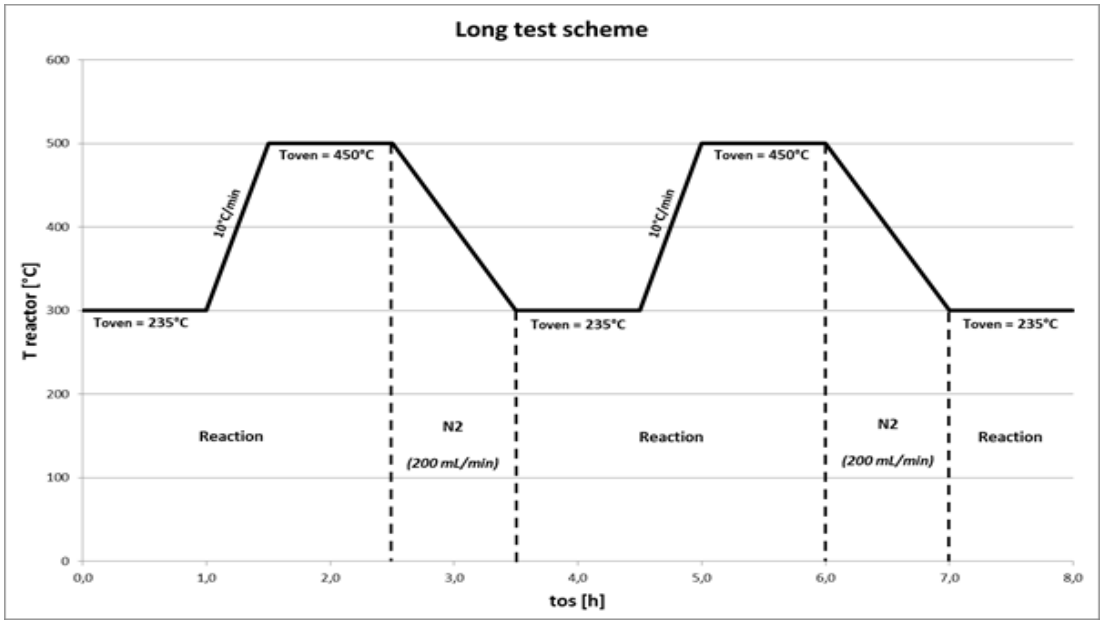

Figure 3.9 Aging test procedure.

In Table 3.5 are reported the CO conversion measured at the beginning and at the end of the 24h test for the reference ZAC23c and the doped catalysts.

All doped catalysts show a higher resistance in WGS reaction conditions. Ce-containing sample results the best catalytic system, showing both best activity at low temperature and best stability also in accelerated aging tests.

Catalyst	Starting %CO converted	Final %CO converted	%ΔCO conversion
ZAC23c	77	62	19
ZAC23cLa50	77	67	13
ZAC23cZr50	78	69	11
ZAC23cCe50	78	74	5

Table 3.5 CO conversion obtained for the reference ZAC23c catalyst and for the La, Zr and Ce doped catalysts

3.1.2 Conclusions

In the first part of this work, an active Cu/Zn/Al catalyst active in MTS condition was synthesized. To improve the activity and stability, the composition was modified by addition of dopant element. The addition of La, Ce and Zr to the reference ZAC23c catalyst gives rise to changes in physical and activity properties.

In particular, regardless the improve obtained for all systems in terms of surface area and Cu dispersion, the better CO conversion was observed for the Ce doped catalyst. The high intra-lattice oxygen mobility and the high oxygen storage capacity of Ce ions may promote the redox mechanism for the WGS reaction, enhancing the reactivity.

Furthermore, the promising results obtained in terms of stability of the catalysts under reaction conditions may be the starting point for a possible scale up of the process, optimizing the overall parameters.

3.1.3 Mg an Ba addition: effect on the catalytic activity

Considering the same ZAC23c catalyst, another important parameter to investigate is the role of basicity on the catalytic behavior. The modulation of basicity of samples has been realized by the addition of different amount of Mg to the catalyst formulation. The positive effect of Mg both on the CO conversion and Cu dispersion was also reported by several authors [7,8,9]. The catalyst composition was modified by partial substitution of Zn with Mg with a weigh content between 3.75 and 15.89 wt%, maintaining the M^{2+}/M^{3+} ratio (mol/mol) constant. Catalyst prepared by Mg doping, which compositions are reported in Table 3.6, are named including the Zn/Mg molar ratio.

Catalyst	Cu (wt/wt)	Zn (wt/wt)	Mg (wt/wt)	Al (wt/wt)	M^{2+}/M^{3+} (mol/mol)	**Zn/Mg** (mol/mol)
ZAC23c	20.0	46.3	0.00	9.2	3	0.00
ZAC23cM4	20.0	40.4	3.75	9.8	3	4.00
ZAC23cM1	20.0	29.3	10.87	10.9	3	1.00
ZAC23cM0.65	20.0	24.4	13.96	11.3	3	0.65
ZAC23cM0.5	20.0	21.4	15.89	11.6	3	0.50

Table 3.6 Catalysts compositions of the Mg ZAC23c catalysts.

Both dried precursors and calcined samples were characterized by XRD analysis. In all dried materials it is possible to see the presence of an hydrotalcite-type phase (Figure 3.10). In the sample containing the lower amount of Mg (ZAC23cM4) an aurichalcite phase may be also detectable. By increasing the Mg content it is possible to observe a change in the intensity of the peaks of the hydrotalcite-type phase, with a decrease in the intensity of the peaks at low 2°Theta values and an increase of that of the peaks al higher 2°Theta values. This effect may be attributed to the embedding of the Mg^{2+} ions in the structure.

After calcination at 550°C, the hydrotalcite-type phases evolve into mixed oxides structures (Figure 3.11); the main effect of the Mg addition is a dramatic decrease of the crystallinity.

The main phase detected is ZnO, presents in all samples, while presence of MgO may be observed in the XRD spectra of ZAC23cM1, ZAC23cM0.65 and ZAC23cM0.5 samples, i.e. those with the higher Mg content.

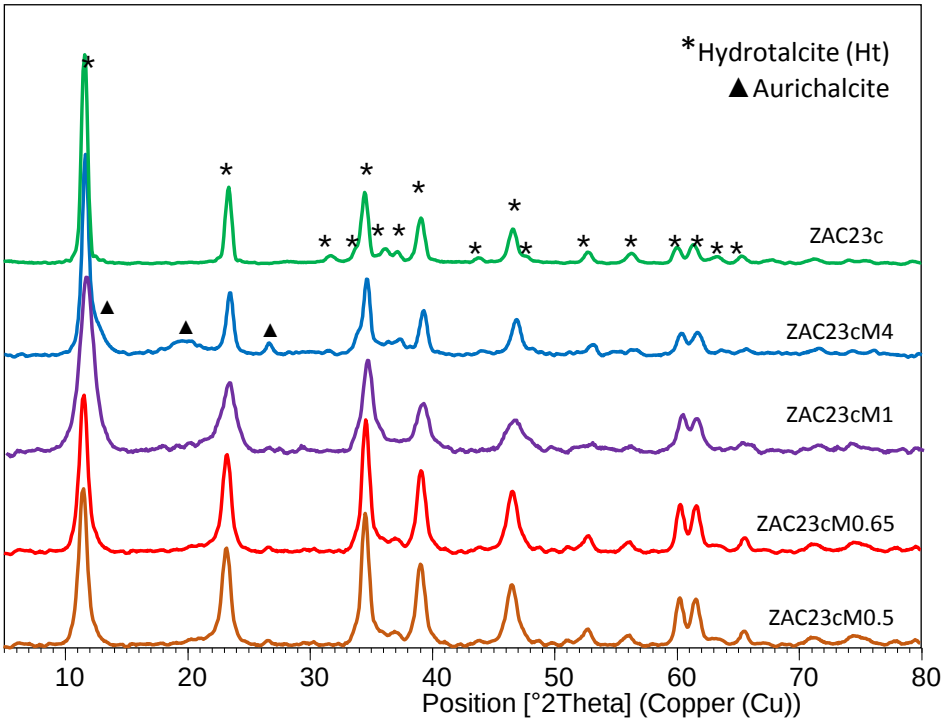

Figure 3.10 XRD patterns of the ZAC23cMx dried precursors.

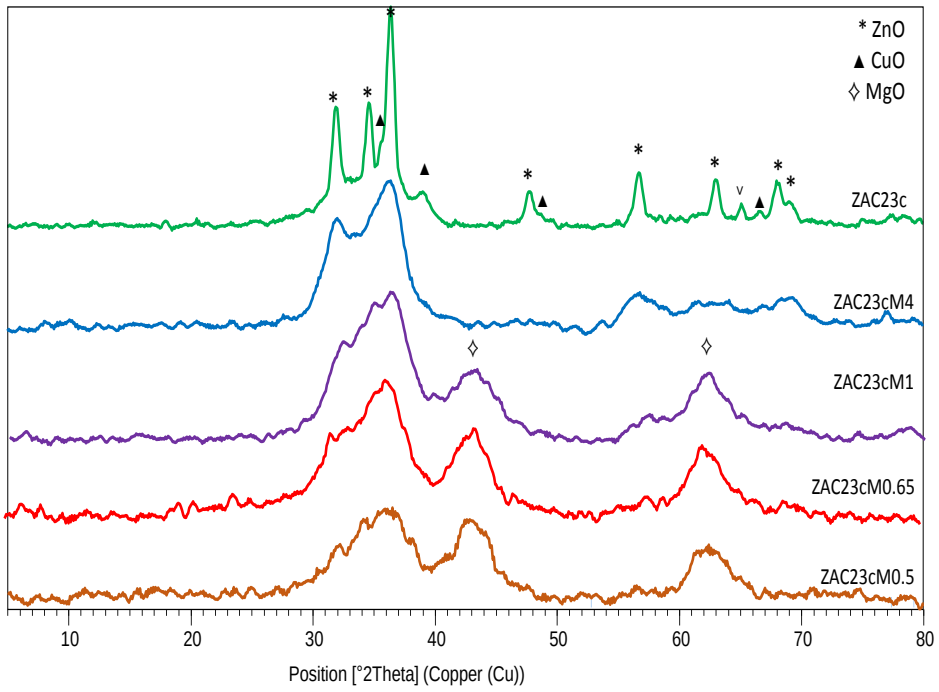

Figure 3.11 XRD patterns of the calcined ZAC23cMx catalysts.

The introduction of Mg in the formulation gives rise to positive effects in terms of specific surface area and Cu distribution. (Table 3.7). In fact, the Mg added increases the surface area and decreases the average pore size; the surface area value shows present a maximum for the ZAC23CM1.00. The same trend may be observed for the Cu dispersion.

Catalyst	Phases	BET Surface area (m^2/g)	Cu surface area (m^2/g_{cat})	Cu surface area (m^2/g_{Cu})	DCu (%)	Particles size (nm)	Pore size (nm)
ZAC23c	ZnO	48	4.9	24.5	3.8	33	28
ZAC23cM4.00	ZnO	64	8.5	42.4	6.5	16	19
ZAC23cM1.00	ZnO	95	13.8	68.8	10.6	10	9
ZAC33cM0.65	ZnO;MgO	71	10.8	55.0	8.3	12	11
ZAC33cM0.50	ZnO;MgO	81	10.1	49.8	7.7	13	13

Table 3.7 Physical properties of the calcined ZAC23cMx catalysts as a function of Mg amount added.

From TPR analysis, it is possible to see a single reduction peak for all the catalysts, correlated to the reduction of CuO particles (Figure 3.12). All the Mg doped catalysts show an increase of the reducibility, in terms of reduction temperature. The decrease in the temperature is not linear with the Mg content, but it may be correlated to the Cu dispersion; higher is the dispersion of the metal on the surface and higher is the temperature, with an effect attributable to a stronger interaction between the Cu-containing phases and the oxide matrix. Under experimental conditions, the reduction of ZnO do not occurred [6].

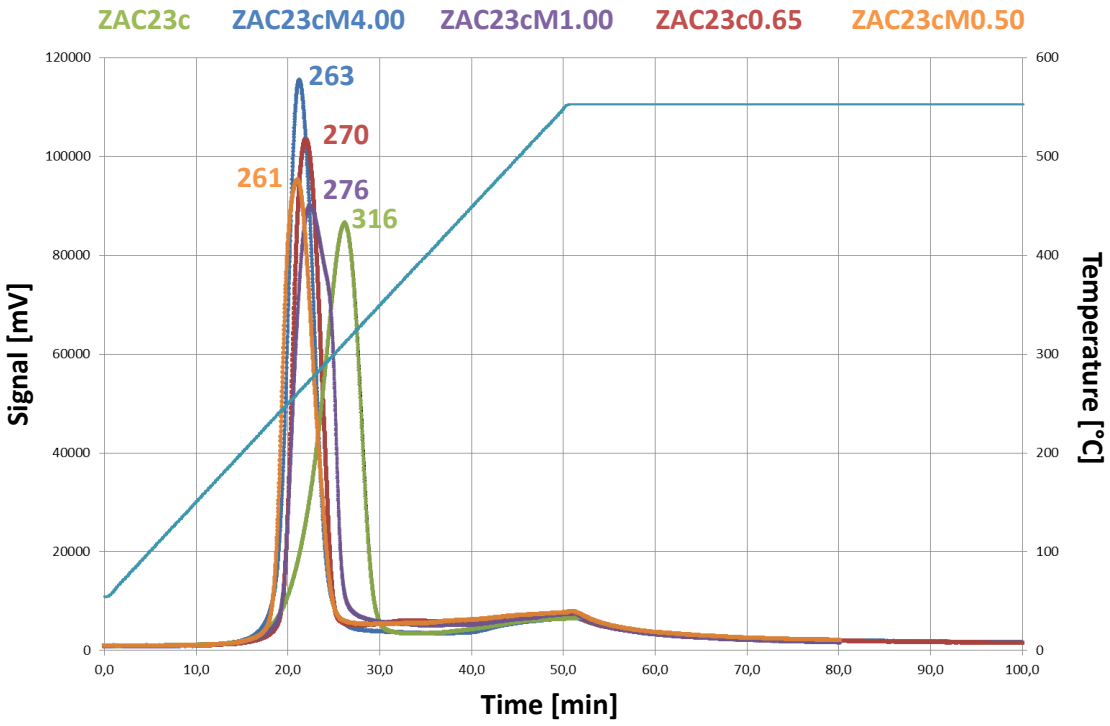

Figure 3.12 TPR analysis of the calcined ZAC23Mx catalysts.

All catalysts were tested in MTS conditions, changing the temperature in the range 250-350°C, with contact time value of 0.5 and 1s and S/DG ratio value of 0.25 and 0.55 v/v (Figure 3.13).

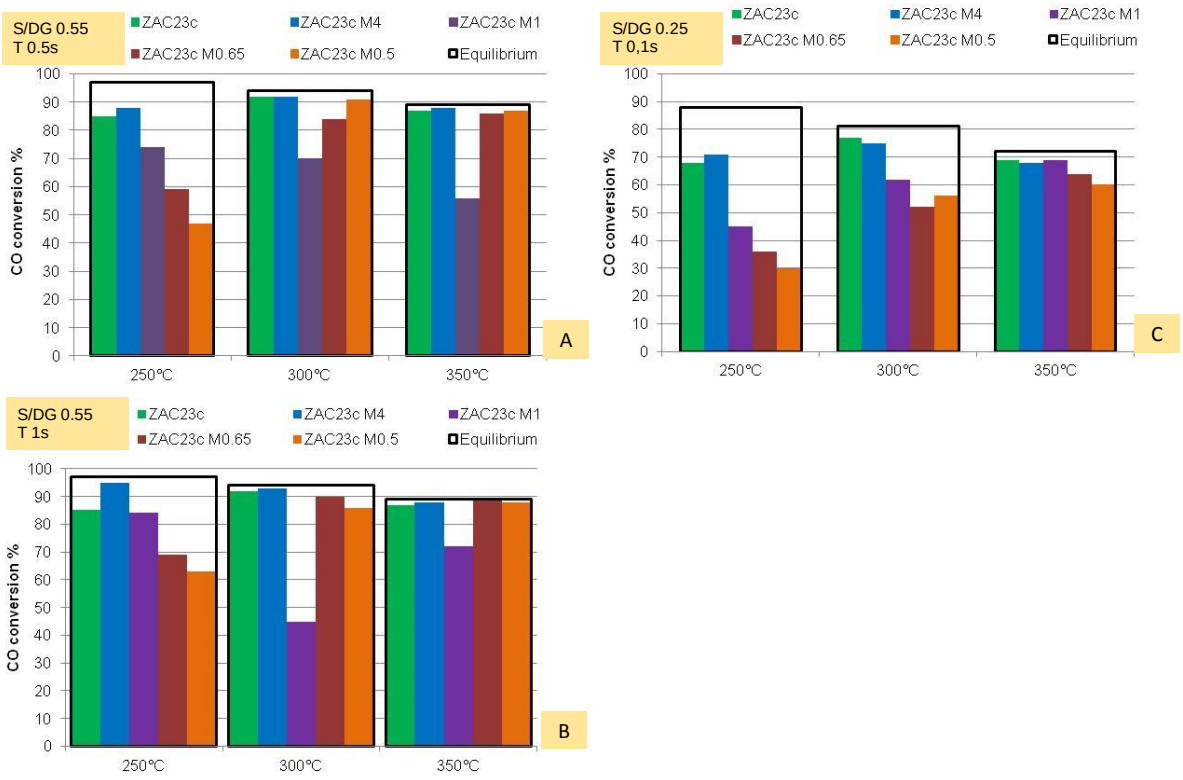

Figure 3.13 Percent of CO converted in the tests performed with ZAC23cMx catalysts as a function of Mg content and reaction parameters.
Figure A S/DG = 0.55v/v, t= 0.5s
Figure B S/DG = 0.55v/v, t= 1s
Figure C S/DG = 0.25v/v, t= 1s

Preliminary tests were carried out changing the temperature with a contact time of 0.25s and a S/DG ratio of 0.55v/v (Figure 3.13 A). At 250°C, after a first increase in the CO conversion observed for ZAC23cM4 catalyst, mainly related to the improved Cu dispersion, the catalytic activity decreases by increasing the Mg content. By increasing the reaction temperature, it may be observed that the CO conversion may be correlated to the reducibility of the Mg doped catalysts; in fact, the trend of the CO conversion is opposite respect to the temperature of the reduction peak.

Increasing the contact time and decreasing the S/DG ratio (Figure 3.13 B-C), it may be observed the same behavior.

It is possible to attribute this effect to the stronger interaction between Cu particles and the oxide matrix when Mg is introduced in the structure that leads to the request of a higher temperature to reach the same activity of the reference catalyst.

ZAC23cM4 catalyst showed the best results in terms of CO conversion also in the test performed at 250°C.

The worst performances are observed for ZAC23cM1 catalyst even if it shows the highest metal dispersion measured on the calcined sample.

Decreasing the steam amount in the feed composition, the same effect was obtained.

Analyzing XRD patterns (Figure 3.14) of spent catalysts (i.e. catalysts after reaction) few considerations can be done:

i) Increasing the amount of Mg decreases the amount of Zn and this results in a decrease of peaks attributed to the ZnO crystalline phase;

ii) Reference catalyst and the doped ones, except the ZAC23cM4 samples, show the presence of Cu^0 species after reaction, accompanied by small traces of CuO, evidencing the formation of large surface passivated Cu^0 particle;

iii) ZAC23cM4 shows the presence of only CuO that may be attributed to the formation of small particles easily oxidized when exposed to the atmosphere during the reactor downloading operations.

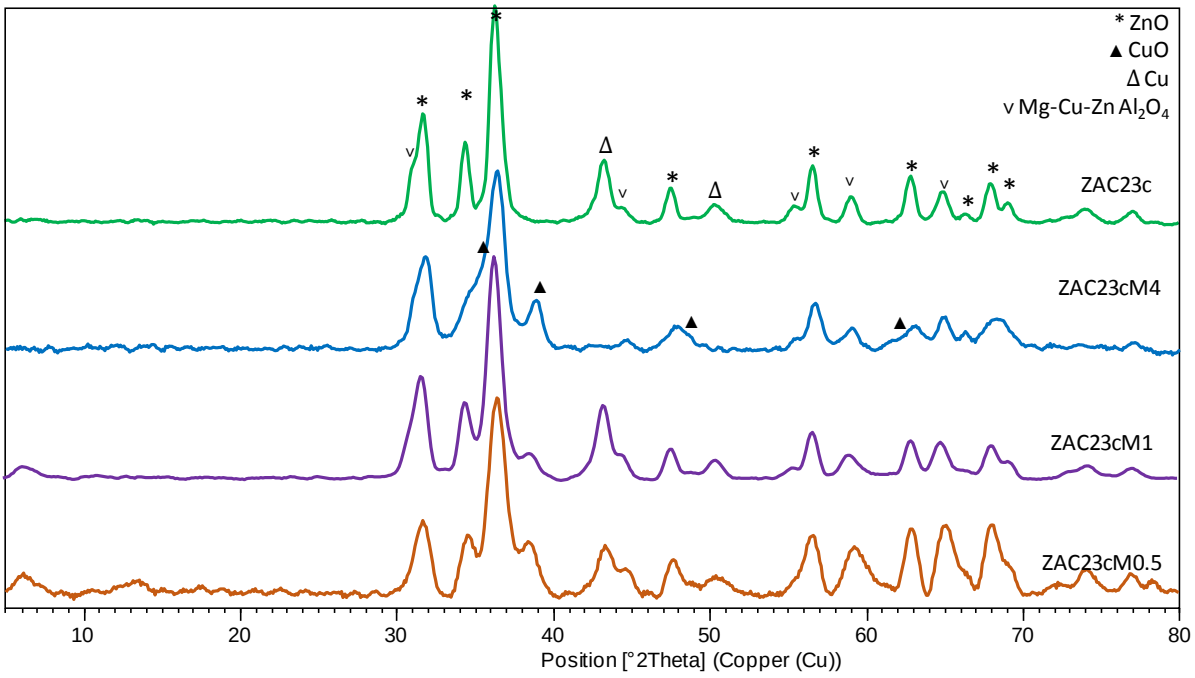

Figure 3.14 XRD patterns of ZAC23cMx catalysts after the catalytic tests.

The considerations evidenced by XRD analysis are confirmed by N_2O chemisorption analyses performed on catalysts after the catalytic tests (Table 3.8). ZAC23cM4 catalyst shows the higher metal dispersion, justifying the best catalytic performances. The introduction of Mg in the catalyst formulation does not promote the stabilization of Cu particles; in fact, the Cu dispersion undergoes a dramatic decrease.

Catalyst	BET surface are (m^2/g)	Cu surface area (m^2/g_{cat})	Cu surface area (m^2/g_{Cu})	D_{Cu} (%)	Pore volume (cm^3/g)	Pore size (nm)
ZAC23c	33	5.1	25.5	2.8	0.35	34
ZAC23cM4	49	8.3	41.7	6.4	0.40	23
ZAC23cM1	41	3.0	14.9	2.2	0.29	16
ZAC23cM0.65	40	5.3	23.5	4.2	0.19	9
ZAC23cM0.5	46	4.3	21.7	3.3	0.21	11

Table 3.8 Physical properties of the ZAC23cMx catalysts after reaction as a function of the Mg amount added.

The increase in Cu dispersion in calcined samples is not correlated to the catalytic activity. During the WGS reaction the Cu particles undergo to sintering phenomena, this is not sufficient to explain the overall catalytic behavior.

Another important effect is the interaction between copper species and mixed oxides forming the structure of the catalysts. The catalytic behavior may be ascribed to the amount of free ZnO in the sample structure, since increasing the amount of Mg decreases the amount of Zn in the catalysts.

Considering the octahedral stabilization energies (P-values) for the Zn^{2+} and Mg^{2+} (-31.6 e -5.0 Kcal/g atomic weigh) [10], it can be assumed that the spinel preferentially formed is $ZnAl_2O_4$. Thus, if the entire Al present in the catalyst formulation forms the aluminate, since alumina phase was not detected in all the catalysts, it is possible to theoretically quantify the total amount of $ZnAl_2O_4$ and ZnO present in each catalyst. In Table 3.9 are reported the calculated molar content of free ZnO compared to the $ZnAl_2O_4$.

Plotting the CO conversion as a function of calculated free ZnO for the tests conducted at T=250°C, S/DG=0.55v/v, τ=0.5s, it is possible to highlight that maximum CO conversion is observed in the samples in which the amount of free ZnO is higher.

Catalyst	Cu (%mol/mol)	Zn (%mol/mol)	Mg (%mol/mol)	$ZnAl_2O_4$ (%mol/mol)	ZnO/Cu (mol/mol)	ZnO/ $ZnAl_2O_4$ (mol/mol)
ZAC23cM0.5	18.2	6.4	37.9	12.5	0.4	0.7
ZAC23cM0.65	18.7	9.7	34.1	12.5	0.6	1.1
ZAC23cM1	19.5	15.2	27.8	12.5	0.9	1.6
ZAC23cM4	21.7	30.1	10.7	12.5	1.5	2.9
ZAC23C	23.1	39.4	0.0	12.5	1.7	3.1

Table 3.9 Molar composition, ZnO/Cu and ZnO/$ZnAl_2O_4$ ratios of the ZAC23cMx catalysts.

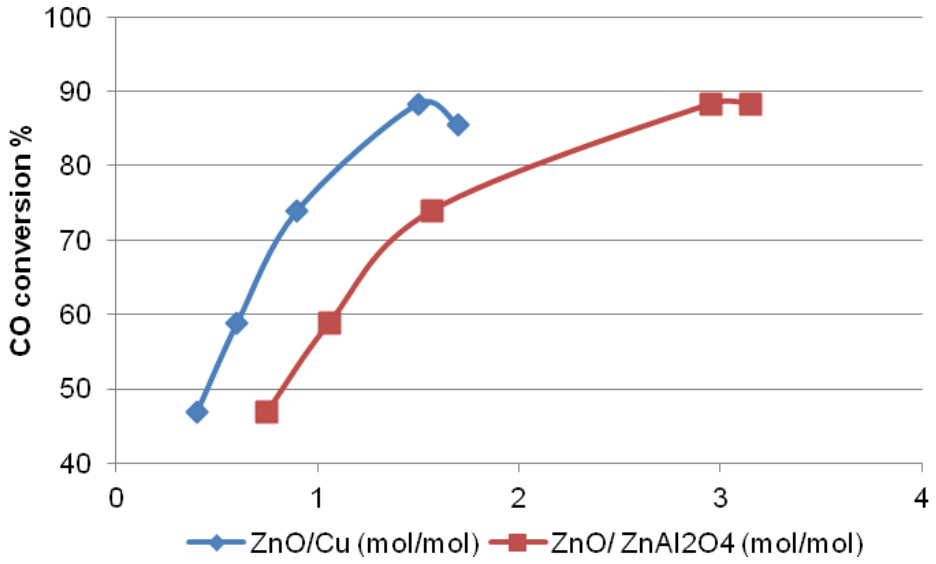

Figure 3.15 CO conversion as a function of Zn/Cu or Zn/$ZnAl_2O_4$ ratios. Test conditions: H_2/CO/CH_4/CO_2 = 72.0/18.8/4.6/4.6 v/v; P = 15 bar; T = 250 °C; S/DG = 0.55; t = 0.5 s

At low temperature, the presence of ZnO is fundamental for the catalytic activity, but the spill-over phenomena reduce with the progressive substitution of Zn by Mg. This effect may be also correlated to the lower reducibility of Mg^{2+} (Mg^{2+}/Mg E°=-2.36V) respect to Zn^{2+} (Zn^{2+}/Zn E°= -0.763V). At 250°C the main contribution to the catalyst activity is given by the Cu particles dispersed into the ZnO matrix.

By increasing the temperature, also the Mg doped materials show interesting properties, but better results were obtained with the catalyst with the lowest Mg content.

In order to point out the rule of the basicity in the catalyst improvement respect to the increase in surface area and Cu dispersion, Mg was substitute by Ba (ZAC23cB4 catalyst).

Ba is characterized by a stronger basicity respect to Mg, but also by a larger ionic radius that do not permit to the metal to be dispersed into the hydrotalcite-type layer [11].

XRD analysis shows that the synthesis route used do not lead to BaO. In the precursor only hydrotalcite-type phase and $BaCO_3$ are observed (Figure 3.16).

During calcination, the hydrotalcite-type phase decomposes to ZnO and Cu-Zn aluminate, while $BaCO_3$ do not undergoes a thermal decomposition. Barium carbonate is more stable than other alkaline-earth carbonates. Complete thermal decomposition of $BaCO_3$ occurs at 1350 °C. Finkelstein studies assumed the existence of a basic carbonate $BaCO_3BaO$ system, obtained by partial decomposition of $BaCO_3$ at about 500°C and stable until 1350°C [12].

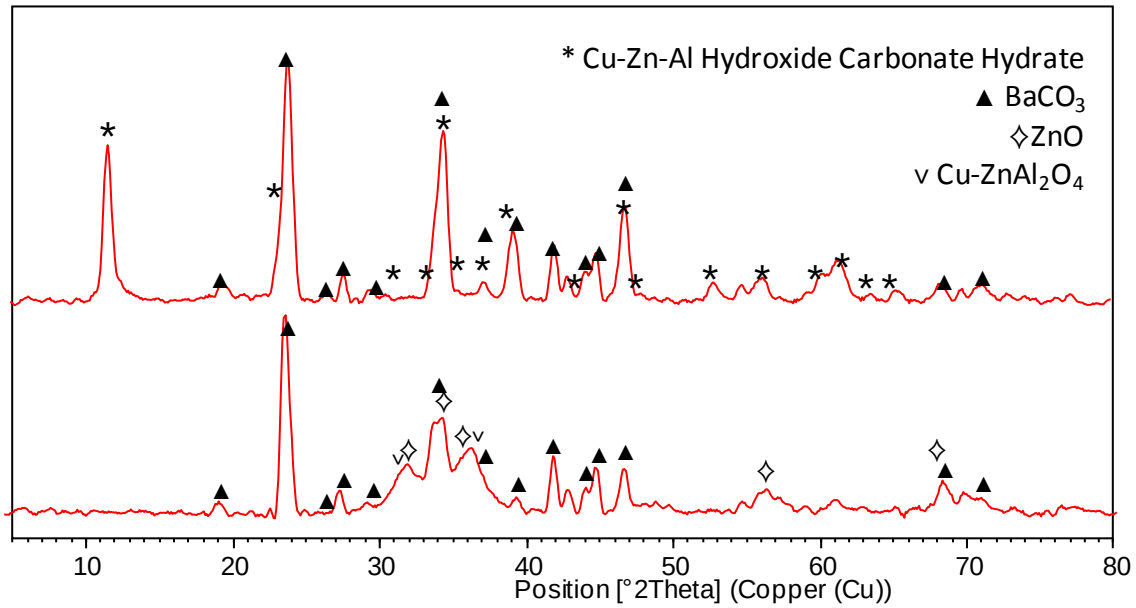

Figure 3.16 XRD patterns of dried and calcined ZAC23cB4 catalyst.

The Ba-doped catalyst shows worst physical properties respect to both undoped and Mg-doped catalyst, while a Cu dispersion, value similar to that of the reference ZAC23c catalyst are observed, showing that the presence of $BaCO_3$ do not affect the CuO particle formations.

Catalyst	Surface area (m^2/g)	Cu surface area (m^2/g_{cat})	Cu surface area (m^2/g_{Cu})	DCu (%)	Pore volume (cm^3/g)	Pore size (nm)
ZAC23c	48	4.9	24.5	3.8	0.35	28
ZAC23cM4	64	8.5	42.4	6.5	0.45	19
ZAC33cB4	37	4.8	24.1	3.7	0.27	18

Table 3.10 Physical properties of calcined ZAC23c, ZAC23cM4 and ZAC23cB4 catalysts.

TPR analysis performed on the calcined catalysts show, for ZAC23cB4, a single broader peak, characterized by a lower reduction temperature (Figure 3.17). The peak, correlated to the

reduction of CuO to Cu^0, evidences a lower interaction between the Cu-containing phases and the matrix. $BaCO_3$ is not reduced under adopted reaction conditions, with a reduction temperature peak centered at about 800°C [13].

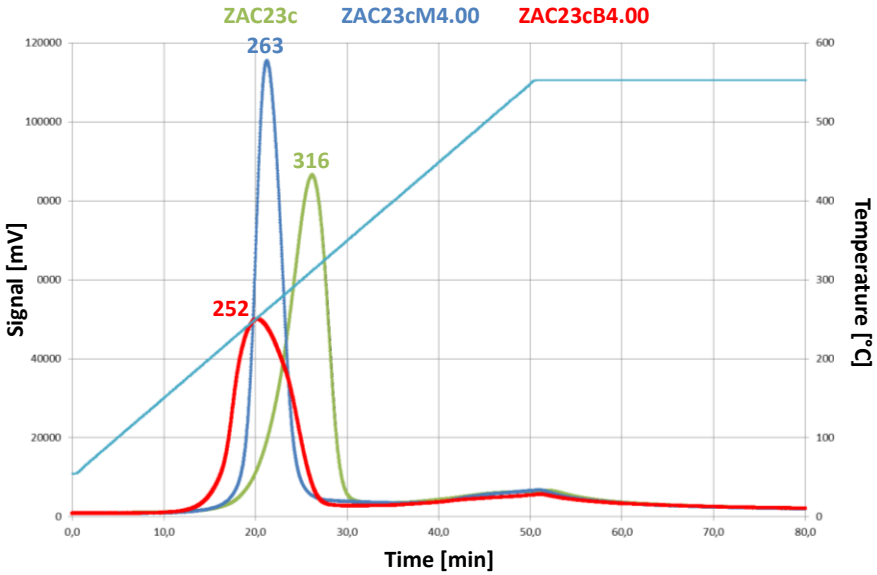

Figure 3.17 TPR analysis of calcined ZAC23c, ZAC23cM4 and ZAC23cB4 catalysts. Effect of the doping on catalyst reducibility.

ZAC23cB4 catalyst was tested in MTS conditions; Figure 3.18 shows the CO conversion obtained, compared with those of ZAC23c and ZAC23cM4 catalysts.

In the tests performed at 300°C and 350°C all the catalysts reach CO conversion equilibrium value, while differences between the three systems may be observed at 250°C.

In test performed with S/DG 0.55v/v and τ 05s (Figure 3.18A), the increase in the catalyst basicity improves the catalytic activity, moving from Mg to Ba-doped catalyst.

By increasing the contact time (Figure 3.18B) the CO conversion observed is similar for both the doped systems; while a reduction of the steam content (Figure 3.18C) points out a slightly higher activity for the Mg doped material.

After reaction, an increase of the crystallinity is observed, with the presence of CuO reflexes (Figure 3.19).

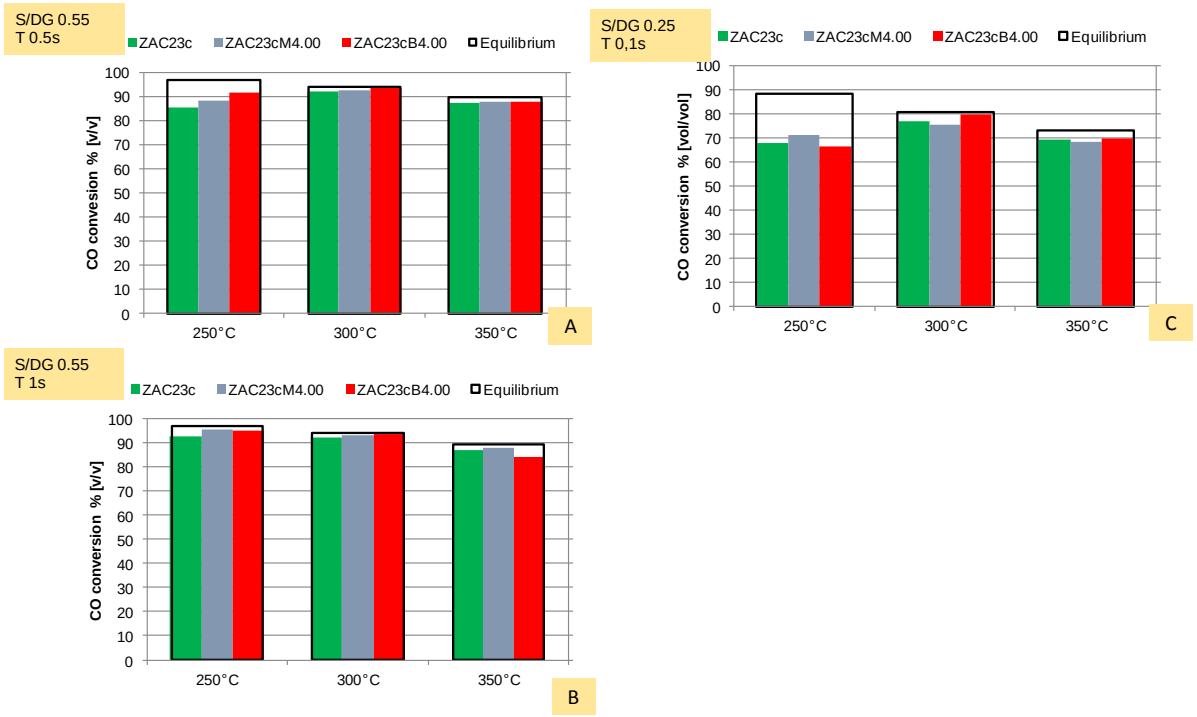

Figure 3.18 Percent CO conversion in tests performed with ZAC23c, ZAC23cM50 and ZAC23cB50 catalysts as a function of Mg or Ba doping and reaction parameters.
Figure A S/DG = 0.55v/v, t= 0.5s
Figure B S/DG = 0.55v/v, t= 1s
Figure C S/DG = 0.25v/v, t= 1s

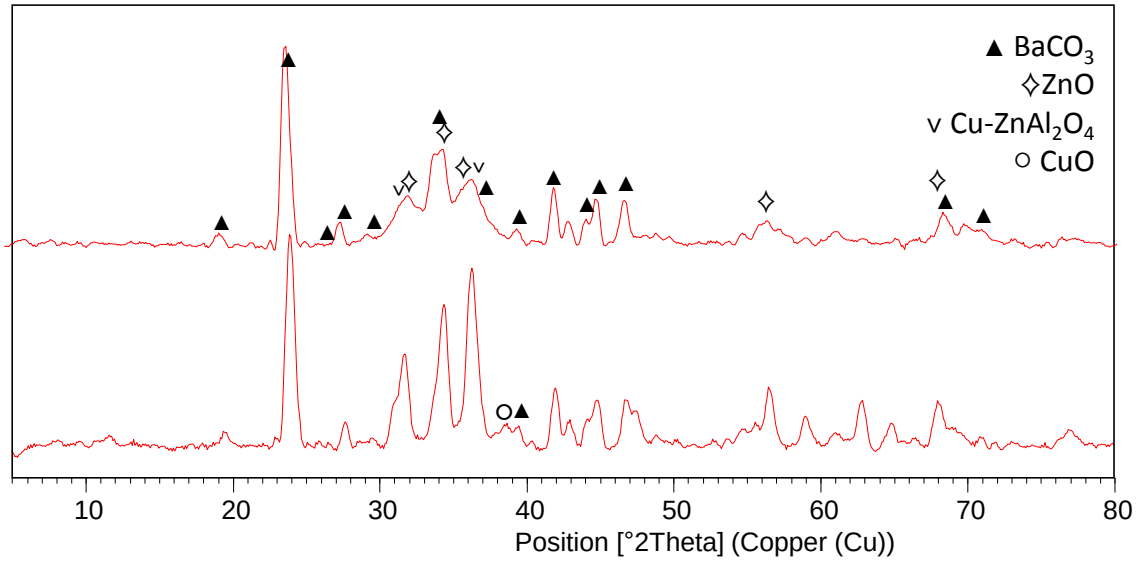

Figure 3.19 XRD pattern of the calcined and spent ZAC23cB4 catalyst.

The basicity does not seems to be directly correlated to the activity of the final catalyst; in fact, considering the physical properties of the different materials, the CO conversion values observed are quite similar.

After the whole catalytic cycle, on the catalysts it was repeated the initial test at 250°C, S/DG 0.55 v/v and τ 0.5 s to evaluate deactivation phenomena (Table 3.11). The Mg containing

catalyst shows the higher activity, which may be ascribed to the higher surface area observed in the spent catalyst.

The ZAC23cB50 catalyst undergoes to the more important deactivation during the catalytic tests; indeed, regardless the starting higher CO conversion, the final activity is the lowest measured. The decrease in the CO conversion observed are not correlated to the physical properties of the materials since all the systems show quite stable characteristics under reaction conditions.

The significant deactivation observed in the ZAC23cB4 catalyst may be attribute to carbon formation on the catalyst surface.

Catalyst	Initial CO conversion [% v/v]	Final CO conversion [% v/v]
ZAC23c	85	78
ZAC23cM4	88	83
ZAC23cB4	92	76

Table 3.11 Decrease in the CO conversion observed for ZAC23c, ZAC23cM50 and ZAC23cB50 catalysts after the whole catalytic cycle

Catalyst	Surface area (m^2/g)	Cu surface area (m^2/g_{cat})	Cu surface area (m^2/g_{Cu})	DCu (%)	Pore volume (cm^3/g)	Pore size (nm)
ZAC23c	33	5.1	25.5	3.9	0.35	34
ZAC23cM4	49	8.3	41.7	6.4	0.40	23
ZAC33cB4	31	4.5	22.3	3.5	0.21	30

Table 3.12 Physical properties of the spent ZAC23c, ZAC23cM4 and ZAC23cB4 catalysts.

3.1.4 Conclusions

The addition of Mg on Cu/Zn/Al systems obtained from hydrotalcitic precursors has different effects. Low amounts of Mg give rise to an improved catalytic activity, correlated to the increase of physical properties and stability of the material. A further increase in the Mg amount leads to a worsening of the catalytic activity and this effect may be ascribed to the interaction of copper species with free ZnO.

The activity after Ba addition is not significantly modified; the different phases and physical properties do not affect the catalytic performances. In this case, the activity seems to be

mainly correlated to the metal content. Furthermore, the Ba doped catalyst have a lower stability under MTS reaction conditions, not correlated to the Cu metal particles stabilization on the catalyst surface.

3.1.5 Coke formation by methylamine decomposition in MTS conditions

Besides the optimization of the catalyst formulation, from an industrial point of view it is very important to minimize or remove the factors that reduce the global plant efficiency.

Coke formation during the reaction may block the pore and the active sites, leading to the deactivation of the catalysts. Generally, coke is mainly formed by Bouduard reaction [14], but this is not the only one way by which it may be produced.

Cu containing catalysts are very active systems, but they also can catalyze alcohols and hydrocarbons formation [15,] according to the reaction pathway reported in Figure 3.20.

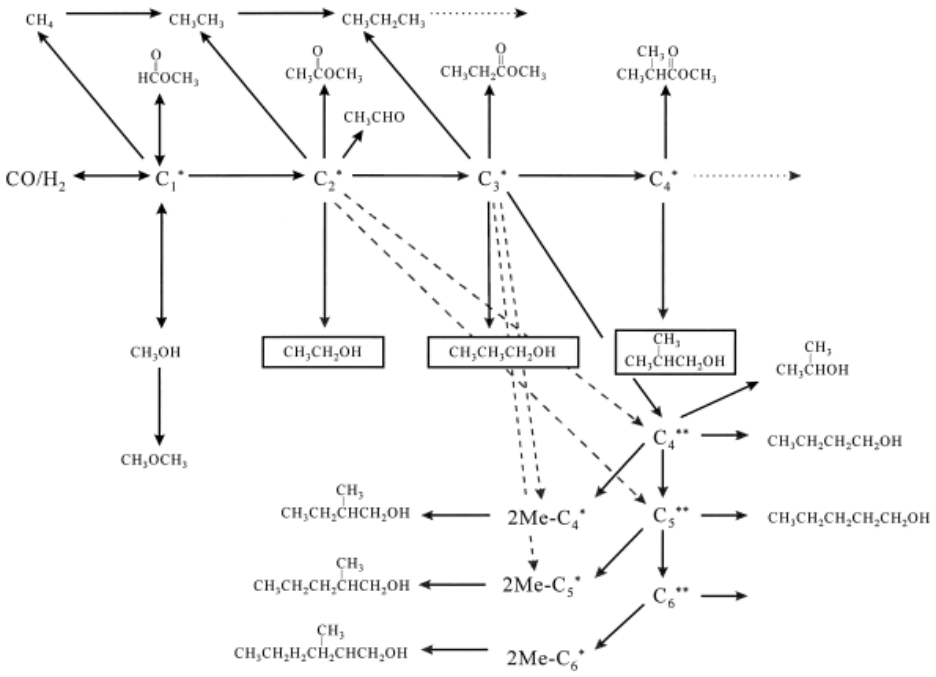

Figure 3.20 Reaction pathway for alcohols and hydrocarbon formation [15].

Alcohols formation is favored at low temperature, because they are molecules unstable at high temperature because undergoing to thermal decompositions.

Other classes of molecules that may be favor the formation of carbonaceous compounds on the catalyst surface are the amines, formed by reaction of NH_3. Industrially, the WGS step follows the Steam Reforming (SR) step where NH_3 may be formed starting from N_2, present as feed impurity.

The ammonia is carried into the WGS process, leading to form MethylAmines (MA); MonoMethylAmine, DiMethylAmine or TriMethyAmine.

MA formed are collected into the non-converted water re-feed to the pre-reforming reactor to improve the plant efficiency.

Due to the high temperature of this step, MA undergoes a thermal decomposition, forming coke [16] which may cause catalyst deactivation, increasing the pressure drop into the reactor and damaging the plant. The decomposition consists of the dehydrogenation of MA up to 500K. The reaction scheme reported below is related to adsorbed amines, although the thermal decomposition occurs also for not absorbed molecules.

$(CH_3)_3N_{ad} \rightarrow (CH_3)_2N_{ad} + C_{ad} + 3H_{ad}$

$(CH_3)_2N_{ad} \rightarrow CH_3N_{ad} + C_{ad} + 3H$

$CH_3N_{ad} \rightarrow CH_2N_{ad} + H\uparrow$

$CH_2N_{ad} \rightarrow N_{ad} + C_{ad} + 2H\uparrow$

$N_{ad} + N_{ad} \rightarrow N_2\uparrow$

Industrially, MA are produced by amination of methanol with ammonia. The reaction works at 400-420°C [15]. The products concentrations (MMA, DMA and TMA) depend on NH_3/MeOH ratio. Reactions involved are reported below. TMA is the thermodynamic favored products, so it may be assumed as an index of the whole amine production.

$MeOH+NH_3 \leftrightarrows MMA+H_2O$ $\Delta G°= -4,13$(Kcal/g mol)

$MMA+MeOH \leftrightarrows DMA+H_2O$ $\Delta G°= -7,24$ (Kcal/g mol)

$DMA+MeOH \leftrightarrows TMA+H_2O$ $\Delta G°= -8,39$ (Kcal/g mol)

The MA synthesis may be catalyzed by several active phases, including the catalysts used in WGS reaction plants, also starting from CO_2-H_2 mixtures rather than methanol. In case of Cu based catalysts, like Cu/Al_2O_3 systems, the reaction pathway followed is the interaction between adsorbed ammonia and an aldehyde intermediate, formed by direct reaction between CO_2 and H_2. Surface acidity is fundamental to define the catalyst activity: in fact, it modulates the adsorption of ammonia favoring the MA synthesis.

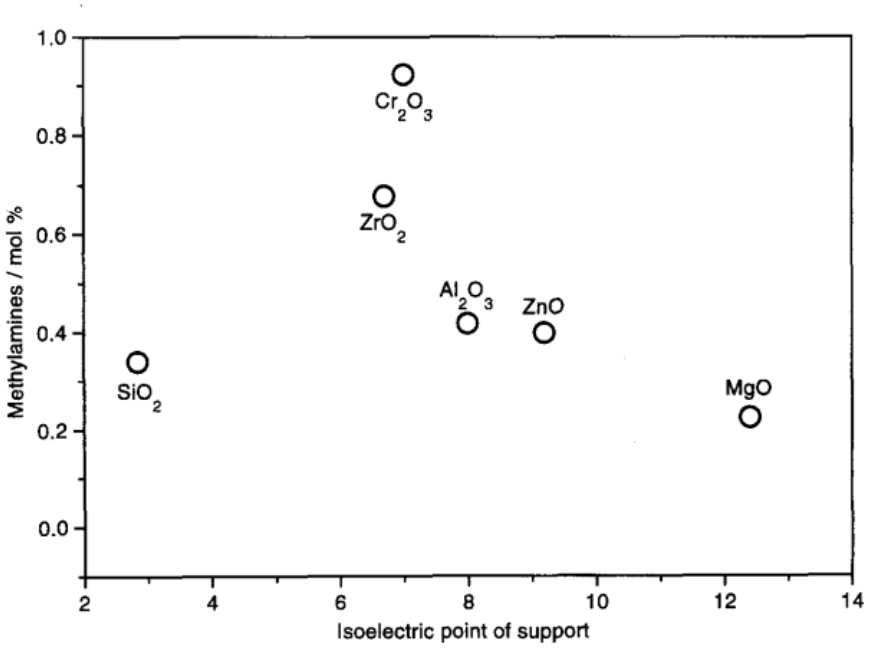

Figure 3.21 Catalytic activity in MA synthesis as a function of isoelectric point of the support (T= 573K, P= 0.6MPa, V 150 cm^3/min CO_2:H_2:NH_3 = 1:3:1 [17].

3.1.5.1 Study of the amine formation on Cu-based catalysts

The effect of reaction parameters on the by-products formations has been studied. In particular, it was examined the production of methanol and MA under MTS conditions.

For this purpose, three different catalysts were compared, two commercials systems and a homemade one. In Table 3.13 are reported the compositions of the catalysts used.

ZAC22c catalysts was prepared by co-precipitation of a hydrotalcite-type precursor (Figure 3.22). On the calcined ZAC22c catalyst, it is possible to observe the formation of ZnO, Cu-$ZnAl_2O_4$ and CuO.

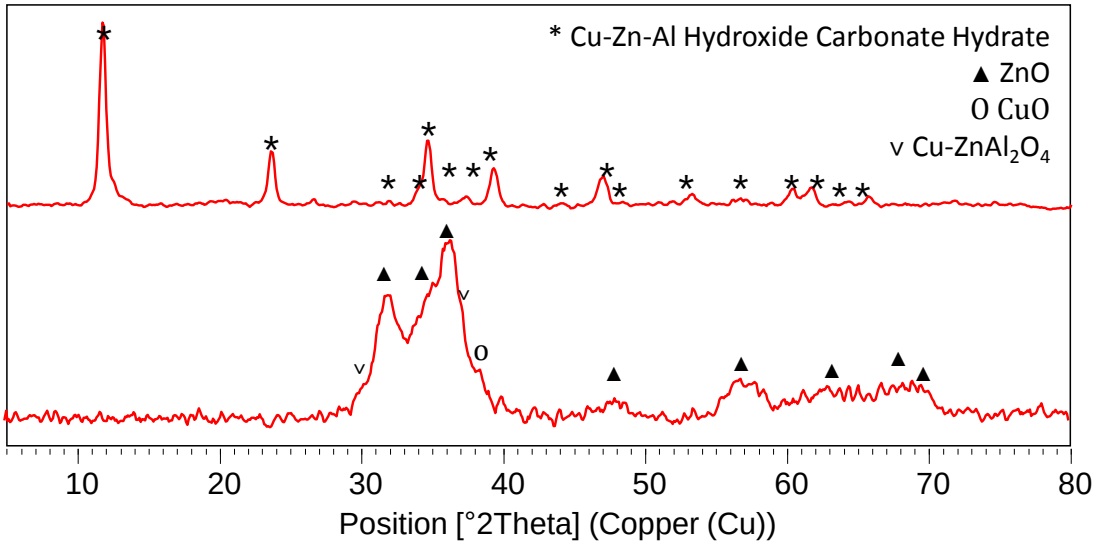

Figure 3.22 XRD pattern of the precursor and calcined ZA22c catalyst.

The two commercial catalysts are characterized by different cupper content, but mainly by a different oxide matrix. In particular, CAT1 contents 19 wt% of Al while CAT2 is composed by 32 wt% of Cr.

Catalyst	Element	Weight content (%wt/wt)
ZAC22c	Cu	20
	Zn	41
	Al	13
CAT1	Cu	26
	Zn	31
	Al	19
CAT2	Cu	16
	Zn	26
	Cr	32

Table 3.13 Weigh composition of ZAC22c, CAT1 and CAT2 catalysts.

XRD analysis performed on calcined CAT1 catalyst show the presence of CuO, ZnO and a spinel phase, containing both Cu and Zn (Figure 3.23). CAT2 shows the presence of ZnO and a mixed oxide spinel phase, which may be ether aluminate or chromate. In both commercial catalysts it is possible to see also the peak attributable to graphite, is added to the catalysts as lubricant in the extruding process.

Comparing the Al containing catalysts, ZAC22c and CAT1, it is possible to see that the commercial one shows lower surface area (Table 3.14), while the Cr-containing one has a similar surface area of the ZAC catalyst.

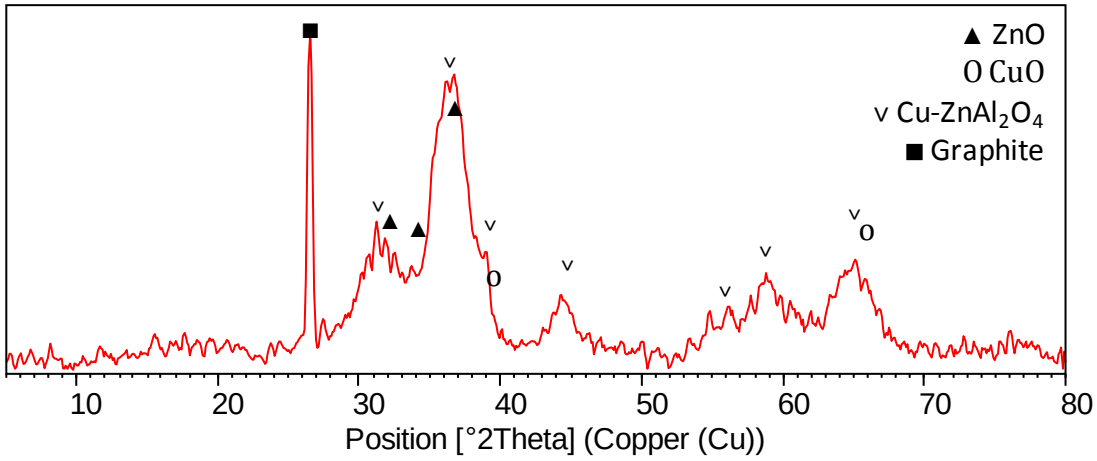

Figure 3.23 XRD pattern of calcined CAT1.

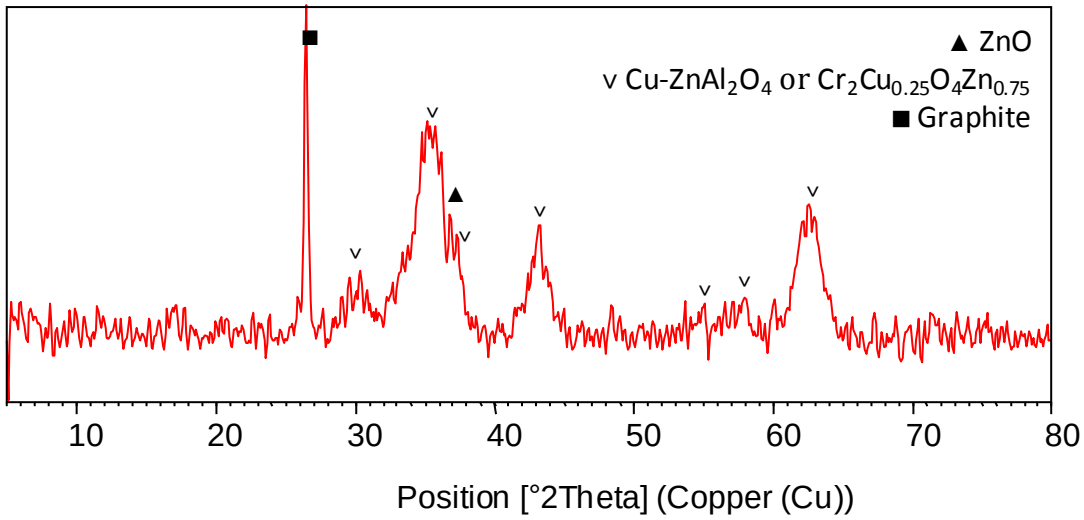

Figure 3.24 XRD pattern of calcined CAT2.

Catalyst	Surface Area BET (m^2/g)
ZAC22c	86
CAT1	117
CAT2	75

Table 3.14 BET surface area of calcined ZAC22c, CAT1 and CAT2 catalysts.

Catalysts have been activated by reduction with a H_2/N_2 stream until 220°C.

Preliminary tests were carried out at 320 and 340°C feeding only demineralized water (DMW). All catalysts showed similar activity at both temperatures (Figure 3.25), with a slightly lower activity observed for the Cr containing catalyst.

On the contrary, some differences may be observed in terms of by-products formation (Table 3.15). ZAC catalyst showed a higher alcohol production than the two commercial systems. Furthermore, also ethanol was produced. This result may be correlated to the greater basicity, due to the higher Zn content; ZnO may stabilizes formate intermediate favoring alcohols formation [18,19,20].

Comparing the results of CAT1 and CAT2, the Cr-containing catalyst (CAT1) gives rise to a higher by-products formation. For all the Al-based catalysts, the alcohol concentration decreases by increasing the temperature. This phenomenon is not evident for the Cr-based system, for which the MeOH concentration remain quite stable also increasing the temperature.

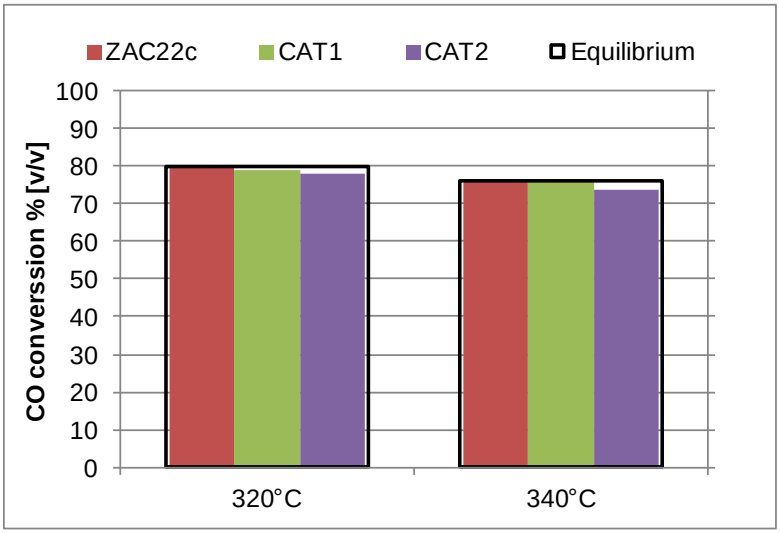

Figure 3.25 Activity of ZAC22c, CAT1 and CAT2 catalyst as a function of temperature (S/DG=0.30 v/v; P=15bar,τ= 3s).

	MeOH (ppm*10^3)		EtOH (ppm*10)	
Catalyst	320°C	340°C	320°C	340°C
ZAC22c	10.9	5.6	10	5
CAT1	3.4	1.7	<d.l.	<d.l.
CAT2	5.8	5.6	<d.l.	<d.l.

Table 3.15 By product concentration measured into the collected unconverted water.

On the same catalysts, have been performed tests feeding an ammonia solution in DMW (8,18E^{-1}g/L) and changing reaction parameters (P=15-20 bar, T=320-340°C, S/DG= 0.30-0.40v/v, τ=03-6 s). It is not worthy that, the increase of the steam content gives rise to a higher ammonia concentration; increasing the S/DG from 0.30 to 0.40, the inlet ammonia molar fraction passes from 2.0E^{-4} to 2.67E^{-4}. To point out only the effect of steam content, the test was repeated reducing the ammonia concentration (from 8.18E^{-1}g/L to 6.61E^{-1}g/L). This test is labelled with (*) symbol.

In Table 3.16 are reported the results obtained in the tests with the ZAC22c catalyst. The effect of reaction parameters on the catalyst performances are pointed out. Test 1 is the reference test in standard conditions; variations to reference conditions in the following tests are highlighted.

After the addition of ammonia to the inlet feed, the CO conversion obtained reach always the equilibrium value, with exception of test 4.

Starting from the reference test, the TMA formation is accompanied by a decrease of the MeOH concentration. The increase of the pressure from 15 to 20 bar (test 2) gives rise to a

higher by-product formation, while the increase of temperature (test 3) leads to the decrease in MeOH and the increase in TMA formation.

Rising the S/DG until 0.40 v/v, alcohols and TMA production decrease, regardless the ammonia inlet molar fraction. Increasing the contact time from 3 to 6 seconds, all the by-products concentrations show an important raise. In general, the increase of the alcohol production matches that of amines.

Test	1	2	3	4	4*	5	6
Pressure (bar)	15	20	15	15	15	15	20
Temperature (°C)	320	320	340	320	320	320	320
S/DG (v/v)	0.30	0.30	0.30	0.40	0.40	0.30	0.30
τ (s)	3	3	3	3	3	6	6
NH_3 water concentration (g/L)	8.18	8.18	8.18	8.18	6.61	8.18	8.18
NH_3 inlet fraction	$2.0E^{-4}$	$2.0E^{-4}$	$2.0E^{-4}$	$2.67E^{-4}$	$2.0E^{-4}$	$2.0E^{-4}$	$2.0E^{-4}$
CO equilibrium conversion (v/v%)	80	80	76	88	88	80	80
CO conversion (v/v%)	80	81	77	73	86	82	81
MeOH ($ppm*10^3$)	7.84	8.90	5.26	3.23	2.95	13.2	12.6
EtOH (ppm)	39	51	43	<d.l.	<d.l.	$132E^2$	$126E^2$
TEA($ppm*10^2$)	1.9	4.3	2.9	1.8	<d.l.	4.5	6.9

Table 3.16 Activity results obtained with the ZAC22c catalyst feeding ammonia solutions.

In tests performed with commercial CAT1 catalyst (Table 3.17), with exception of test 4, the CO conversion measured exceed the equilibrium, as already observed for ZAC22c catalyst. This phenomenon may be correlated to the TMA formation [21] via ether CO or via MeOH. Unlike, for ZAC22c catalyst, the ammonia addition give rise to an increase in the MeOH formation. At the same time, ammonia addition is not followed by TMA formation in the reference test. This result does not exclude MA formation, which may have a different product distribution, with concentrations too low to be detected.

According with the previous results, the increase of the pressure give rise to a by-products increase. Heating the catalyst up to 340°C, a slight decrease in the MeOH production is observed, while TMA concentration remain under the detection limit.

By increasing of the steam content, the effect observed is similar to that observed by increasing the temperature for MeOH. Furthermore, with the highest ammonia molar fraction also the TMA formation may be observed.

Finally, by increasing of the contact time, unlike to that observed for the ZAC catalyst, a general decrease of the by-product formation is observed.

Catalytic results obtained with CAT2 commercial catalyst are reported in Table 3.18. As in case of CAT1, the CO conversions measured overcome the equilibrium values, with the exception of test 3 (after the temperature increase). Again, this may be correlated to by-product formation, accompanied to a lower MeOH production. The increase of pressure is followed by a rise in MeOH, production while surprisingly TMA concentration remain constant. On the contrary, the increase of the temperature does not affect the MeOH production while improves the TMA formation. These results are not trivial, but it is not possible to verify if the changes in the reaction parameters give rise to a different MA distribution, because of the high detection limits of MMA and DMA. Finally, the increase of the steam content reduces the by-products formation, regardless the ammonia inlet molar fraction.

Test	1	2	3	4	4*	5	6
Pressure (bar)	15	20	15	15	15	15	20
Temperature (°C)	320	320	340	320	320	320	320
S/DG (v/v)	0.30	0.30	0.30	0.40	0.40	0.30	0.30
τ (s)	3	3	3	3	3	6	6
NH_3 water concentration (g/L)	8.18	8.18	8.18	8.18	6.61	8.18	8.18
NH_3 inlet fraction	$2.0E^{-4}$	$2.0E^{-4}$	$2.0E^{-4}$	$2.67E^{-4}$	$2.0E^{-4}$	$2.0E^{-4}$	$2.0E^{-4}$
CO equilibrium conversion (v/v%)	80	80	76	88	88	80	80
CO conversion (v/v%)	84	85	81	87	90	85	85
MeOH (ppm*10^3)	4.0	6.2	3.7	2.0	2.3	3.3	5.1
EtOH (ppm)	<d.l.	<d.l.	<d.l.	<d.l.	<d.l.	<d.l.	<d.l.
TEA(ppm*10^2)	<d.l.	6.5	<d.l.	1.5	3.5	3.4	5.5

Table 3.17 Activity obtained with CAT1 catalyst feeding ammonia solution.

Test	1	2	3	4	4*
Pressure (bar)	15	20	15	15	15
Temperature (°C)	320	320	340	320	320
S/DG (v/v)	0.30	0.30	0.30	0.40	0.40
τ (s)	3	3	3	3	3
NH_3 water concentration (g/L)	8.18	8.18	8.18	8.18	6.61
NH_3 inlet fraction	$2.0E^{-4}$	$2.0E^{-4}$	$2.0E^{-4}$	$2.67E^{-4}$	$2.0E^{-4}$

CO equilibrium conversion (v/v%)	80	80	77	87	87
CO conversion (v/v%)	83	85	81	87	90
MeOH (ppm*10^3)	3.7	5.9	3.7	2.7	1.9
EtOH (ppm)	<d.l.	<d.l.	<d.l.	<d.l.	<d.l.
TEA(ppm*10^2)	4.5	4.5	3.6	<d.l.	<d.l.

Table 3.18 Activity obtained with the CAT2 catalyst feeding ammonia solution.

The previous tests seem to indicate a correlation between MeOH and MA formation. To better shed light on the mechanism involved, tests 1 and 2 were repeated co-feeding MeOH ($4.8E^{-2}$ mol/L) to the ammonia solution (tests labeled with m). Results are reported in Table 3.19, Table 3.20 and Table 3.21.

Again, for all the catalysts the overcome of the equilibrium values is observed and it may be attributed to MA formations.

It is worth to note that the addition of MeOH to the feed do not give rise to an increase in alcohols concentration in the collected water. Furthermore, the TMA concentration does not show any dramatic increase by MeOH addition.

In particular, for ZAC22c catalyst (Table 3.19), tests 1 and 1m show similar MeOH concentrations. Probably the alcohols are not stable in the reaction conditions and may decompose. Furthermore, TMA concentration is higher. Increasing the pressure from 15 to 20 bar (1m and 2m) the by-product formation increases.

A similar effect may be observed for CAT1 catalyst (Table 3.20).

For CAT2 the main effect is in terms of alcohol concentration (Table 3.21); MeOH values measured show a higher increase respect to the other catalysts, while TMA content is almost constant.

For all the catalyst, the byproducts formation seems to be more affected to the catalyst characteristics than the feed compositions; the pressure being the main responsible for the MA production.

Test	1 320°C;15bar +NH_3	2 320°C;20bar +NH_3	1m 320°C-15bar +NH_3 & MeOH	2m 320°C-20bar +NH_3 & MeOH
CO equilibrium conversion (v/v%)	80	80	80	80
CO conversion (v/v%)	80	82	82	82
MeOH (ppm*10^3)	7.84	8.90	7.75	9.78
EtOH (ppm)	39	51	71	52
TEA(ppm*10^2)	1.9	4.3	2.2	3.7

Table 3.19 Activity obtained with the ZAC22c catalyst feeding ammonia and methanol solution.

Test	1 320°C;15bar +NH_3	2 320°C;20bar +NH_3	1m 320°C-15bar +NH_3 & MeOH	2m 320°C-20bar +NH_3 & MeOH
CO equilibrium conversion (v/v%)	80	80	80	80
CO conversion (v/v%)	84	85	85	85
MeOH (ppm*10^3)	4.0	6.2	4.0	8.0
TEA(ppm*10^2)	<d.l.	6.5	3.0	11

Table 3.20 Activity obtained with the CAT1 catalyst feeding ammonia and methanol solution.

Test	1 320°C;15bar +NH_3	2 320°C;20bar +NH_3	1m 320°C-15bar +NH_3 & MeOH	2m 320°C-20bar +NH_3 & MeOH
CO equilibrium conversion (v/v%)	80	80	80	80
CO conversion (v/v%)	83	85	85	82
MeOH (ppm*10^3)	3.7	5.9	5.0	9.2
TEA(ppm*10^2)	4.2	4.5	4.9	7.0

Table 3.21 Activity obtained with the CAT2 catalyst feeding ammonia and methanol solution.

The XRD analyses performed on the catalysts after the tests show an increase in the crystallinity. In both Al-containing spent catalysts, the presence of Cu particles is observed, while the Cr-containing one shows peaks attributable to CuO. As preliminary discussed, in spent catalysts CuO is observed when particles are very small, undergoing to complete oxidation during catalyst discharge. In presence of large Cu^0, the metal is only surface passivated, being detected by XRD analysis as Cu^0. Furthermore, both the commercial catalysts are characterized by a more amorphous structure.

After reaction ZAC22c and CAT1 show a decrease in the surface area, while CAT2 shows a higher surface area, confirming the effect of the matrix stability on the physical properties, with better performance for the Cr-containing oxide matrix.

Catalyst	BET Surface Area (m^2/g) Before Reaction	BET Surface Area (m^2/g) Before After
ZAC22c	86	65
CAT1	117	96
CAT2	75	102

Table 3.22 Surface areas of calcined and spent ZAC22c, CAT1 and CAT2 catalysts.

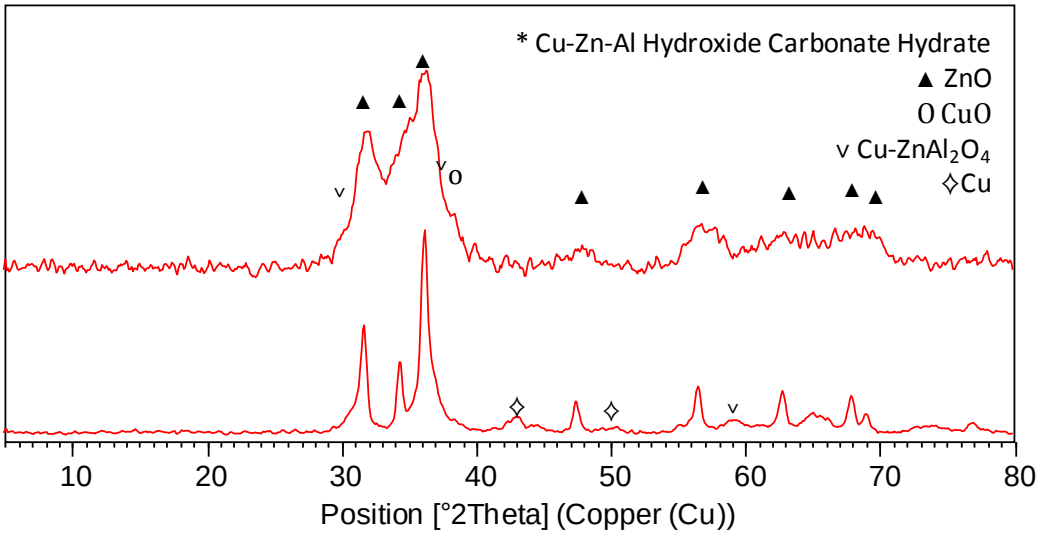

Figure 3.26 XRD pattern of calcined and spent ZAC22c catalyst.

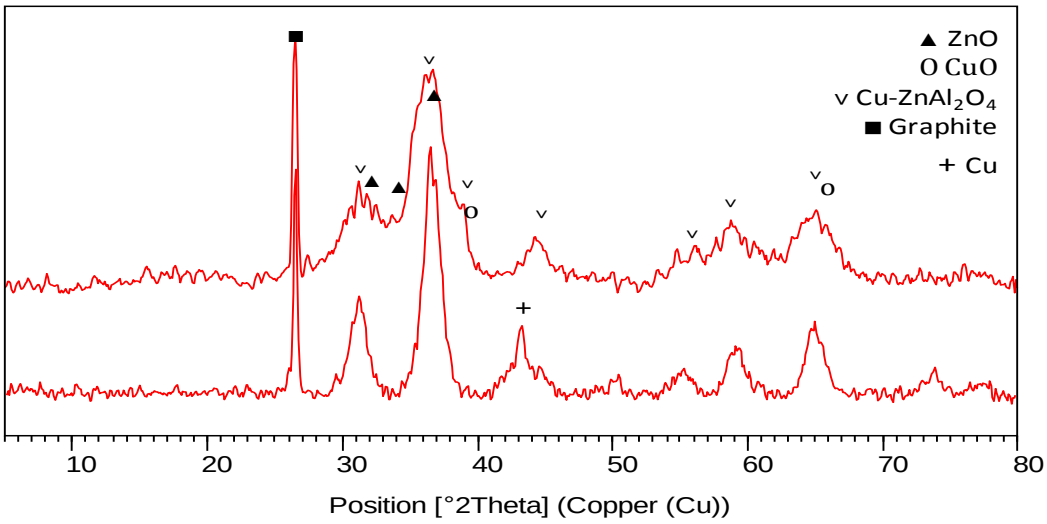

Figure 3.27 XRD pattern of calcined and spent CAT1.

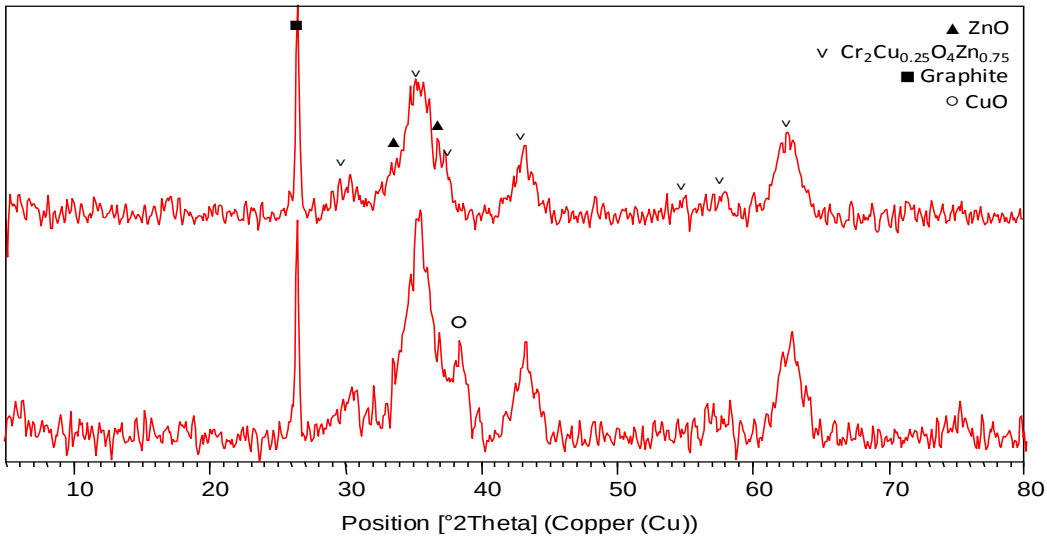

Figure 3.28 XRD pattern of calcined and spent CAT2.

3.1.6 Conclusions

The addition of traces of ammonia to the feed leads to the formation of MA and modify the MeOH formation during WGS reaction at medium temperature. Table 3.23 summarizes the effect of the reaction parameters on the by-products formation observed in the tests performed feeding a diluted ammonia solution.

The Al containing catalysts show similar behaviors, pointing out a correlation between TMA and MeOH formations, with a similar concentration trend for both samples. The raise of the pressure increases the product concentrations. This effect can be correlated to the stronger interaction between reactant and catalyst surface.

On the contrary, the increase of the temperature gives rise to lower productions; since the thermal decomposition of intermediates, like MeOH, may reduce the TMA formations.

Finally, a further steam addition suppresses the side reaction.

For CAT2 the two by-products seem to not be linked by the same reaction pathway, with a concentrations trend different in the case of temperature and pressure variations.

The observed differences may be correlated to the different oxide matrixes, which may differently stabilize the reaction intermediates, modifying the step involved.

Reaction parameter	Catalyst	M^{3+}	MeOH	TMA
↑P	ZAC22c	Al	↑	↑
	CAT1	Al	↑	↑
	CAT2	Cr	↑	Stable
↑T	ZAC22c	Al	↓	↓
	CAT1	Al	↓	<d.l.
	CAT2	Cr	stable	↓
↑S/DG	ZAC22c	Al	↓	↓
	CAT1	Al	↓	<d.l
	CAT2	Cr	↓	↓

Table 3.23 Effect of the increase of P, T and S/DG ratio on the methanol and trimethylamine formations.

3.2 High Temperature Shift catalysts: new promising formulations

Iron-Chromium based material are the most used catalysts in High Temperature Shift (HTS) reaction. As already discussed, several are the reasons for new materials able to replace the traditional catalysts, conferring to the overall process better characteristics in terms of stability, selectivity and environmental.

Low Cu containing Cu-Zn-Al catalysts may represent a good alternative and for this reason have been synthesized, tested as catalysts in HTS reaction and deeply characterized to correlate the physical-chemical properties to the activity.

3.2.1 Synthesis and characterization of Cu based catalyst: ZAC041c

With the aim produce an active and stable catalytic system in HTS reaction, ZAC041c catalyst was synthesized. It is characterized by a Cu content of 4wt% and a Me^{2+}/Me^{3+} molar ratio of 1. Cu catalysts are active in WGS reaction but tend to deactivate because of they suffer of an important metal sintering. The catalyst formulation was defined to optimize the activity/stability of the material.

For this purpose, the amount of Cu has been kept low to avoid sintering phenomena. On the contrary, a high Al content has been adopted to improve thermal strength. In Figure 3.29 is reported the XRD pattern of the ZAC041c dried precursor, where only the peaks ascribable to the hydrotalcite-type (Ht) phase can be observed.

After calcination at 550°C (Figure 3.30), it is possible to see the presence of ZnO and a Cu and/or Zn/Al spinel phase, together with traces of a low crystalline CuO phase.

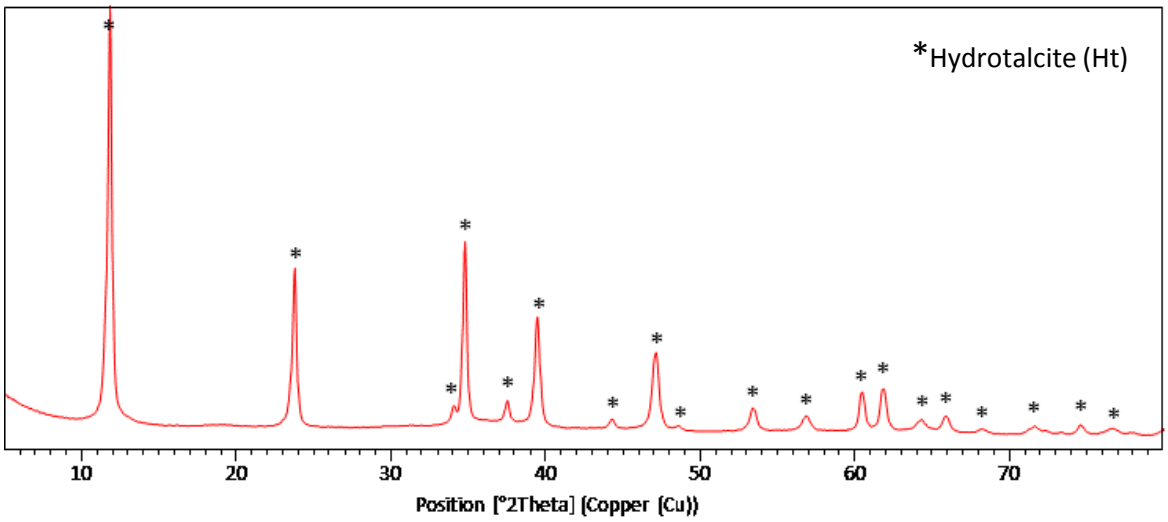

Figure 3.29 XRD pattern of the dried ZAC041c precursor.

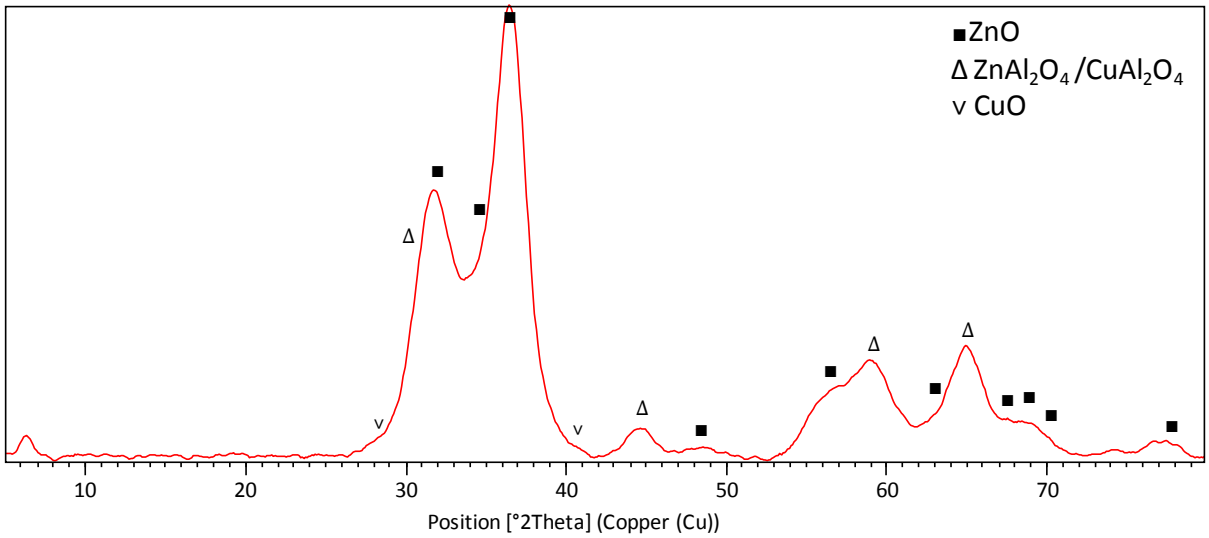

Figure 3.30 XRD pattern of calcined ZAC041c.

To evaluate the thermal stability of the material, the physical properties have been measured after calcination at 550 and 750°C. The increase in the calcination temperature gives rise to a general decrease of both surface area and cupper dispersion.

	550°C x 6h				750°C x 6h			
Sample	BET S.A. (m^2/g)	M.S.A. (m^2_{Cu}/g_{sample})	D (%)	d_{Cu} (nm)	BET S.A. (m^2/g)	M.S.A. (m^2_{Cu}/g_{sample})	D (%)	d_{Cu} (nm)
ZAC041c	73	1	4	24	50	1	3	33

Table 3.24 Physical properties of ZAC041c catalyst; effect of the calcination temperature

The redox properties of the calcined sample have been studied by TPR-O-R experiments. In the first TPR experiment (Figure 3.25, curve green), it is possible to observe two peaks, related to the consumption of H_2; the first centered at 350°C may be attributed to the reduction of

CuO particle formed in the calcination; the former centered at about 700°C may be ascribed to the reduction of the spinel phase. The high temperature of reduction of CuO suggest that the particle are in strongly interacting with the oxide matrix. After a re-oxidation step (TPO) at 750°C a second TPR experiment (blue curve) has been performed, detecting a peak centered at 200°C with two shoulders, at 110°C and 335°C. In this case, the temperature is typical of the reduction of free CuO particles, the shape of the curve suggesting a wide range of particle size. The first shoulder at 110°C may be attributed to the partial reduction of Cu^{2+} to Cu^{+}. The decrease of the reduction temperature is due to the weakening of the interaction between the cupper and the oxide matrix. During the second reduction it was not possible to observe any pick attributable to the spinel phase reduction.

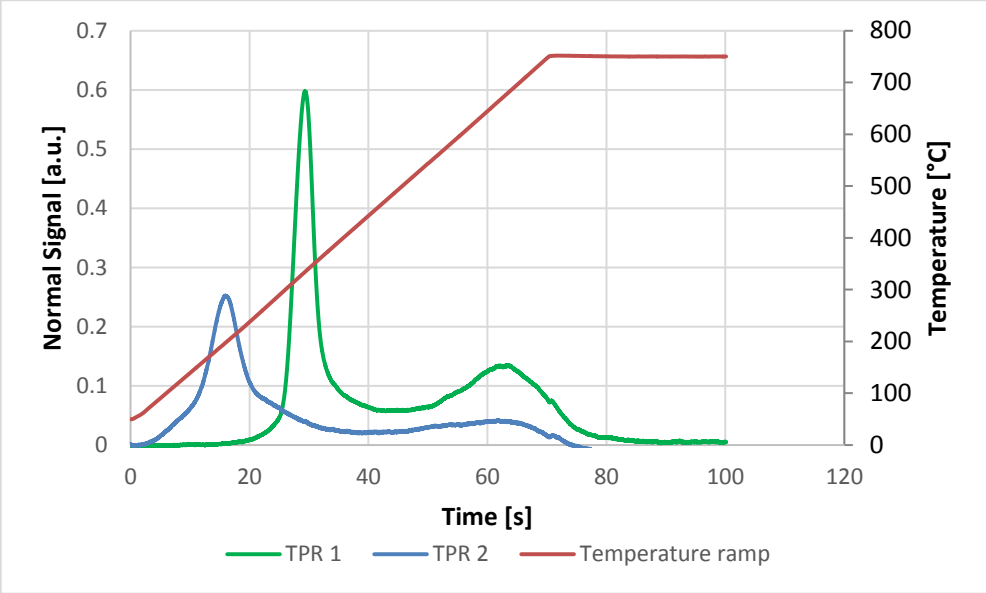

Figure 3.31 TPR profiles of ZAC041c catalyst obtained during the R-O-R cycle

Peak	1° peak [a.u.]	2°peak [a.u.]
H_2 consumption/CuO	0.67	0.41

Table 3.25 H_2 consumption measured during TPR analysis.

Tests were performed, as reported in Figure 3.32 and Figure 3.33, starting with le lowest temperature and contact time, and then increasing firstly the contact time and finally the temperature, in order to avoid changes in the catalyst activity due to the thermal aging.

First, the catalyst was tests under screening conditions, at 430°C, 20 bar, S/DG of 0.55 v/v and a contact time of 3s, to reach the equilibrium value, with a CO_2 selectivity of 100%.

Tests performed at 350°C and S/DG of 0.55v/v show that, by increasing the contact time increases the CO conversion. The increase of the temperature to 400°C gives rise to a higher

activity, reaching the equilibrium value in the test with a contact time value of 1 s. A similar effect can be observed also at 450°C, leading to obtain the CO equilibrium conversion value for all contact time value.

A similar result was observed in tests with S/DG of 0.65 v/v (Figure 3.33), in which the increase of the steam content improves the catalyst activity, giving rise to higher CO conversion.

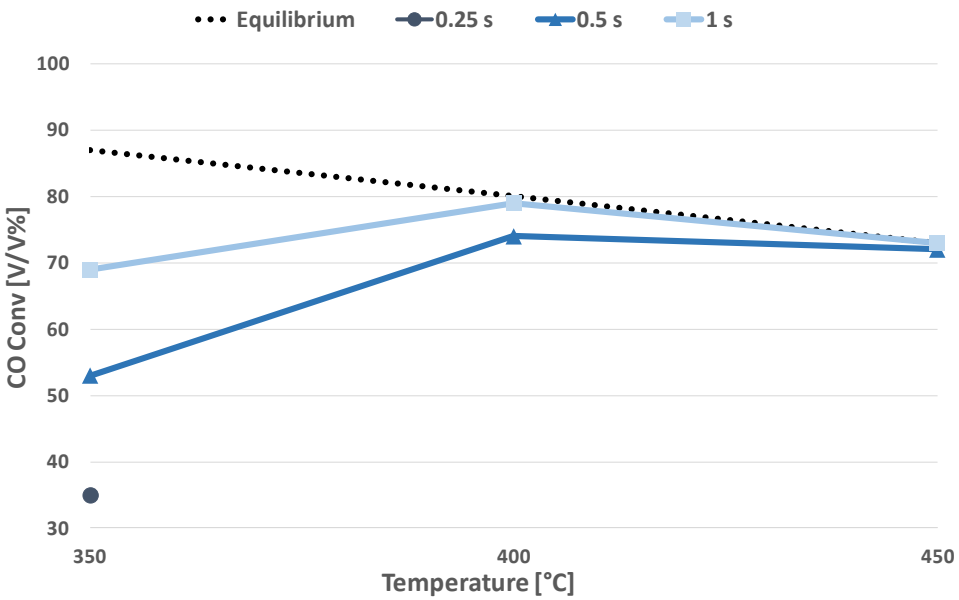

Figure 3.32 CO conversion for the ZAC041c catalyst as function of the temperature for different contact times, compared with the equilibrium values (S/DG= 0.55v/v).

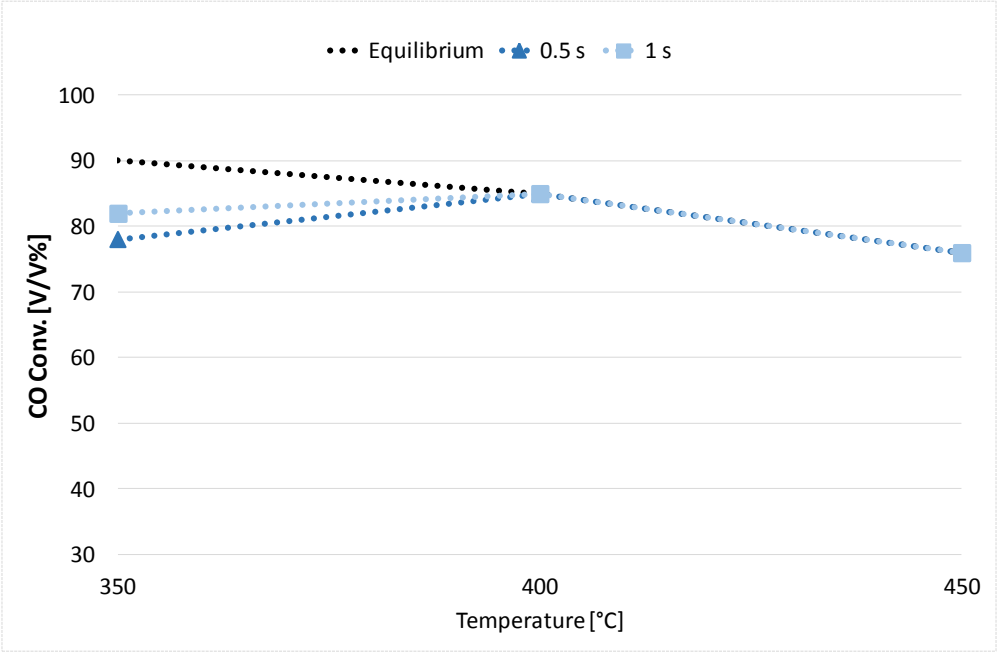

Figure 3.33 CO conversion for the ZAC041c catalyst as function of the temperature for different contact times, compared with the equilibrium values (S/DG= 0.65v/v).

Although the Cu based catalysts are known to be active in methanol synthesis, the ZAC041c show a very low tendency to form alcohols (Table 3.26). The methanol concentration measured in the condensed unconverted water rise with the contact time and decrease with the temperature. It is known that the thermal decomposition of the alcohols is favored by increasing of the temperature. By increasing of the contact time, the higher methanol production obtained may be correlated to a reaction mechanism involving a common intermediate with the WGS reaction.

		Test	MeOH [mg/L]	Test	MeOH [mg/L]
T [°C]	τ [s]	S/DG 0,55		S/DG 0,65	
350	0,25	1	14		
350	0,5	2	69	8	71
350	1	3	93	9	111
400	0,5	4	50	10	38
400	1	5	57	11	67
450	0,5	6	19	12	17
450	1	7	26	13	23

Table 3.26 Methanol concentrations detected in the condensed water for the tests at S/DG 0,55 and 0,65 v/v with the ZAC041c catalyst. Tests performed at the same temperature and contact time are reported in the same row.

After the activity cycles, the deactivation was verified by repeating of the initial tests, observing in both cases, a decrease in the CO conversion (Table 3.27).

S/DG	0.55	0.65
Decrease in CO% conversion	43	53

Table 3.27 Deactivation observed for ZAC041c catalyst after tests at different S/DG values.

The higher deactivation showed after tests performed with the highest S/DG ratio may be correlated to the harder hydrothermal treatment of the catalyst surface, due to the higher steam content.

On the spent catalyst, the formation of Cu particles well stabilized in the catalyst oxide matrix are observed, with the particle size increasing from 24 to 29nm.

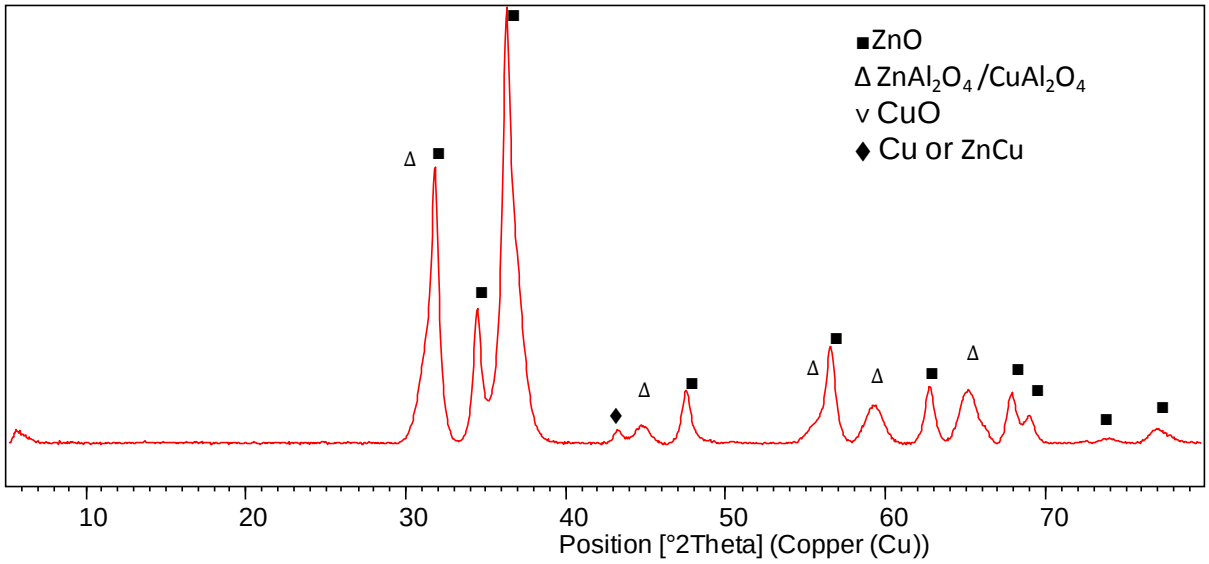

Figure 3.34 XRD pattern of spent ZAC041c catalyst.

3.2.2 Effect of doping elements on the activity and stability

The catalytic performances obtained for the ZAC041c catalysts point out very interesting prospective for the application of Cu-based in HTS reaction. However, the high deactivation observed is a key drawback that has to be improved. As discussed in the first part of this thesis for the MTS catalysts and as suggested by literature [22,23], the reference catalyst was doped with In, La and Ga, respectively.

3.2.3 Addition of La; ZAC041cLa50 characterization

The amount of La was defined in order to obtain an Al/La molar ratio of 50. The La-doped dried precursor shows a lower crystallinity compared to the reference one (Figure 3.35). Furthermore, it is possible to see the presence of small amount of aurichalcite phase. After calcination no La-containing phase was observed and the diffraction pattern is the same of the reference sample (Figure 3.36).

The addition of La give improve the physical properties, with a higher surface area and cupper dispersion (Table 3.28) also by increasing the calcination temperature.

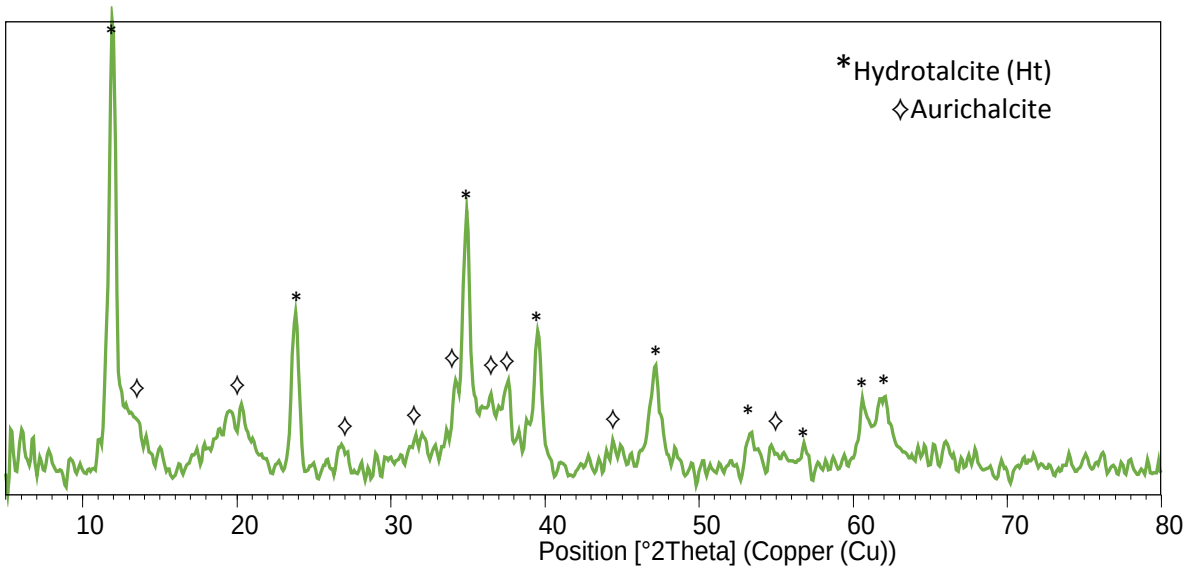

Figure 3.35 XRD pattern of the ZAC041cLa50 dried precursor.

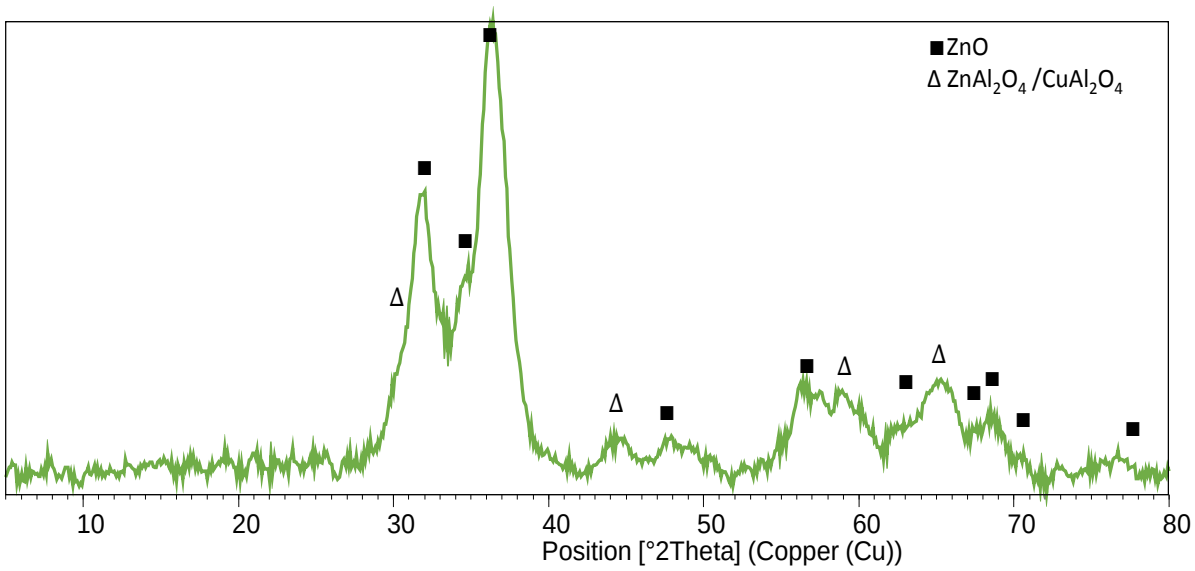

Figure 3.36 XRD pattern of the ZAC041cLa50 calcined catalyst.

	550°C x 6h				750°C x 6h			
Sample	BET S.A. (m^2/g)	M.S.A. (m^2_{Cu}/g_{sample})	D (%)	d_{Cu} (nm)	BET S.A. (m^2/g)	M.S.A. (m^2_{Cu}/g_{sample})	D (%)	d_{Cu} (nm)
ZAC041c	73	1	4	24	50	1	3	33
ZAC041c La50	87	4	13	8	46	3	12	8

Table 3.28 Effect of the La doping on the physical properties of the catalyst.

The introduction of La strongly affects the redox properties of the catalyst; the reduction profile of La-doped sample shows a higher reducibility respect to the undoped catalyst. (H_2 consumption/CuO = 1,72 higher than that of the reference one). The increase of the amount

of Cu that may be reduced by adding of La is in line with the reduction of particle size and increase of Cu dispersion. These effects leads to a strong interaction between Cu-containing particles and oxide matrix, resulting in an increase of the temperature of reduction, in this case shifted at 363°C.

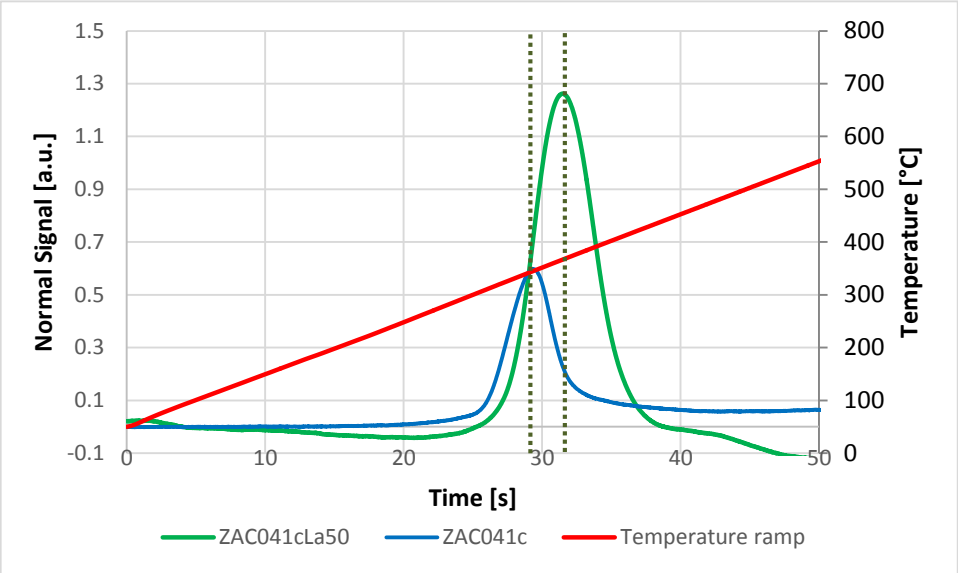

Figure 3.37 TPR profiles of calcined ZAC041c and ZAC041cLa50.

3.2.4 Addition of In; ZAC041cIn50 characterization

As in case of La, In was added to ZAC041c catalyst with a Al/In molar ratio of 50. In this case, the dried precursor show a crystalline hydrotalcite-type phase, with a small amount of aurichalcite (Figure 3.38). After calcination ZnO and spinel phase are formed (Figure 3.39).

The addition of In gives rise to an important improvement of the physical properties of the catalyst (Table 3.29), with an elevate surface area value and a lower reduction temperature. The smaller Cu-containing particles give rise to a higher reducibility (Figure 3.40); TPR analysis shows possible to see a single peak centered at 304°C, lower than that of the reference catalyst. The value of observed H_2 consumption/CuO is equal to 1.39.

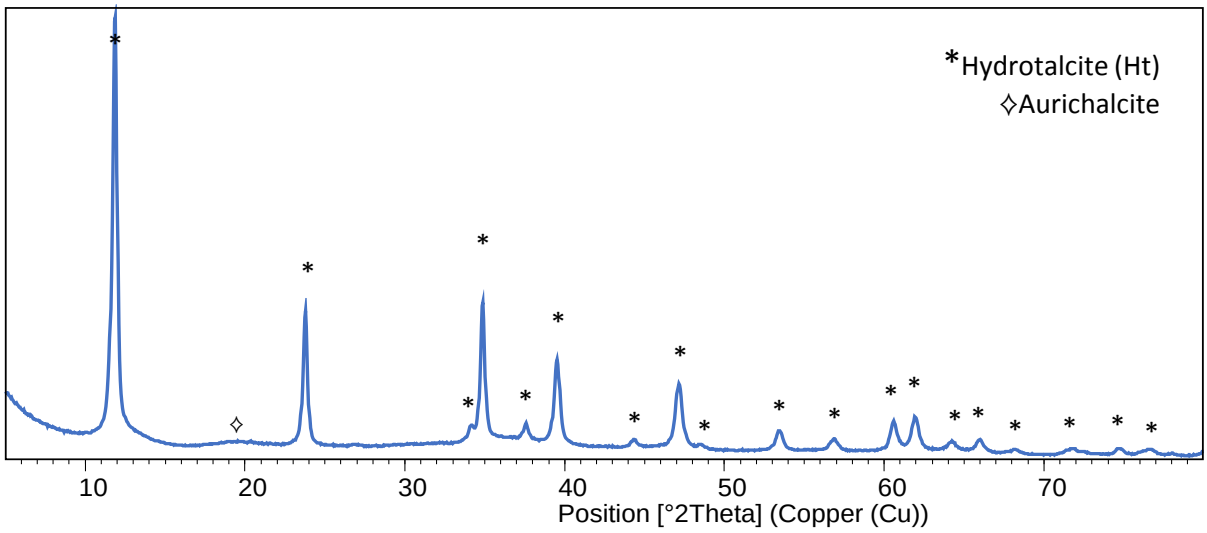

Figure 3.38 XRD pattern of the ZAC041cIn50 dried precursor.

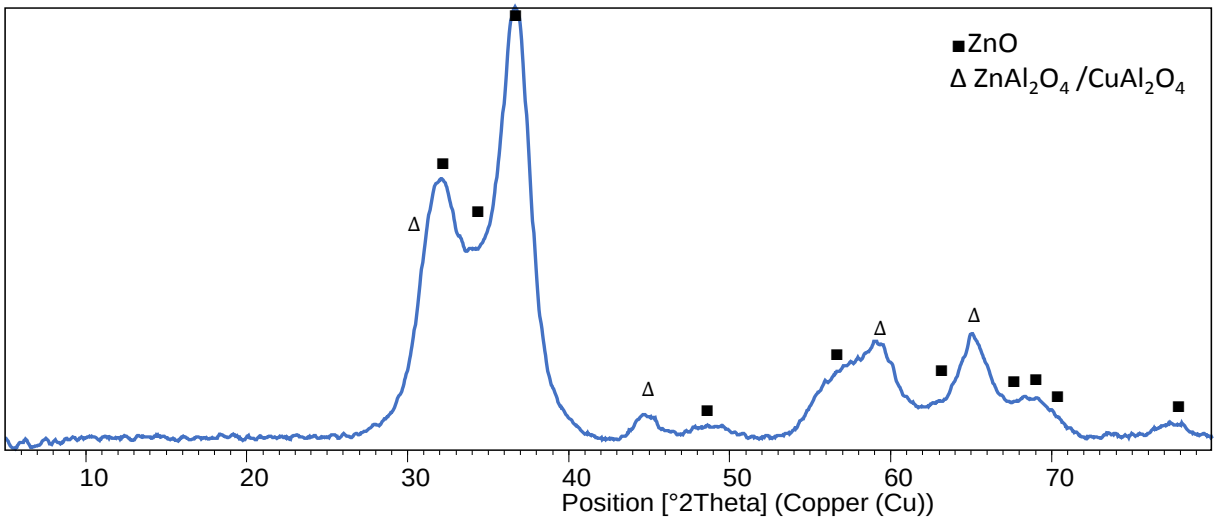

Figure 3.39 XRD pattern of the ZAC041cIn50 calcined catalyst.

	550°C x 6h				750°C x 6h			
Sample	BET S.A. (m^2/g)	M.S.A. (m^2_{Cu}/g_{sample})	D (%)	d_{Cu} (nm)	BET S.A. (m^2/g)	M.S.A. (m^2_{Cu}/g_{sample})	D (%)	d_{Cu} (nm)
ZAC041c	73	1	4	24	50	1	3	33
ZAC041c In50	103	6	22	5	13	8	32	3

Table 3.29 Effect of the In doping on the physical properties of the catalyst.

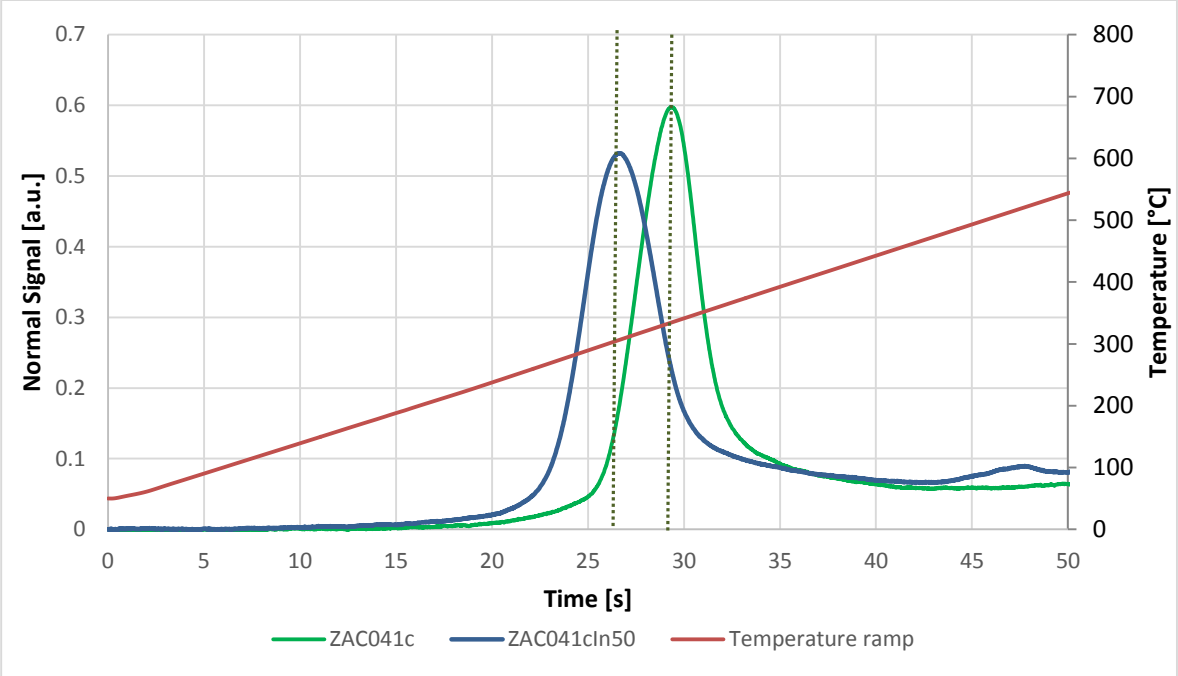

Figure 3.40 TPR profiles of fresh ZAC041c and ZAC041cIn50.

3.2.5 Addition of Ga; ZAC041cGa50 characterization

Ga also was added to ZAC041c catalyst with an Al/Ga molar ratio of 50.

In the XRD pattern of the precursor only the hydrotalcite-type phase is detected (Figure 3.41), while after calcination ZnO and spinel phase are formed (Figure 3.42).

Also in this case an improvement in the physical properties was observed (Table 3.30). Cu particles are characterized by lower size and higher reducibility. TPR analysis shows a reduction peak centered at 320°C, lower than that observed for the undoped catalyst. The addition of Ga give rise to an increase in the reducibility of the material respect to the reference ZAC041c catalyst, with a H_2 consumption/CuO ratio of 01.24.

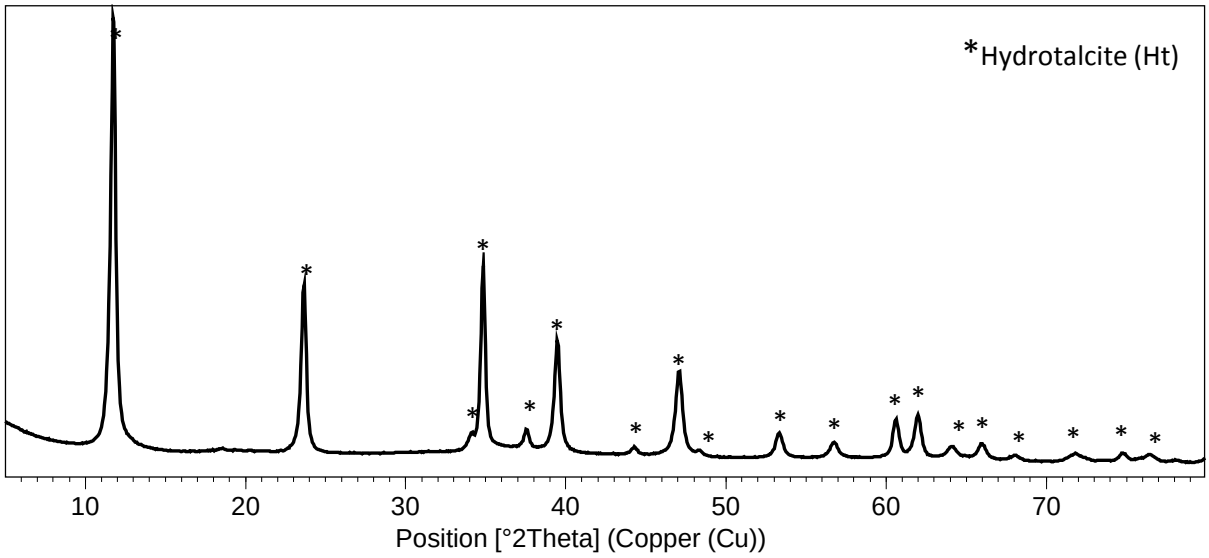

Figure 3.41 XRD pattern of the ZAC041cGa50 dried precursor.

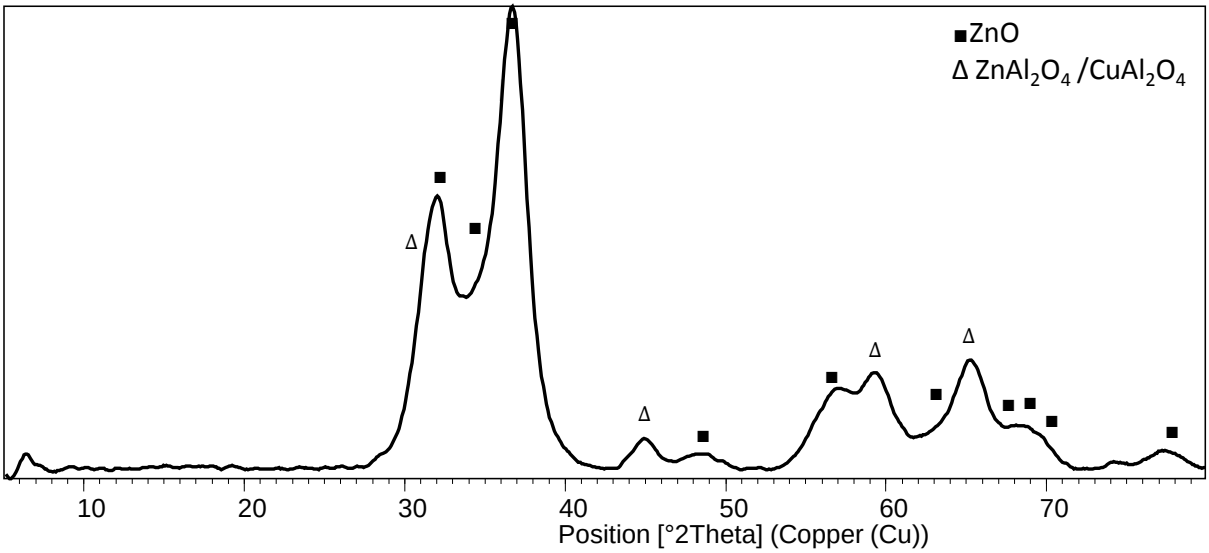

Figure 3.42 XRD pattern of the calcined ZAC041cGa50 catalyst.

	550°C x 6h				750°C x 6h			
Sample	BET S.A. (m^2/g)	M.S.A. (m^2_{Cu}/g_{sample})	D (%)	d_{Cu} (nm)	BET S.A. (m^2/g)	M.S.A. (m^2_{Cu}/g_{sample})	D (%)	d_{Cu} (nm)
ZAC041c	73	1	4	24	50	1	3	33
ZAC041c Ga50	97	5	20	5	33	5	18	6

Table 3.30 Effect of the Ga doping on the physical properties of the catalyst.

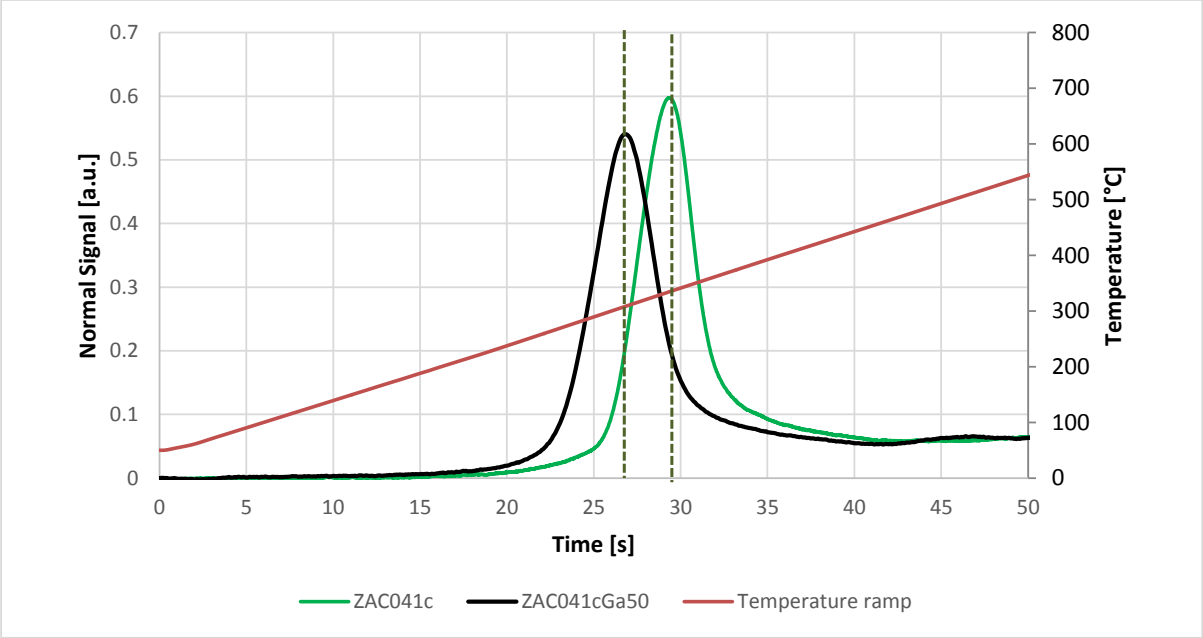

Figure 3.43 TPR profiles of calcined ZAC041c and ZAC041cGa50.

3.2.6 Effect of doping elements on the catalytic activity

All the doped catalysts were tested in HTS reaction, to evaluate the variations of the catalytic performances. The addition of doping elements gives rise to an improvement of the physical properties of the catalysts, the results of activity tests show significant differences (Figure 3.44).

The La doped one shows a higher activity respect to the reference one, reaching the equilibrium conditions already at 350°C with a contact time of 1s. The In incorporation leads to the unexpected results, with a lower CO conversion observed, also increasing the temperature.

The best results are obtained with Ga containing sample. In fact, equilibrium values are reached already at 350°C. Furthermore, this formulation leads to very stable activity, showing the lower deactivation rate (Table 3.31).

All the doped catalysts show a higher tendency to form methanol, in particular the Ga-containing sample, probably correlated to the high activity (Table 3.32).

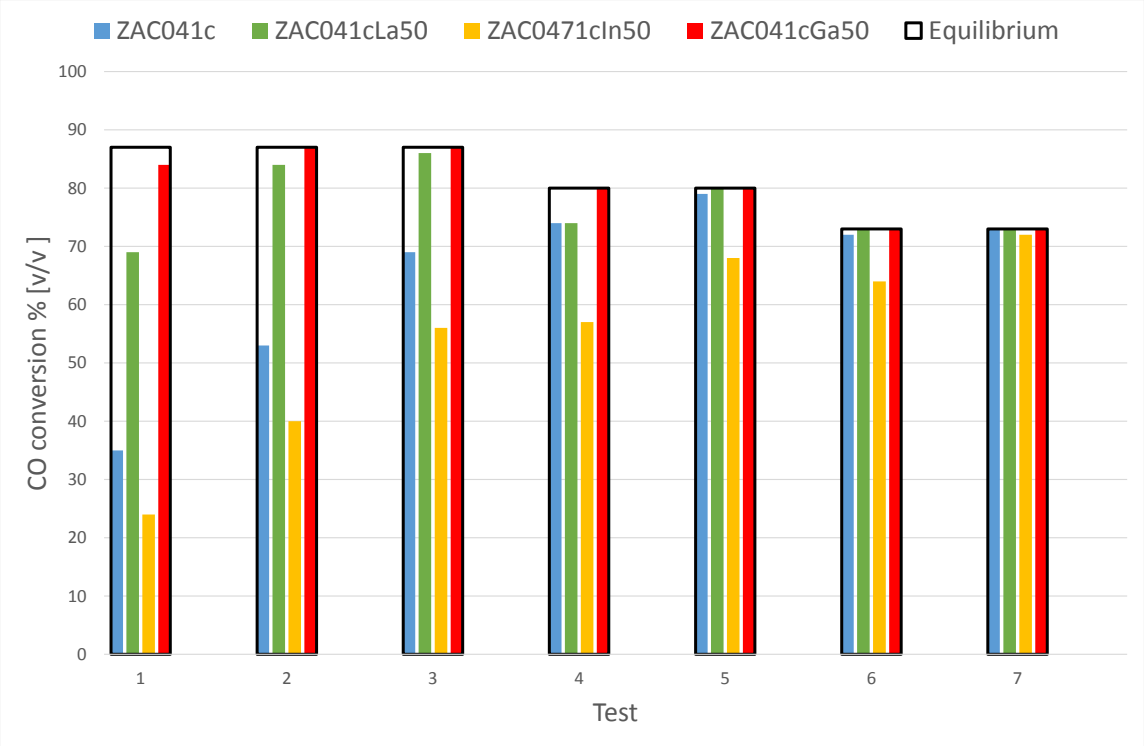

Figure 3.44 CO conversion obtained in the different tests performed with S/DG = 0,55 v/v: effect of the doping elements.

Catalyst	Deactivation (Decrease in CO% conversion)
ZAC041c	43
ZAC041gLa50	23
ZAC041cIn50	37
ZAC041cGa50	7

Table 3.31 Deactivation observed for the undoped and doped ZAC041c catalysts.

	T (°C)	350	350	350	400	400	450	450
Catalyst	**Contact time (s)**	**0.25**	**0.50**	**1.00**	**0.50**	**1.00**	**0.50**	**1.00**
ZAC041c	MeOH (ppm/h)	4	21	18	13	11	8	6
ZAC041cLa50	MeOH (ppm/h)	27	54	53	22	29	14	8
ZAC041cGa50	MeOH (ppm/h)	166	159	96	92	58	42	20
ZAC041cIn50	MeOH (ppm/h)	16	54	76	72	45	101	36

Table 3.32 By-products obtained as a function of the reaction conditions for undoped and doped catalysts.

The lower activity observed in the In doped catalyst may be correlated to different aspects. The higher cupper dispersion, observed respect to that of the ZAC041c catalyst, measured by N_2O chemisorption, could be overestimate by the interaction between N_2O and the In-containing species. Matsumura e Ishibe [24] hypothesized that part of the N_2O may react with In forming In_2O_3.

$In_2O_3 + 3\ H_2 \longrightarrow 2In + 3\ H_2O$

$2\ In + 3\ N_2O \longrightarrow In_2O_3 + 3\ N_2$

To verify this assumption, a Zinc-Aluminum mixed oxide sample a composition comparable to that of the ZAC041In50 catalyst, was prepared. After calcination at 550 °C for 6 h the material shows the presence of Zn and Zn/Al oxides as in the other Zn/Al based catalysts, such as highlighted in the XRD spectrum diffraction (Figure 3.45).

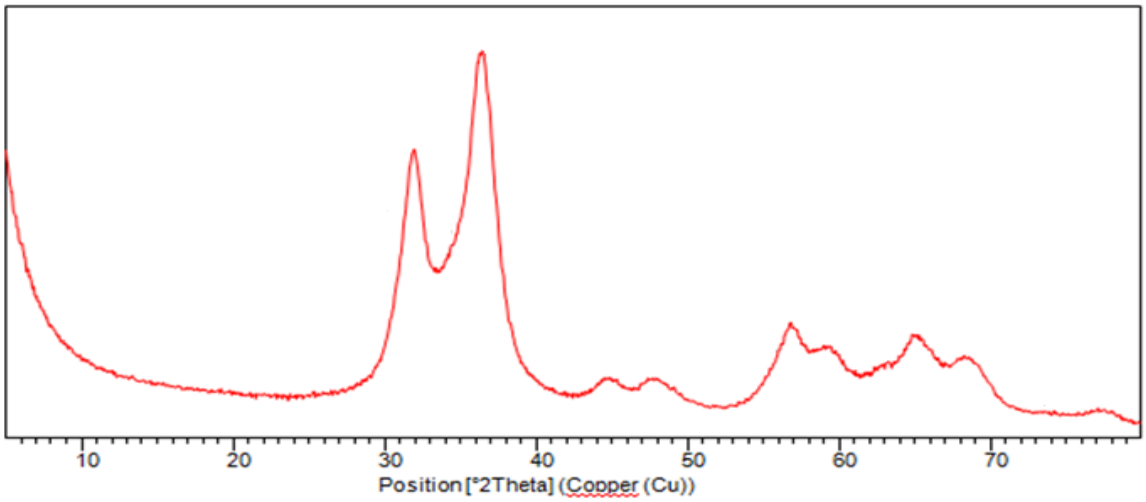

Figure 3.45 XRD pattern of the calcined ZA catalyst.

After calcination, an $In(NO_3)_3$ aqueous solution was impregnated on the surface of the Zn/Al sample by incipient wetness impregnation (IWI) to obtain 2wt% of In. Then the sample was dried and calcined at 550 °C for 2 h.

Chemisorptions analyses, performed on the impregnated sample (Figure 3.46A), confirm that In_2O_3 can be reduced during the reduction step and then interacts with N_2O strongly affecting the Cu dispersion determination. This result confirms the high hydrogen consumption observed during TPR analysis, attributable to the reduction of In oxides, because the ZA sample does not undergoes to reduction-oxidation reactions during both in TPR (not shown) and N_2O-chemisorption analysis (Figure 3.46B).

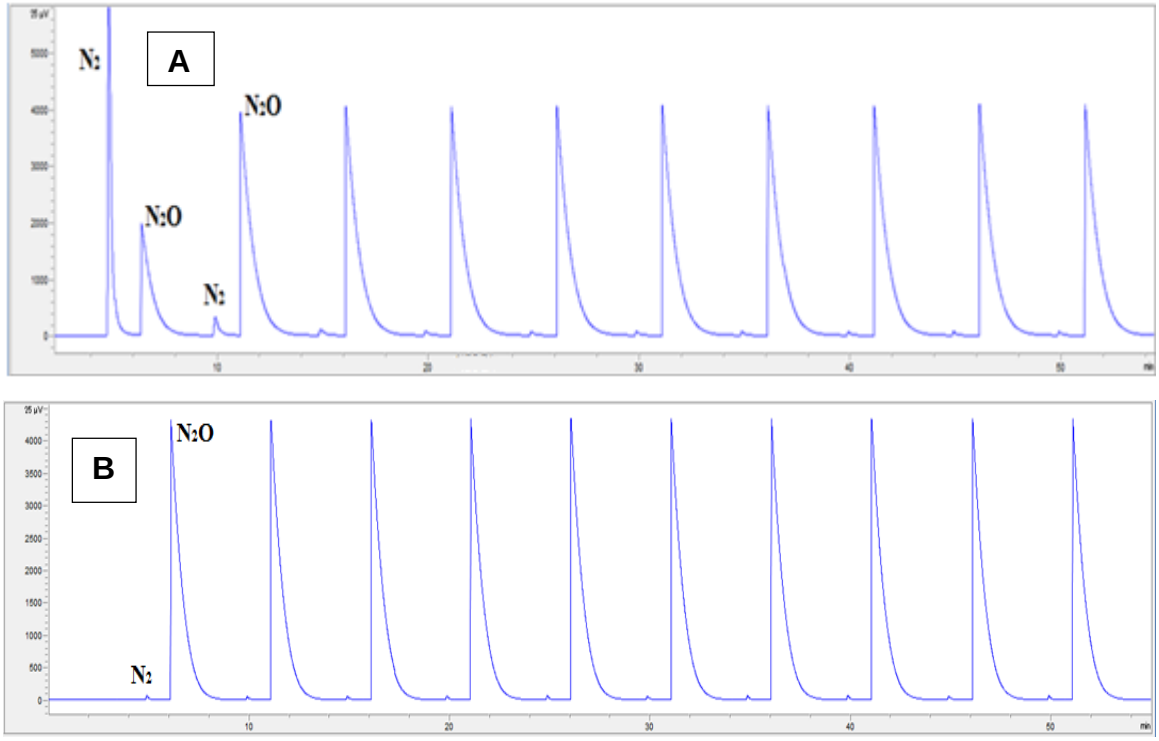

Figure 3.46 N_2O-chemisorption chromatogram peaks of 2%In/ZA catalyst (A) compared with the undoped ZA sample (B).

On the contrary, La and Ga 2wt% impregnated samples do not show any redox reactivity during the chemisorption analyses (Figure 3.47), confirming the reliability of the Cu-dispersion value obtained, that well justify the improvement in the catalytic activity.

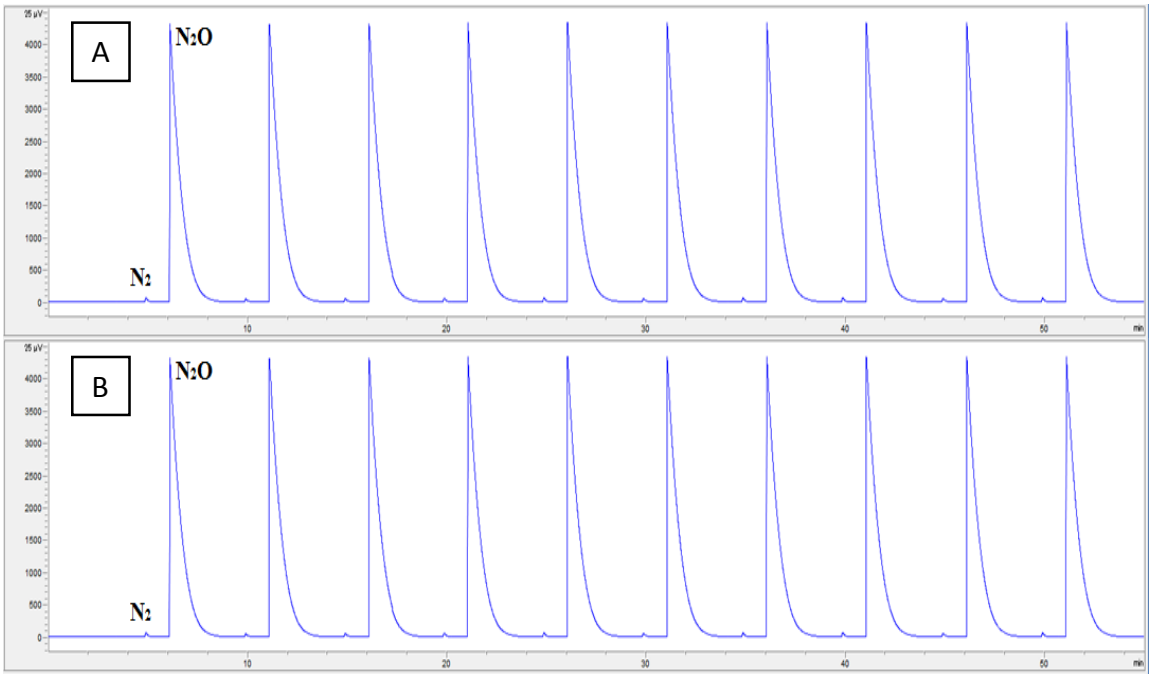

Figure 3.47 N_2O-chemisorption chromatogram peacks of 2%Ga/ZA catalyst (A) and of 2%La/ZA catalyst (B).

The low activity of the ZAC041cIn50 catalyst may be also due to the low melting temperature. In fact, In-oxides may be reduced during activation, forming In^0, that melts at 156,6 °C [25,26] and may form alloys with the Cu^0 present on the surface, reducing its activity.

XRD patterns of spent catalysts (Figure 3.48) show the following results: i) the presence of ZnO, spinel and Cu phases for ZAC041c catalyst, with an increase in the crystallinity; ii) the presence of the same crystalline phase also for ZAC041cIn50 with an increase of the intensity of the peaks related to the spinel phase; iii) the absence of peaks attributable to Cu-containing phase and a significant increase of the spinel phase peaks in case of Ga containing sample.

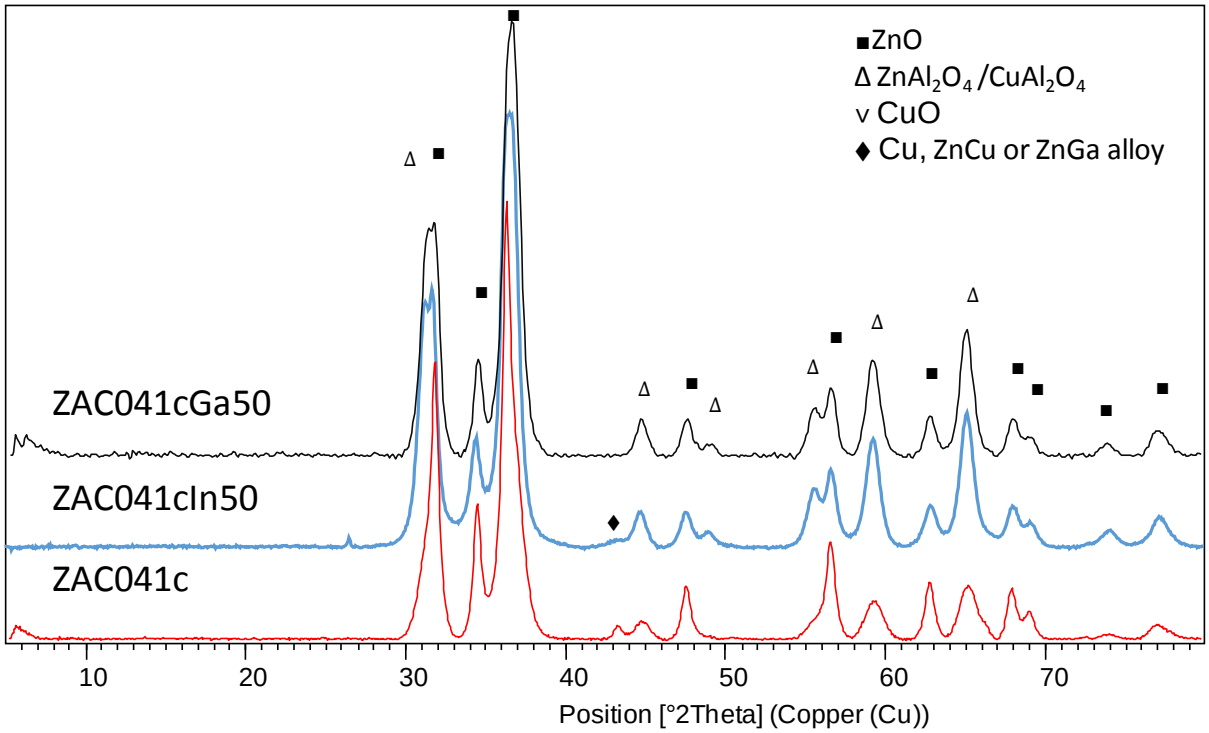

Figure 3.48 XRD patterns of ZAC041c, ZACo41cIn50 and ZAC041cGa50 spent catalysts.

Differences observed in terms of reactivity and crystalline phases evidenced by XRD analyses are the consequence and the cause, respectively, of the different redox behaviors observed in the TPR experiments carried out on spent catalysts. (Figure 3.49). To evaluate the effect of calcination temperature on the evolution of the phases, the same tests were also performed on the samples calcined at 750°C (Figure 3.50).

After reaction, the reducibility of the samples is evidenced by a main peak accompanied by two shoulders related to the H_2 consumption.

Assuming that are the CuOx species, obtained by passivation of reduced species formed during reaction, that mainly contribute to the H_2 consumption, comparing the three catalysts

it is possible to do the following observations: i) the spent catalyst containing In consumes about the same amount of H_2 during the reduction step in comparison to the reference catalyst, but the reduction happens at lower temperature probably because the particle are smaller or less interacting with the oxide matrix; ii) the addition of Ga in the catalyst formulation results in a decrease of the H_2 consumption measured for the catalyst after reaction, accompanied to a slight decrease of the reduction temperature if compared to the reduction profile of calcined sample. Considering the former case, the position of the peak suggests the formation of more stable CuO particle, strongly interacting with the oxide matrix. The last assumption may be confirmed by comparing the TPR profiles of samples calcined at 750°C (Figure 3.51). In fact, the calcination temperature strongly affects the average particle size distribution resulting in a different reducibility. Catalysts containing In and Ga are characterized by an higher H_2 consumption respect to the undoped catalyst. The increase in H_2 consumption is accompanied by a significant decrease in the reduction temperature, that is more evident for the catalyst containing Ga. The above reported results agree with the crystalline phases evolution observed by XRD analyses (Figure 3.51). The reference sample shows the formation of CuO, ZnO and spinel phases, while in the case of Ga and In containing catalysts CuOx phases are not detectable, with an important increase of the spinel phase.
Comparing results obtained for TPR analyses carried out on samples calcined at 750°C with those performed on the same samples calcined at 550°C, it is possible to observe a shift of the curves to lower temperature for the former catalysts, with and a higher H_2 consumption for doped samples. This effect may be explained supposing that the increase in the calcination temperature give rise to: i) an increase of free and less interacting copper species on the surface, that may justify the decrease of reduction temperature; ii) the free species formed quickly undergo sintering forming bigger particles in case of undoped catalyst. The presence of a dopant stabilize these particles and justify that in case of doped samples, the increasing of the calcination temperature increases the amount of consumed H_2.

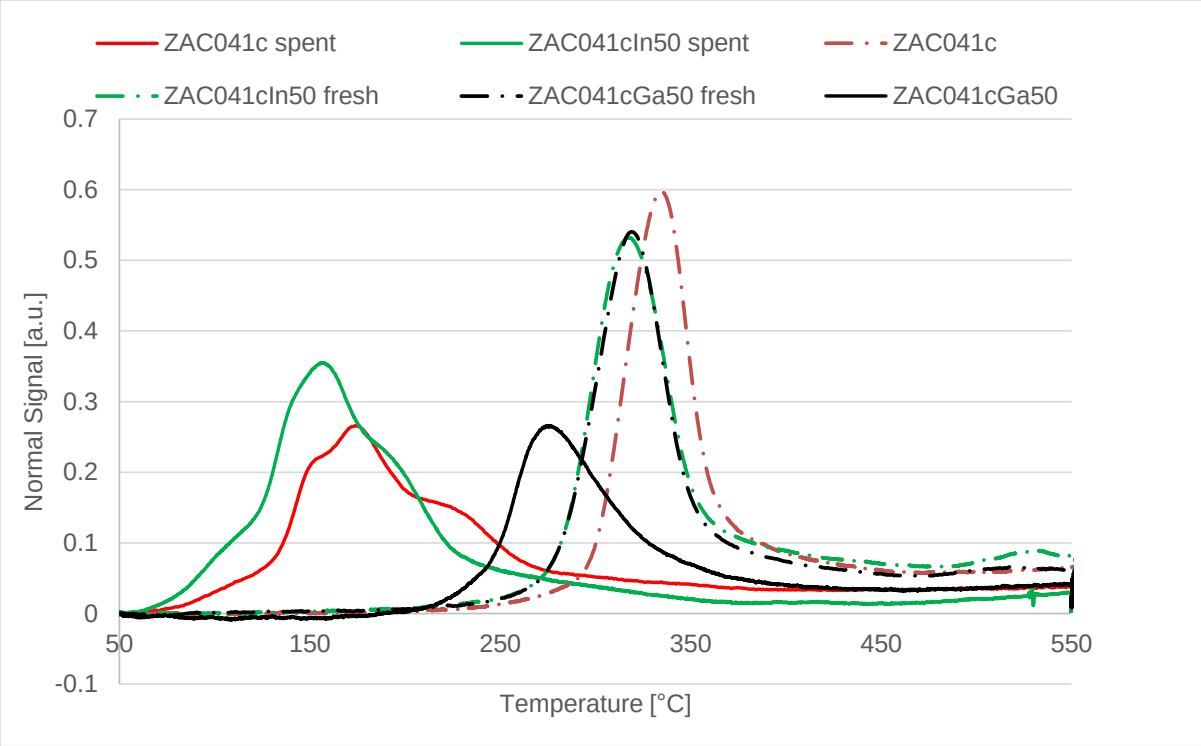

Figure 3.49 TPR analysis of ZAC041c, ZAC041cIn50 and ZAC041cGa50 fresh and spent catalysts.

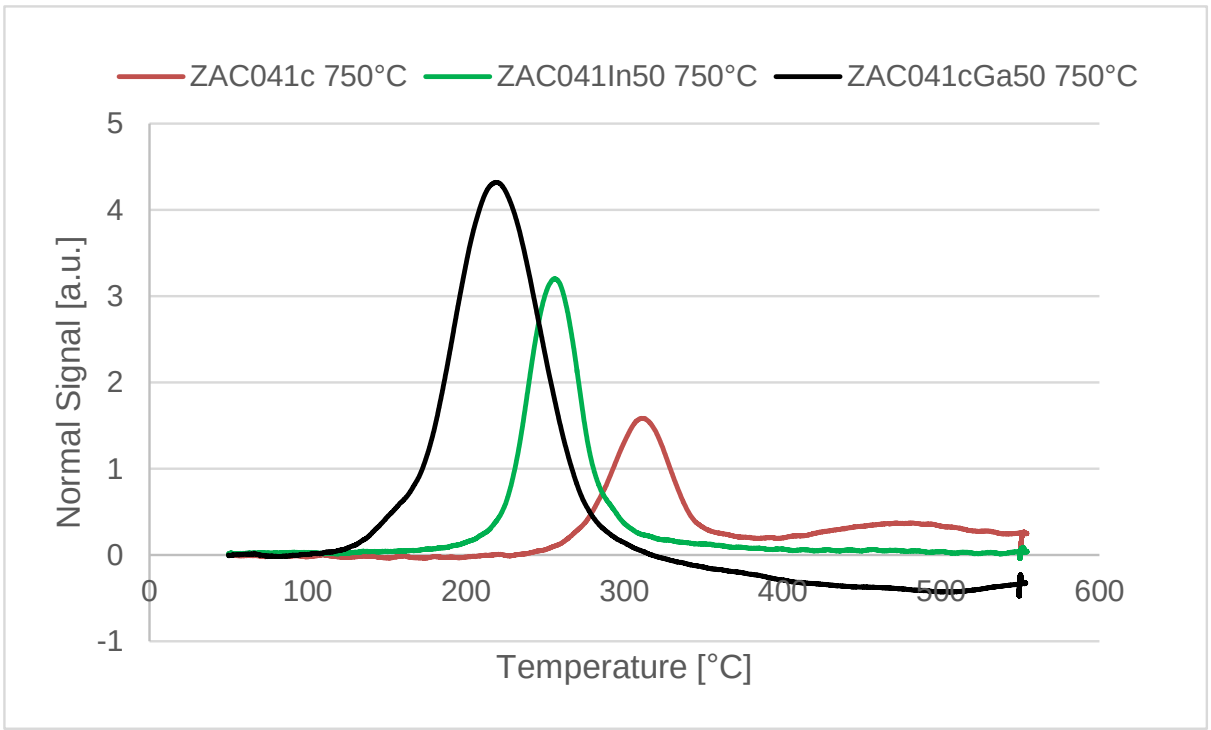

Figure 3.50 TPR analysis of ZAC041c, ZAC041In50 and ZAC041Ga50 catalysts calcined at 750°C.

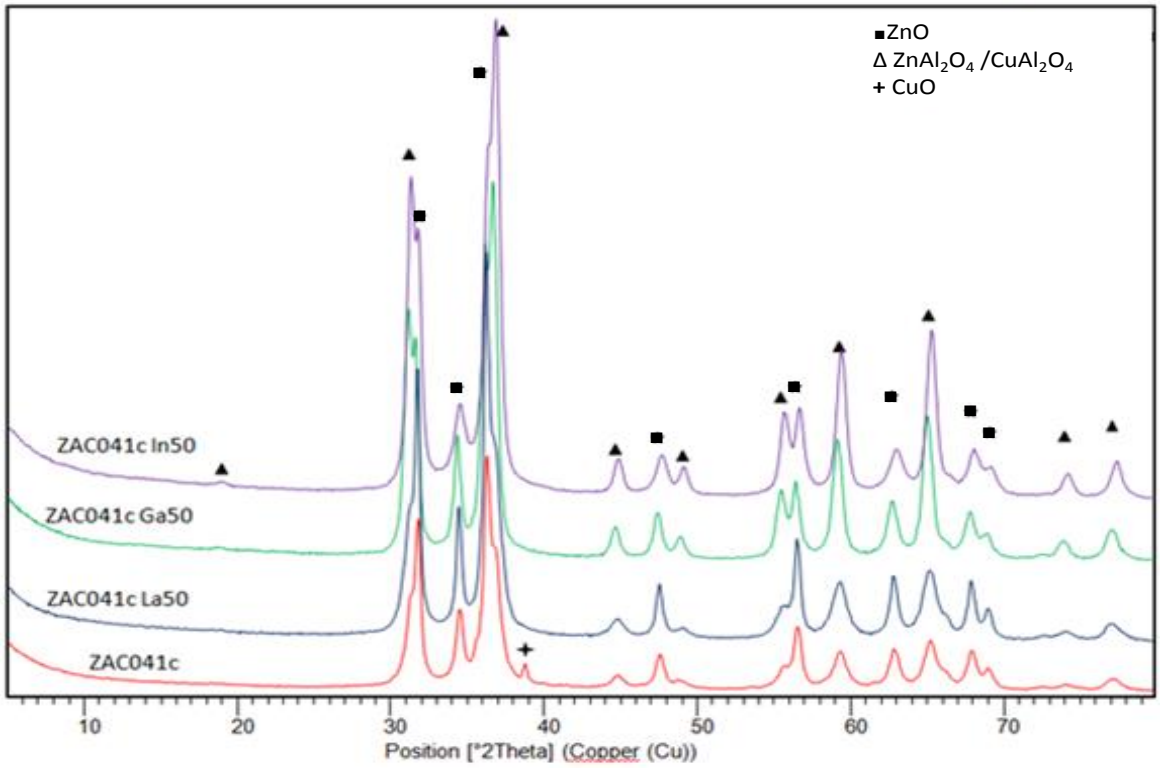

Figure 3.51 XRD patterns of spent ZAC041c, ZAC041cLa50, ZAC041Ga50, and ZAC041cIn50 calcined at 750°C.

The above results partially agree with the catalytic behaviors. In fact, if the effect of Ga addition matches with the catalytic results, in case of In there is not a correlation between physical-chemical properties and catalytic activity.

To shed light on the effect of the doping agent on the active phase, the calcined catalysts were characterized by FT-IR analysis using CO as probe molecule. Analysis were carried out at -196°C on pre-reduced samples (at 350°C with a H_2/N_2 5% v/v stream).

ZA catalyst was analyzed in the same conditions in order to discriminate the effect of interaction between CO and Zn/Al mixed oxide (Figure 3.52).

The spectra related to the reference system (formed by ZnO and $ZnAl_2O_4$), show a single band at 2155 cm^{-1}, correlated to physically adsorbed CO, weakly bounded to ZnO and the –H species present on the surface [27].

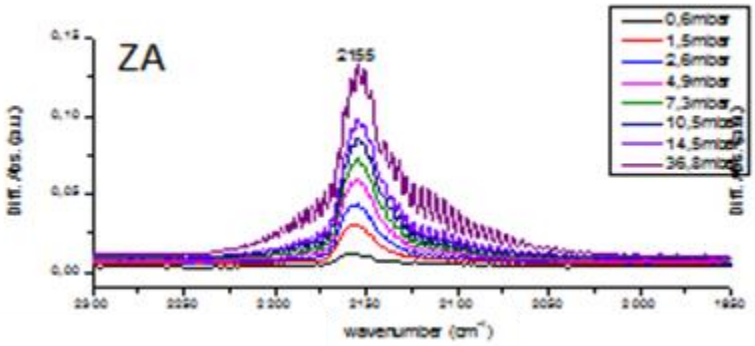

Figure 3.52 FT-IR spectra of the reduced ZA catalyst.

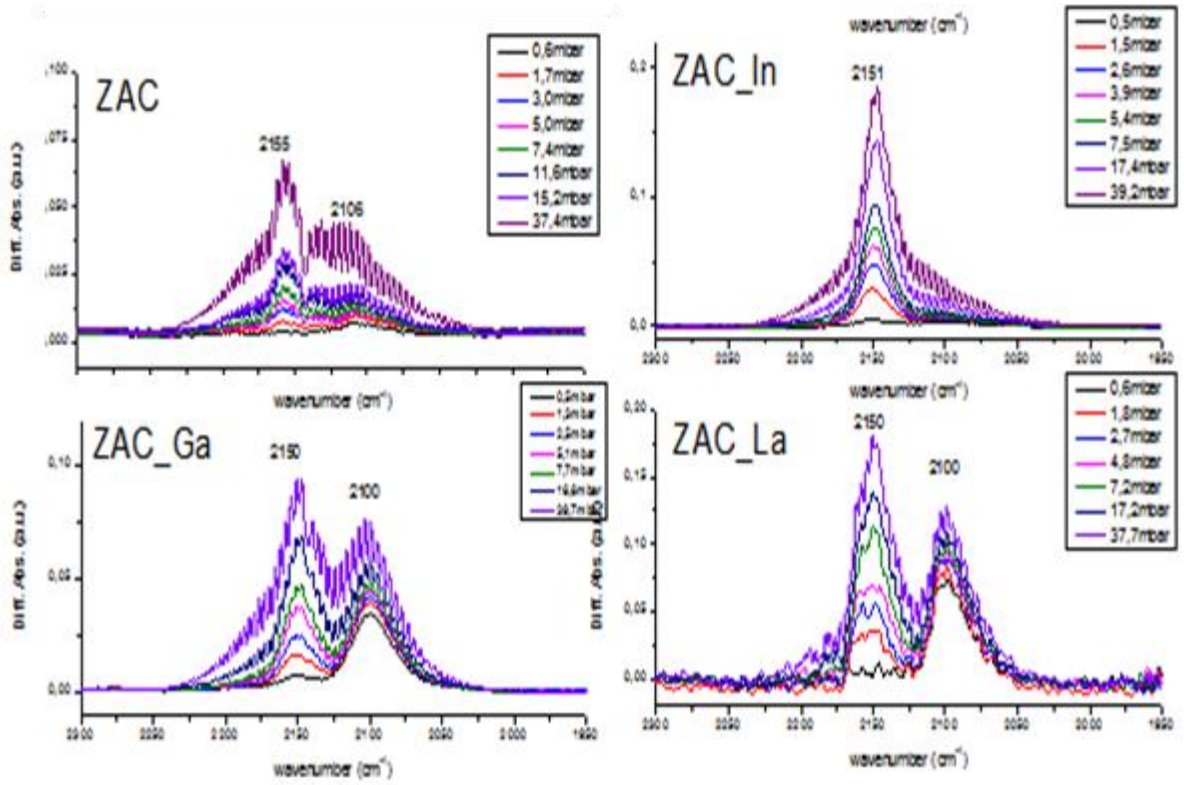

Figure 3.53 FT-IR spectra of reduces ZAC, ZAC041cIn50, ZAC041cGa50 and ZAC041cLa50 calcined catalysts.

The spectra of the ZAC041c catalyst (Figure 3.53) shows two bands; the first at 2155 cm^{-1} may be correlated to the physical-adsorption of CO on the oxide matrix, while the second broad band centered at 2106 cm^{-1} could be attributed to the CO interacting with Cu^0 formed during reduction the step [28].

On the contrary, the sample containing In shows only one band centered at 2151 cm^{-1} (Figure 3.53), as in the case of previous ZA sample, but shifted at lower wavenumber. This band may be attributed to a stronger interaction between CO and support and/or the interaction of CO with unreduced Cu^{2+} species. The absence of bands related to the presence of Cu^0 agrees with the low catalytic activity.

In both the La and Ga doped catalysts a shift of the band to lower wave number is observed. In particular it may be observed a first band at 2150cm^{-1} and a second one at 2100cm^{-1}, already present at 0.6 mbar of CO. This result may be attributed to small Cu^0 particles that strongly interact with adsorbed CO molecules [29].The presence of smaller metal particles was already evidenced by N_2O chemisorption analyses (Table 3.28 and Table 3.30).

A similar effect may be due to the exposition of different atomic planes of Cu. In fact, the adsorption of CO molecules on metallic surfaces characterized by different Miller indexes gives rise to bands characterized by a specific wavelength shift. In a study performed with a single crystal, the 2100 cm^{-1} frequency was measured for CO adsorbed on Cu(211) surface [30]. The higher activity of the La and Ga doped catalysts in HTS conditions may be correlated to both higher cupper dispersion and presence of a different atomic layers.

3.2.1 Effect of the Ga content on the catalytic properties

The results described in the previous section evidence that the addiction of small amount of Ga in the catalyst formulation leads to an important increase of catalytic activity both in terms of CO conversion and resistance to deactivation. For these reasons may be interesting a deeper investigation on the role of this element. A series of catalysts containing different amount of Ga have been prepared (Table 3.33) and compared to the undoped ZAC014c sample.

mol%	Cu	Zn	Al	Ga	Ga/Cu	Al/Ga	Ga/Al	Al/Cu
ZAC041c	4.16	45.8	50	0	0	0	0	12.02
ZAC041cGa200	4.17	45.9	49.7	0.25	0.06	200	0.005	11.92
ZAC041cGa50	4.19	45.8	49	0.98	0.24	50	0.02	11.69
ZAC041cGa28	4.17	45.8	48.3	1.72	0.41	28	0.04	11.58
ZAC041cGa20	4.22	45.8	47.6	2.38	0.56	20	0.05	11.28
ZAC041cGa14	4.25	45.75	46.67	3.33	0.78	14	0.07	10.99
ZAC041cGa11	4.17	45.8	45.83	4.17	1	11	0.09	10.99

Table 3.33 Composition of Ga containing catalysts: metal molar % content and metal ratio.

All the dried precursors are constituted mainly by a hydrotalcite-type phase, with small amount of aurichalcite detected in few samples, although the formation of this crystalline phase is to correlated to the amount of Ga (Figure 3.54).

The calcination at 550°C leads to the decomposition of the hydrotalcite-type phase to ZnO and spinel phases (Figure 3.55). The presence of CuO was detected only in the undoped ZAC catalyst.

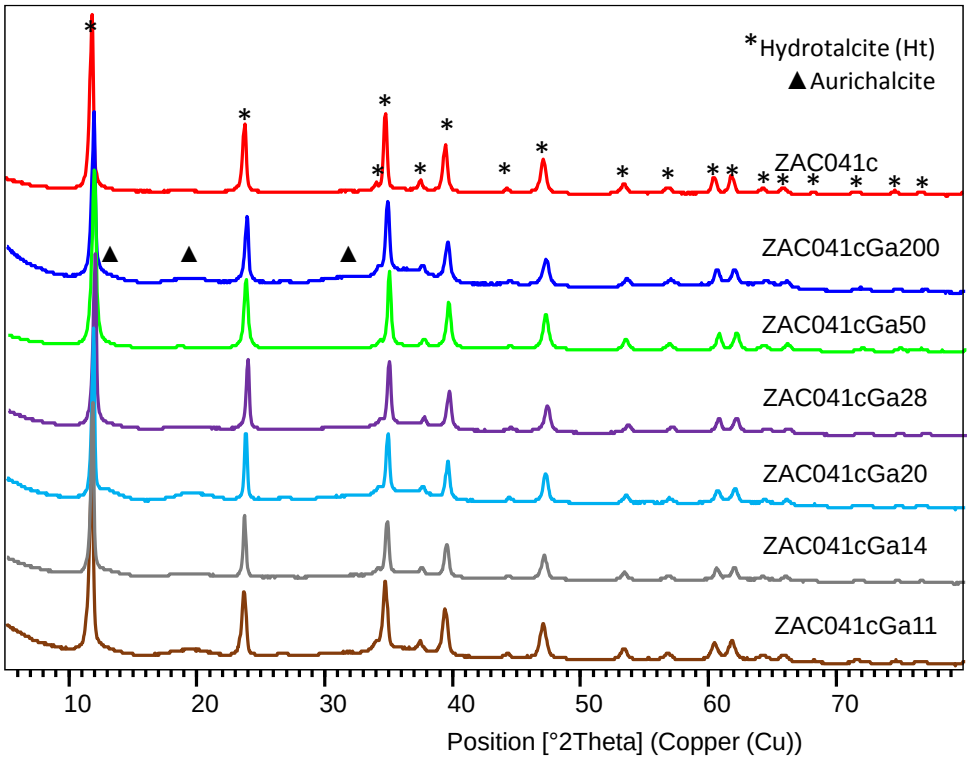

Figure 3.54 XRD patterns of ZAC041cGaX dried precursors.

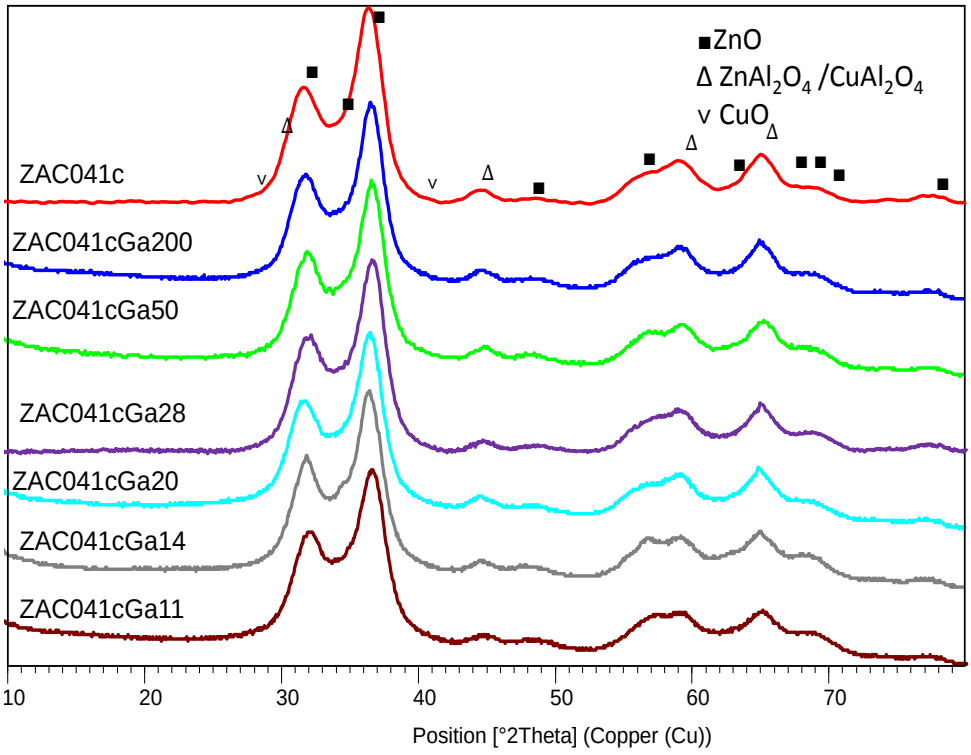

Figure 3.55 XRD patterns of calcined ZAC041cGaX catalysts.

The evaluation of the redox properties of calcined samples have been performed by TPR analyses (Figure 3.56). All the catalysts are characterized by a single reduction peak; temperature of reduction and amount of H_2 consumed during the process do not show a linear correlation with the Ga amount. (Figure 3.56).

The addiction of Ga leads to the formation of smaller CuO particles (Figure 3.57) compared to the reference sample. For high amount of Ga in the structure, a slight increase of particle size may be detected. The specific surface area of these samples an increase for small amount of Ga, reaching a maximum and then decrease by further increasing the Ga content and with anomalous behavior for the ZAAC041cGa20 catalyst (Figure 3.58).

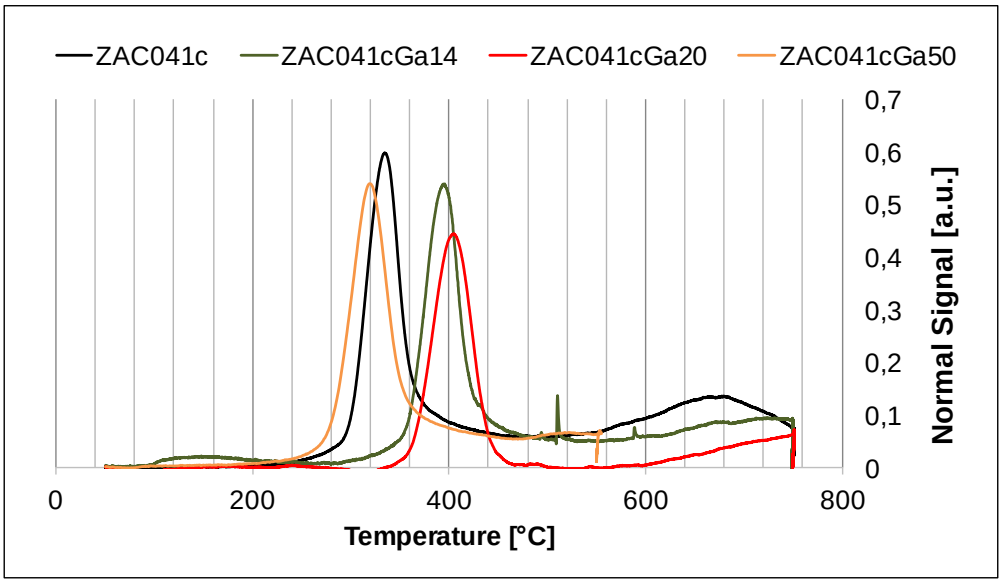

Figure 3.56 TPR analysis of calcined ZAC041c, ZAC041cGa11, ZAC041cGA20, ZAC041cGa50 catalysts.

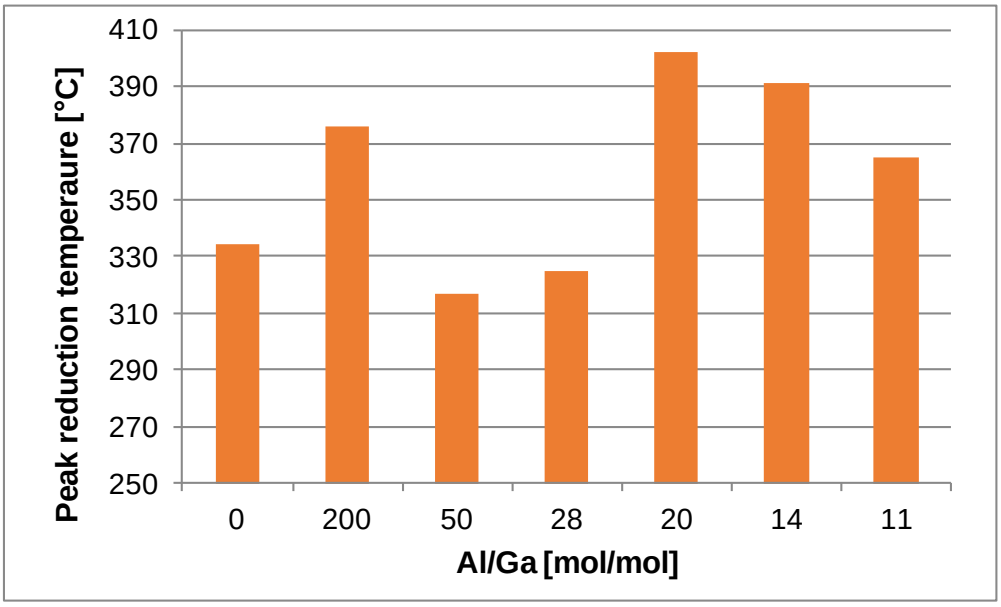

Figure 3.57 Temperature of the reduction peak observed for the calcined ZAC041cGax catalysts.

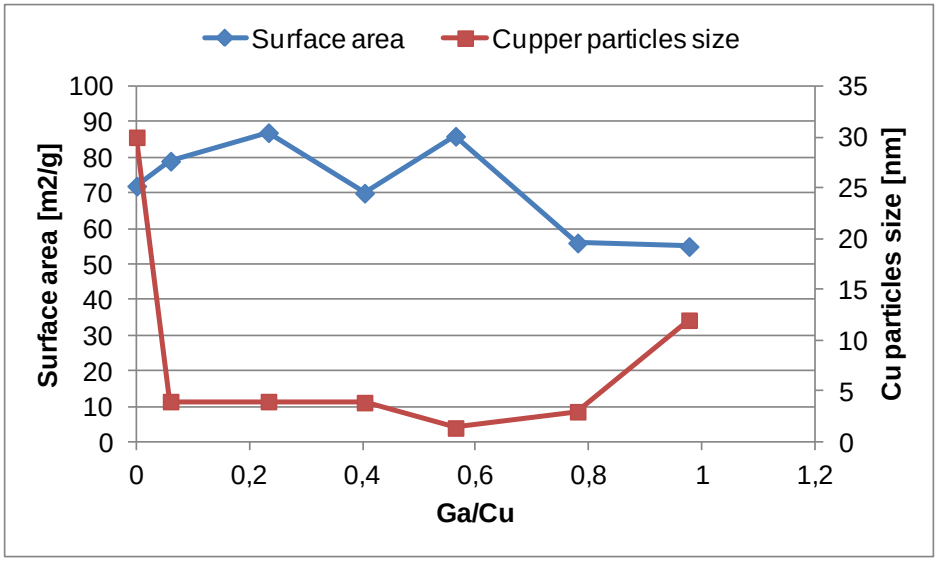

Figure 3.58. Surface area and Cu particle size on fresh ZAC041cGaX catalysts as a function of Ga content.

All the Ga doped catalysts were tested in HTS reaction conditions, using a S/DG ratio of 0.55v/v. In Figure 3.59 are reported the CO conversion obtained in tests performed at 350, 400 and 450°C.

After the last test at 450°C, test number 2 was repeated to evaluate the catalyst deactivation (Figure 3.59). By increasing of the temperature, already at 400°C, all samples reach the equilibrium values. To point out the differences in terms of activity, in Figure 3.60 are reported the values of CO conversion as a function of contact time obtained in tests performed at 350°C and with S/DG of 0.55vv. In particular, in Figure 3.61 is reported the CO conversion obtained in test 2 at T= 350°C, τ = 0.5s and S/DG= 0.55v/v with the different catalysts.

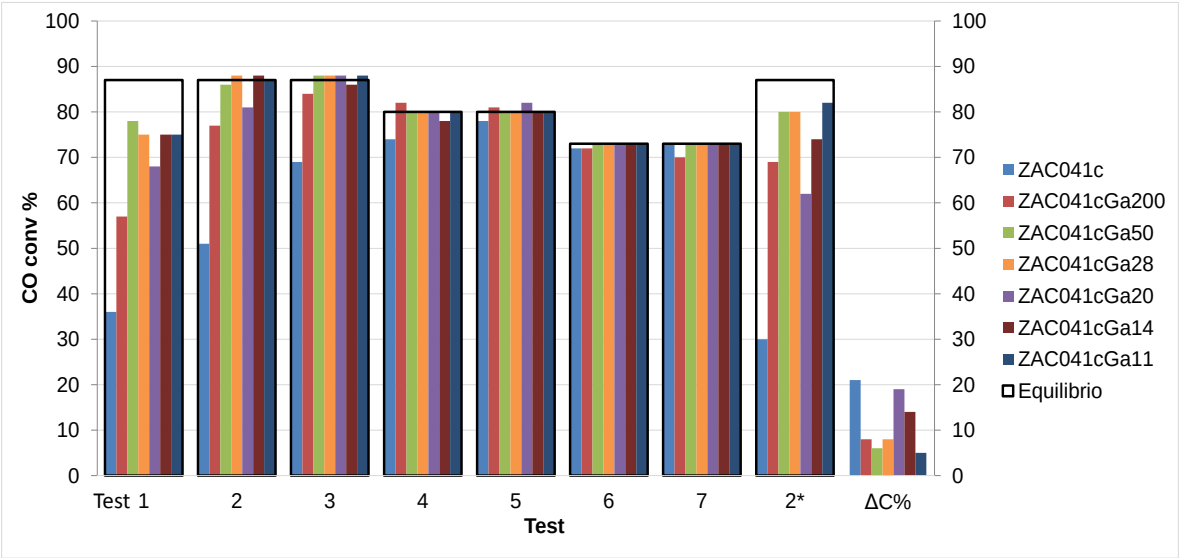

Figure 3.59 CO conversion percent obtained in test performed with the Ga containing catalysts using a S/DG ratio equal to 0.55v/v.

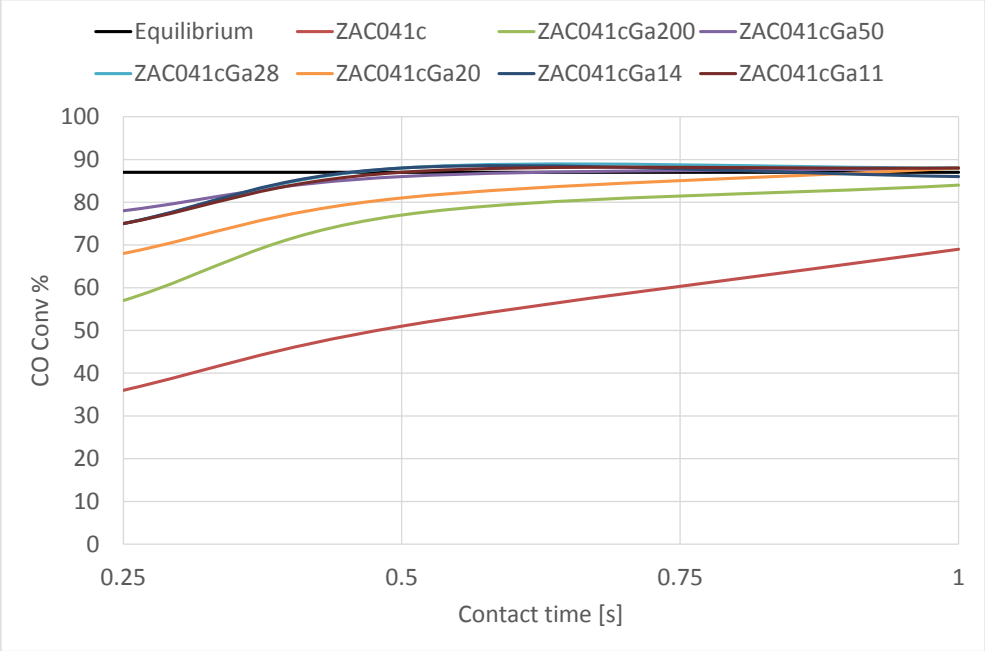

Figure 3.60 CO conversion percent obtained in test performed with the Ga containing catalysts at S/DG=0.55v/v and T= 350°C.

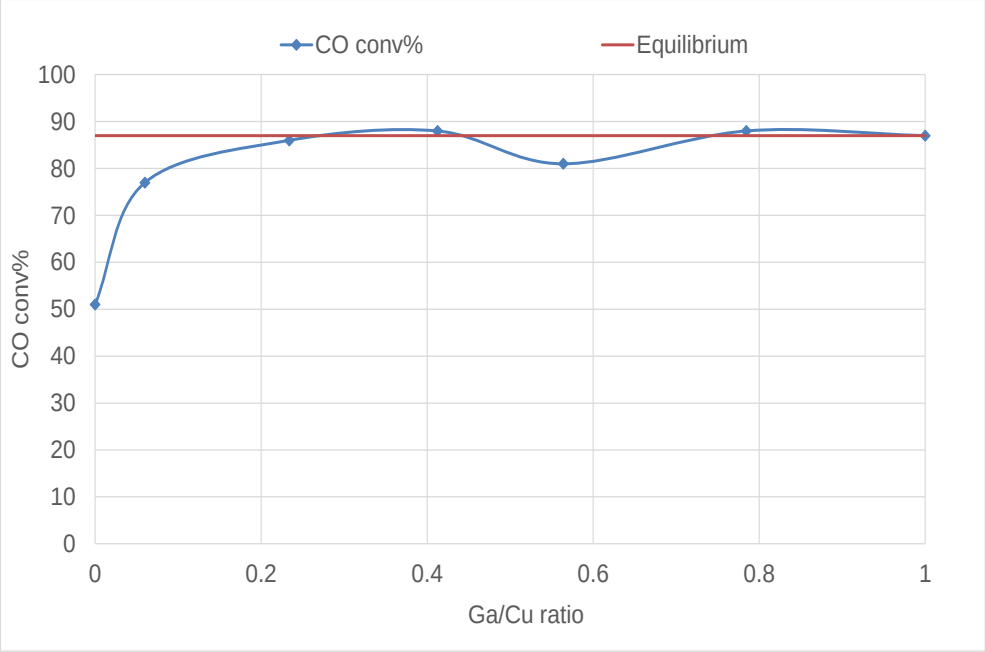

Figure 3.61 CO percent convention obtained in test 2; S/DG =0.55v/v; T= 350°C; τ= 0.5s .

Figure 3.61 show that the presence of Ga strongly affects the catalytic performances, with at first an almost linear increase of CO conversion with the amount of Ga, less evident for high contact times because all the doped samples reach the equilibrium values. A little amount of Ga (ZAC041cGa200 catalyst) is sufficient to dramatically increase the CO conversion. A further increase of Ga leads to a further increase of catalytic activity reaching in the case of ZAC041cGa50 the equilibrium value.

Higher amounts of Ga do not affect the CO conversion, which remain fixed to the equilibrium value, with the exception of the ZAC041cGa20 catalyst that evidences a decrease in CO conversion. The decrease in CO conversion observed for this last sample is accompanied by the lowest reducibility observed in the TPR analysis of the calcined catalyst.

TPR analysis performed on the spent catalysts (Figure 3.62), show that Cu particles present a lower reducibility respect to those of the calcined catalysts and that of spent undoped one. This result may be attributed to a higher interaction between metal particles and oxide matrix. In fact, regardless the increased reducibility observed after reaction, the cupper particles appear to be stable in the reaction conditions. In fact, sintering phenomena are not observed (Figure 3.63), with only a decrease of the specific surface area values that become comparable for all the catalysts.

XRD analyses performed on the spent catalysts show interesting results (Figure 3.64); ZAC041c spent catalyst evidences the formation of a peak attributable to Cu^0. Increasing the Ga content, an increase of spinel phase and the disappearance of the peak attributable to Cu^0 are observed. Only the ZAC041cGa20 sample does not respect this trend, in fact, in this case the amount of spinel phase is comparable to that in the reference catalyst.

It may be supposed that the Ga addition favors the aluminate formation; Cu-containing spinel shows a modified Cu availability, enhancing the activity. The formation of Cu^{2+} containing spinel, with Ga^{3+} incorporated into the structure, may give rise to higher dispersed Cu^0 particles. This is in agreement with the lower CO conversion observed for ZAC041cGa20 catalyst, which shows a low spinel content.

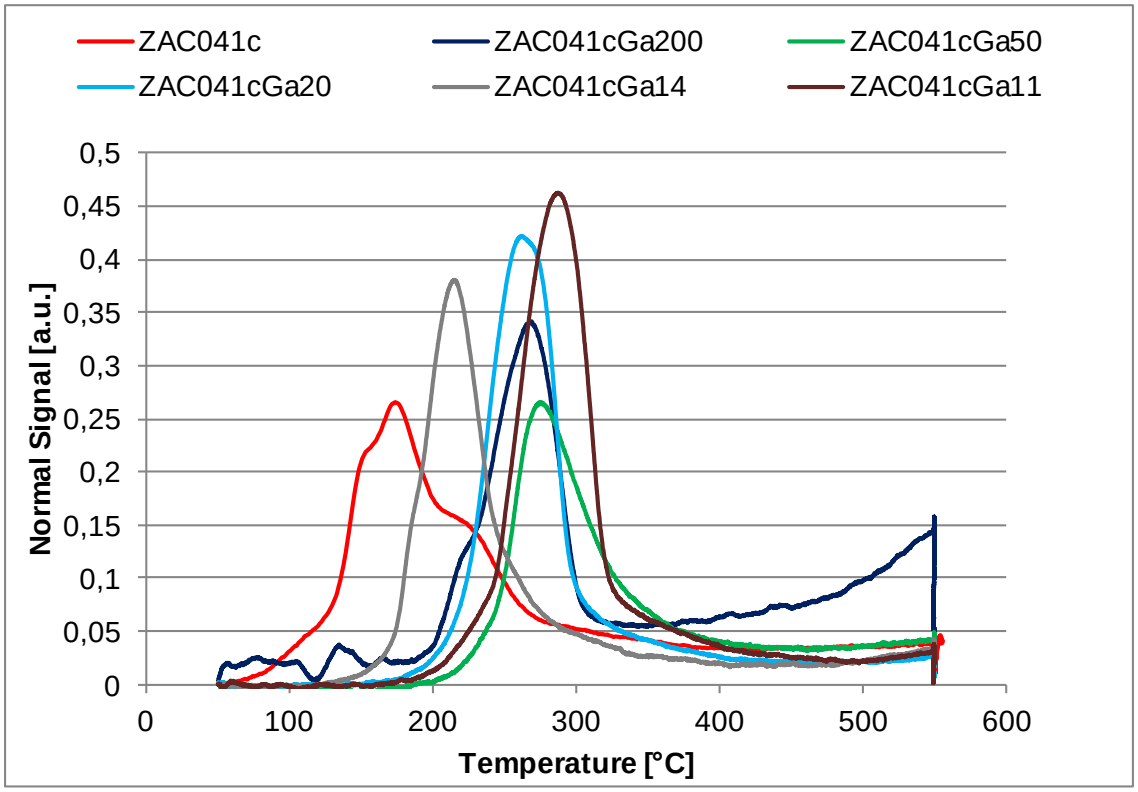

Figure 3.62 TPR analysis of spent ZAC041cGaX catalysts.

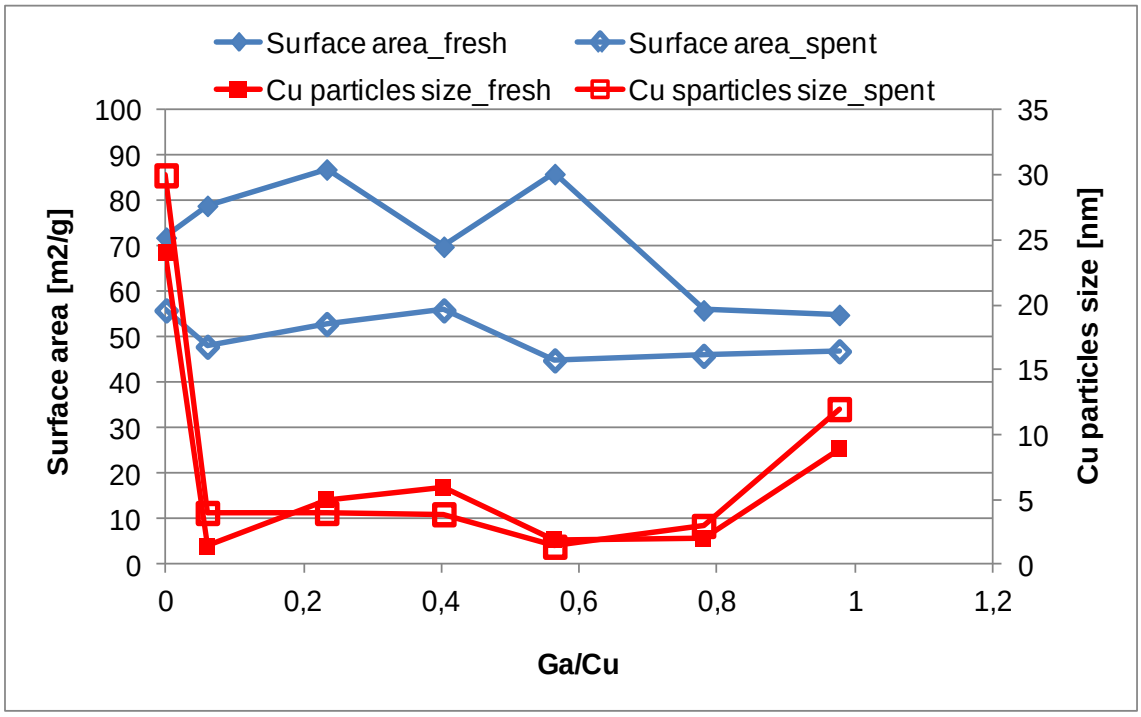

Figure 3.63 Surface area and Cu particle size on fresh and spent ZAC041cGaX catalysts as a function of Ga content.

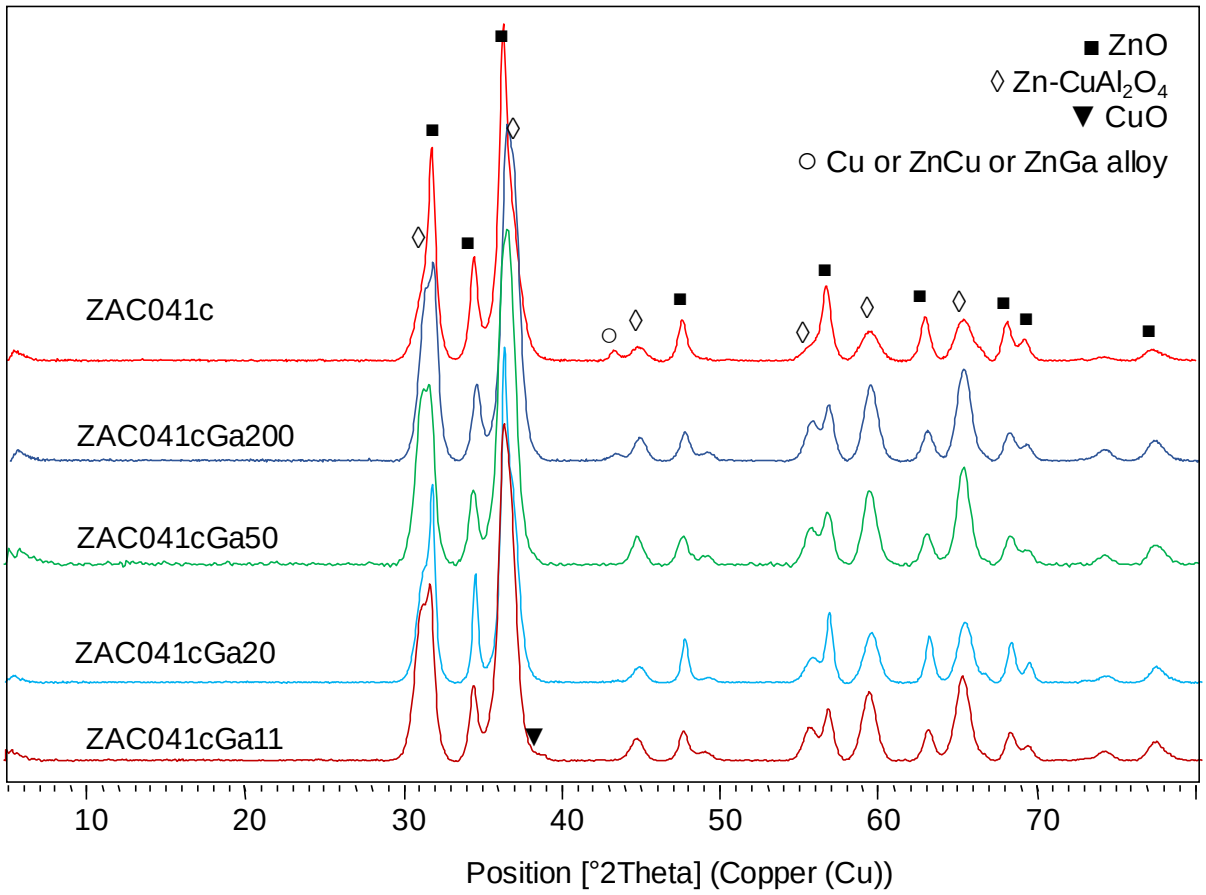

Figure 3.64 XRD pattens of spent ZAC041cGaX catalysts.

3.2.2 Correlation between crystalline structure and catalytic activity

From the previous results, it is clear that the Ga acts as a promoter in the WGS reaction for the CO oxidation. However, to point out the nature of the effect it is necessary to study the role of the different phases on the global catalytic activity. With this aim, some model samples were prepared:

- Pure spinel samples
- Modified ZAC catalysts.

3.2.3 $CuAl_2O_4$ and $CuGa_2O_4$: stability and activity of the spinel phases in the WGS reaction

It is known from literature that different type of spinels are active in the WGS reaction, in particular in LTS conditions [31]. In case of CuO-Al_2O_3-$CuAl_2O_4$ systems reported in literature, it is not defined what are the specific contributions of the different species, and to evaluate each contribution it is necessary to obtain pure spinel phases.

As shown in Figure 3.65, for the normal spinel ($[A^{2+}][B^{3+}]_2O_4$), all of the divalent cations are located in the tetrahedral sites, while trivalent cations are present in octahedral sites. On the

contrary, divalent cations in the inverse spinel ($[B^{3+}][A^{2+}B^{3+}]O_4$) occupied the octahedral sites and the trivalent cations are equally distributed in the tetrahedral and octahedral sites.

In case of $CuAl_2O_4$, Cu^{2+} have a lower octahedral site preference energy (-0.1Kcal/g atomic weight) that Al^{3+} (-2.5 Kcal/g atomic weight) [32]; thus the obtained spinel has a normal distribution.

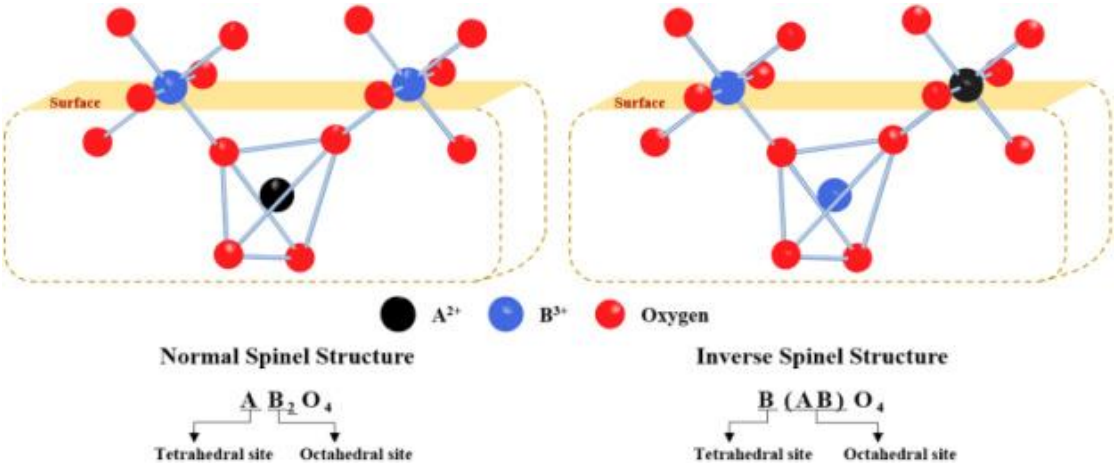

Figure 3.65 Normal and inverse spinel structure schema [33].

The spinel was prepared by sol-gel techniques, starting from Cu and Al nitrates. After drying, the precursor was calcined at different temperatures to evaluate the selectivity in the phase formation.

Figure 3.66 shows that also after calcination at 800°C there is the further presence of CuO, by increasing the temperature the peaks related to CuO are less intense. Although the spinel formation is favored by the temperature [34], it was not possible to obtain a pure spinel phase. To completely remove the traces of CuO phase, the material underwent an ammonia leaching. The formation of the cupro-ammonia complex leads to a complete elimination of the CuO from the surface. The complete leaching of the CuO was verified both by UV-Vis analysis on the extracting solution and XRD analysis.

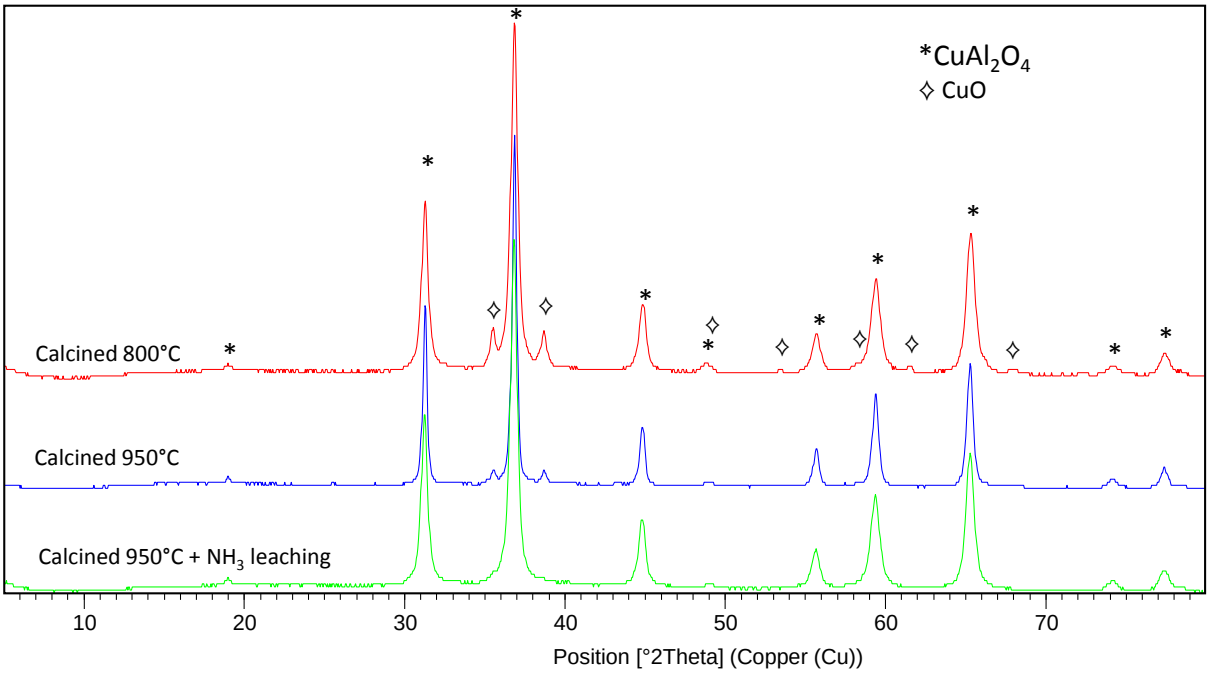

Figure 3.66 XRD patterns of $CuAl_2O_4$; effect of calcination temperature and NH_3 leaching.

On the pure $CuAl_2O_4$ it was performed a TPR-O-R analysis to evaluate the reducibility of the material (Figure 3.67). The reduction of the Cu^{2+} in the spinel occurs at 500°C, with a small peak at 400°C that may be attributed to the reduction of small spinel particles (this peak cannot be attributed to the reduction of CuO particle considering the high temperature value). During the oxidation step all the Cu containing particles are fully reoxidized at T<230°C, mainly below 150°C (Figure 3.68). The easy oxidation of dispersed Cu^0 is well known and is the reason of the complete oxidation already at room temperature (pyrophoric effect) of low sized-highly dispersed particles.

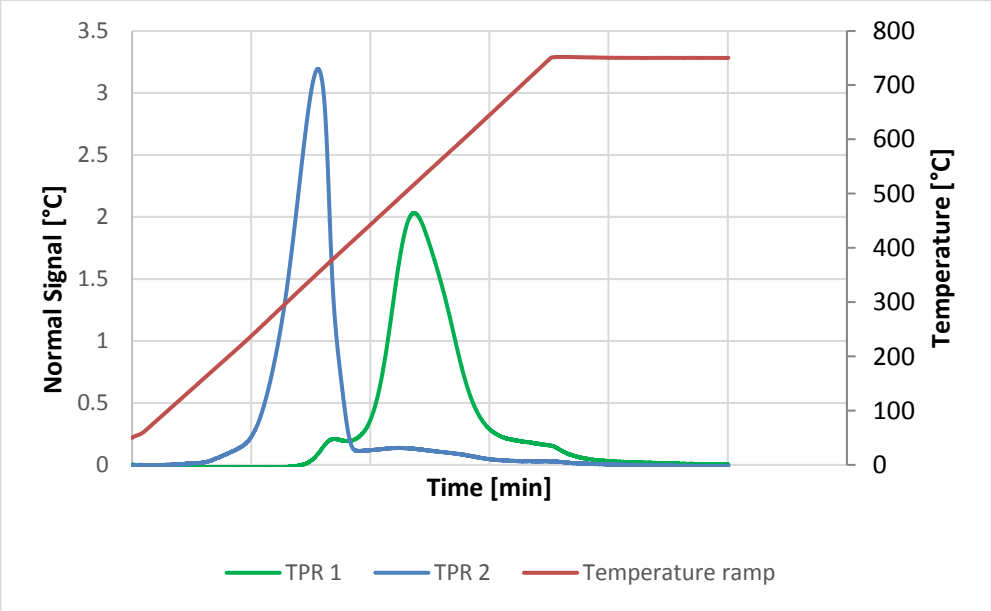

Figure 3.67 TPR profiles of pure $CuAl_2O_4$ catalyst during the two reduction steps.

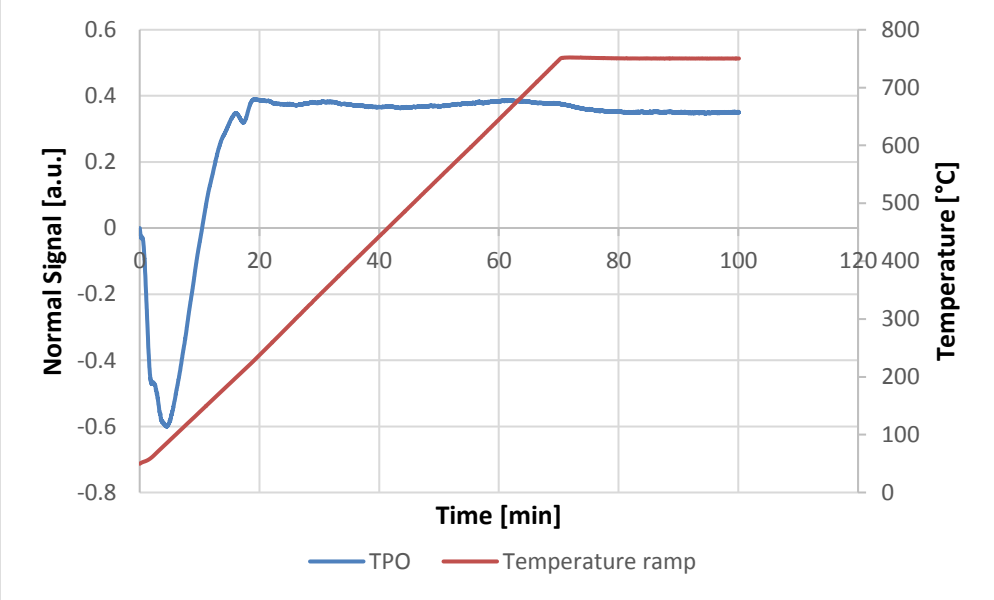

Figure 3.68 TPO profile of pure $CuAl_2O_4$ catalyst during the oxidation step.

Both the un-leached and the leached catalysts were tested in HTS tests with a S/DG ratio equal to 0.55v/v. The un-leached sample is characterized by a 1wt% of Cu on the surface (in form of CuO before activation). The results obtained are interesting; the activity obtained with the "free" CuO-containing catalyst is lower respect to that obtained with the pure spinel phase (Figure 3.69).

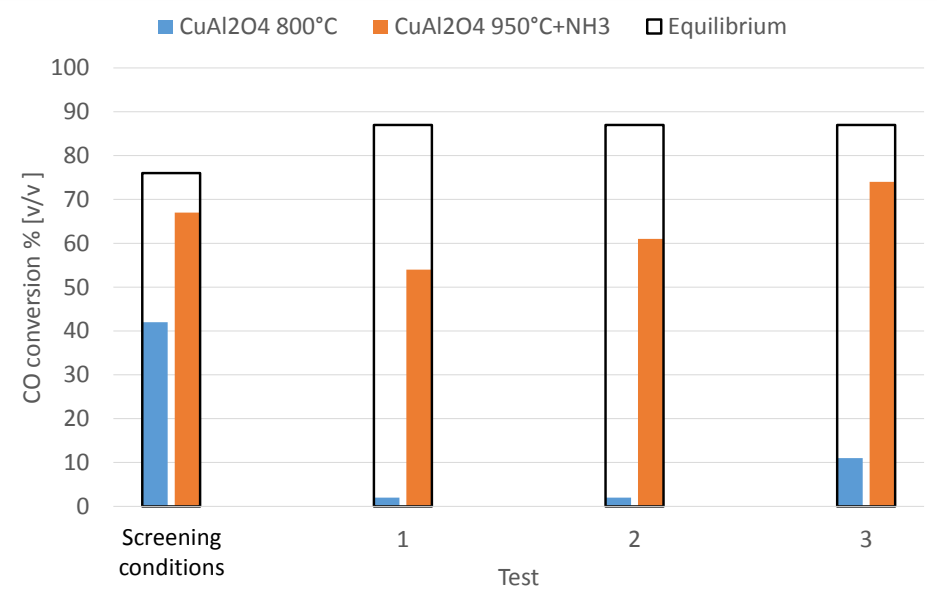

Figure 3.69 Conversion percent obtained in the different tests performed on $CuAl_2O_4$ calcined at 800°C and on the $CuAl_2O_4$ calcined at 950°C and leached by NH_3.

This result is not trivial because the difference between the two samples is only the presence or not of CuO on the surface, which is active in the WGS reaction.

By XRD analyses performed on the spent catalysts it is possible to see that, in both samples, the spinel is completely decomposed. Even if the reaction temperature is below the reduction temperature reported in TPR analysis, the Cu^{2+} in the spinel structure is completely reduced. The Cu oxides phases observed are due to the reoxidation of the Cu^0 small particles.

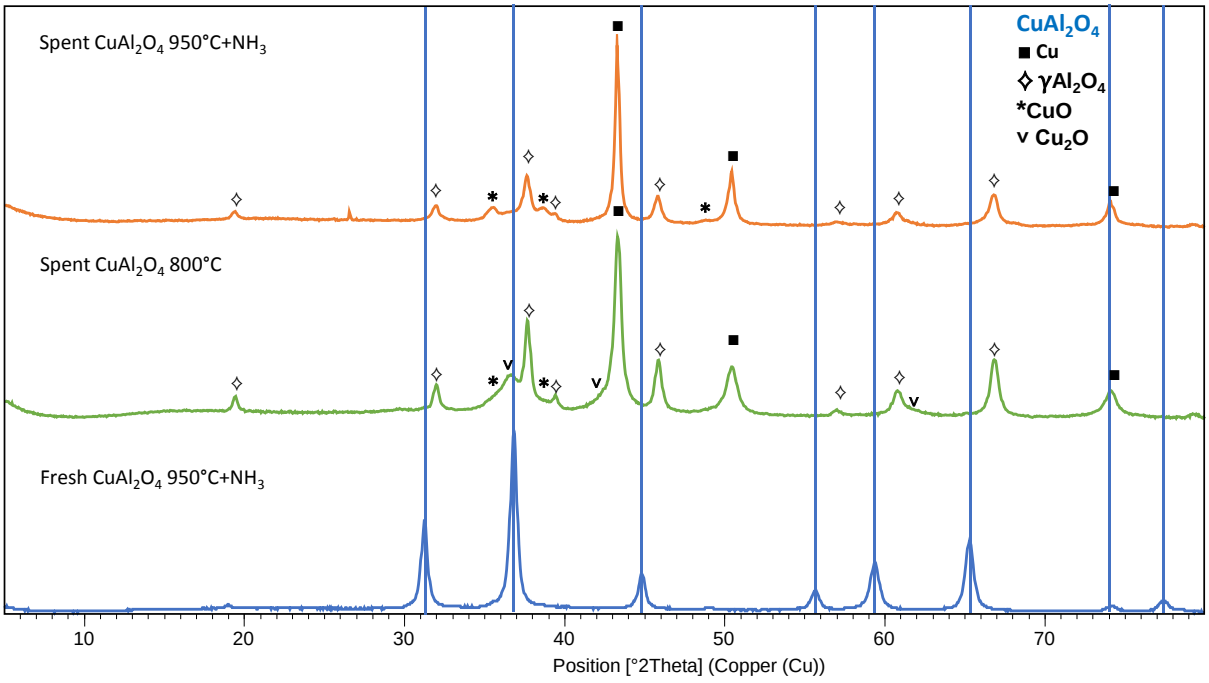

Figure 3.70 XRD patterns of the spent leached and un-leached $CuAl_2O_4$ samples.

On the two spent samples were performed TPR analysis (Figure 3.71). The amount of reducible cupper oxides depends to the size of the metal Cu particles present on the catalyst surface after activation. The particles which undergo oxidation are those characterized by low size, responsible of the cupper oxides phases detectable in XRD patterns. Large Cu^0 particles are merely passivated on the surface.

The reduction temperatures obtained are the same for both the spent samples.

From the TPR analysis it is possible to measure the reducibility of the samples. In Table 3.34 are reported the amount of H_2 consumed for the two spent samples, calculated comparing the hydrogen consumption obtained during the TPR analysis and the total amount of Cu^{2+} species in for calcined samples (CuO and $CuAl_2O_4$).

The spent pure spinel shows a higher reducibility, correlated to a higher dispersion of the Cu^0 that gives rise to better catalytic performances. The low reducibility of the un-leached sample may be also correlated to the presence of Cu_2O, which need a lower amount of hydrogen to be reduced.

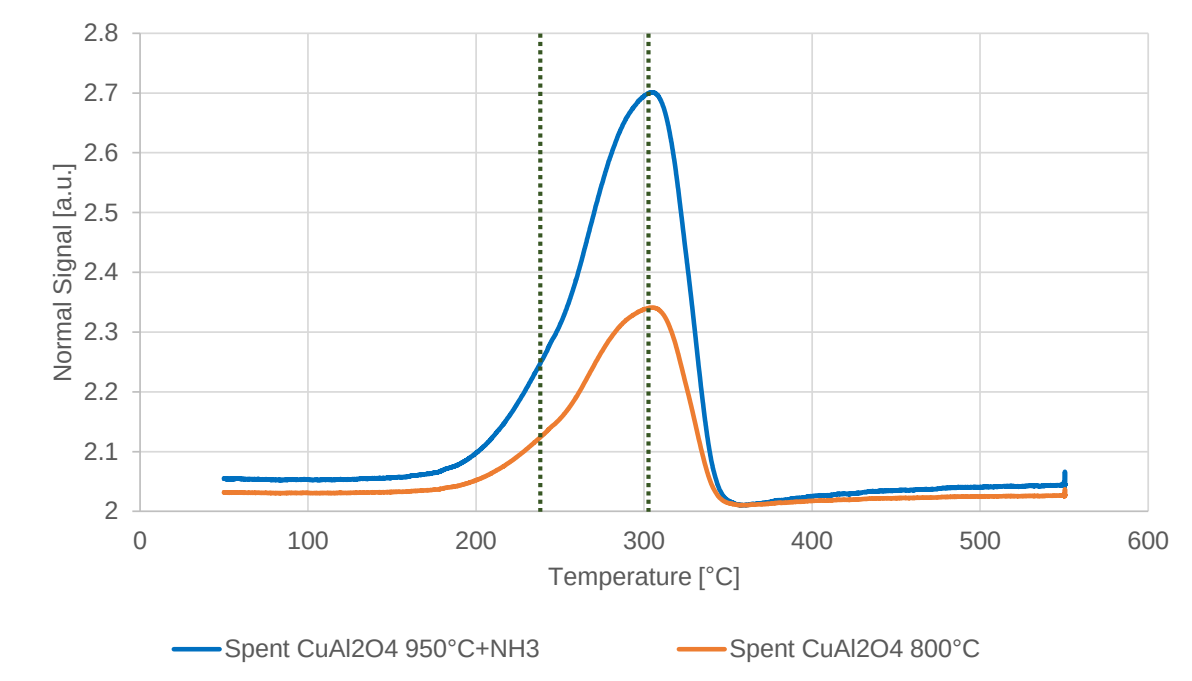

Figure 3.71 TPR profile of catalyst leached and un-leached spent $CuAl_2O_4$ catalysts.

	$CuAl_2O_4$ 800°C	**$CuAl_2O_4$ 950°C+NH_3**
H_2 consumed/Cu^{2+} species	0.658	0.862

Table 3.34 Reducibility of the un-leached and leached spent catalysts.

In presence of Cu^0 particles in the starting material, the Cu^0 produced during spinel reduction may migrate on the pre-existent particles increasing the size and reducing the activity.

Also $CuGa_2O_4$ was synthesized via sol-gel technique. Unlike, that observed for $CuAl_2O_4$, the increase of the calcination temperature do not significantly improve the amount of the spinel phase (Figure 3.72).

Before being tested in HTS reaction, the $CuGa_2O_4$ sample was treated by NH_3 solution to completely remove Cu and Ga oxides.

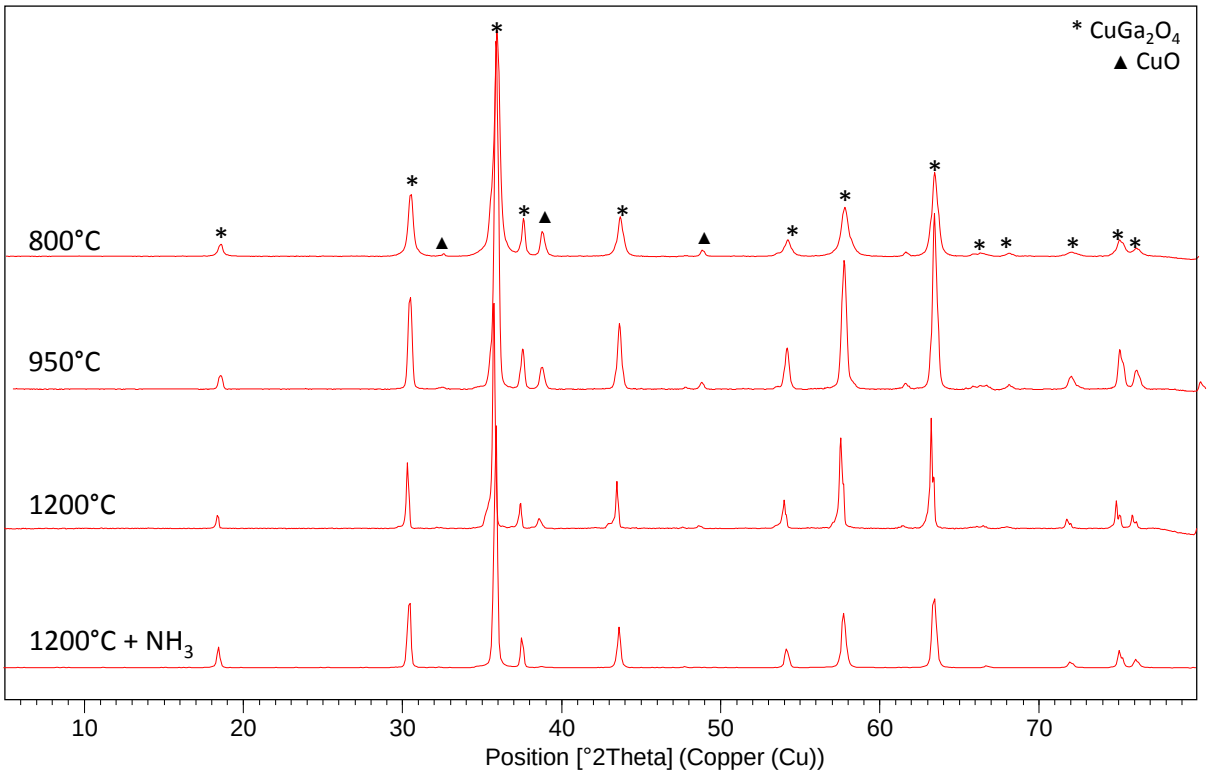

Figure 3.72 XRD patterns of $CuGa_2O_4$; effect of the calcination temperature on the sample formation.

TPR-O-R analysis show a very interesting behavior. It is known that the reduction of Ga_2O_3 species occur near 610° C [35]. In first TPR test it is possible to see a first peak at 427°C, attributable to spinel reduction, with two shoulders at 346 and 376°C. The brooding of the observed peak indicates a wide distribution of Cu-O species with different reducibility. A second peak at 600°C is present. After oxidation, the second TPR analysis shows two peaks; the first one at 268°C is due to the reduction of CuO particles, while the second at 348°C is difficult to be assigned.

$CuGa_2O_4$ pure spinel was tested in HTS conditions; Figure 3.74 report the CO conversions obtained, compared with those of $CuAl_2O_4$. It is possible to see that the reactivity obtained for the $CuGa_2O_4$ sample is lower than the previous one.

This effect may be explained by XRD analysis performed on the spent $CuGa_2O_4$ (Figure 3.75). In fact, on the spent sample it is possible to still observe the pattern of $CuGa_2O_4$, unlike the spent $CuAl_2O_4$.

Even if the Ga spinel shows a higher reducibility compared to the Al spinel in TPR experiments, it is more stable under HTS reaction conditions. The increase of the activity observed in ZAC041cGaX catalysts is not due to the activity of $CuGa_2O_4$. On the contrary, the controlled reduction of the spinel may produce well defined Cu^0 particles and justify the sizes observed on the spent catalyst.

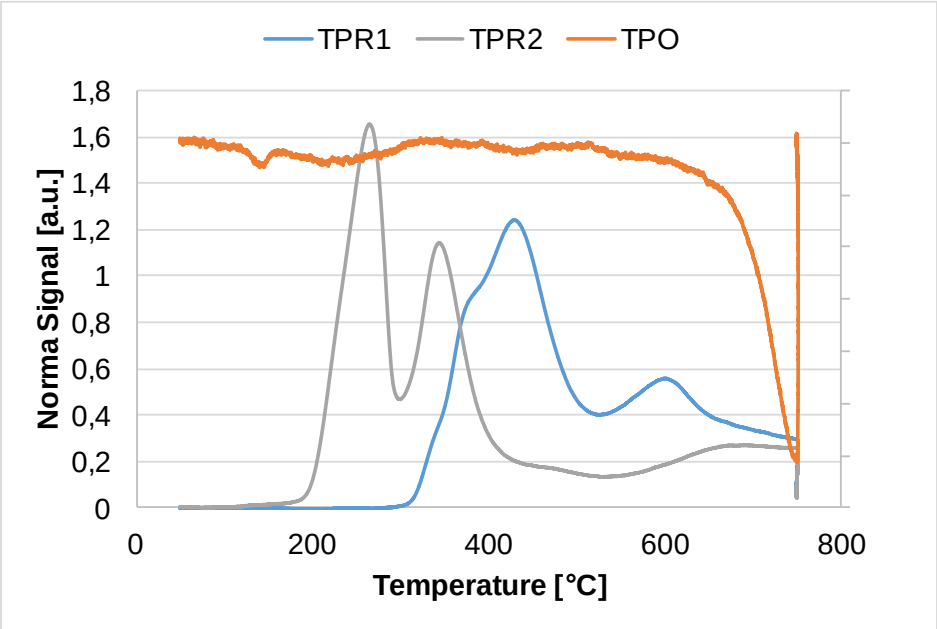

Figure 3.73 TPR-O-R analysis of pure $CuGa_2O_4$.

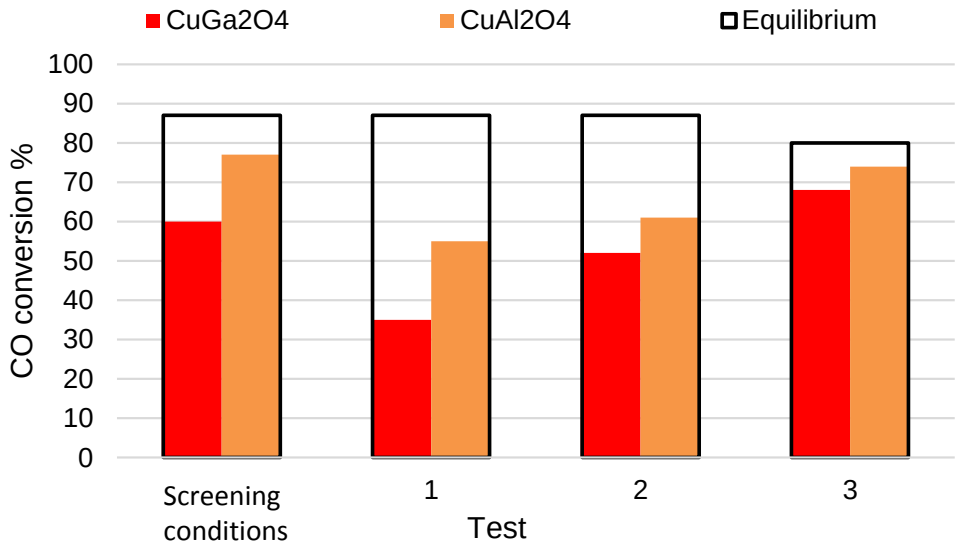

Figure 3.74 CO conversion obtained in HTS tests with $CuGa_2O_4$ and $CuAl_2O_4$.

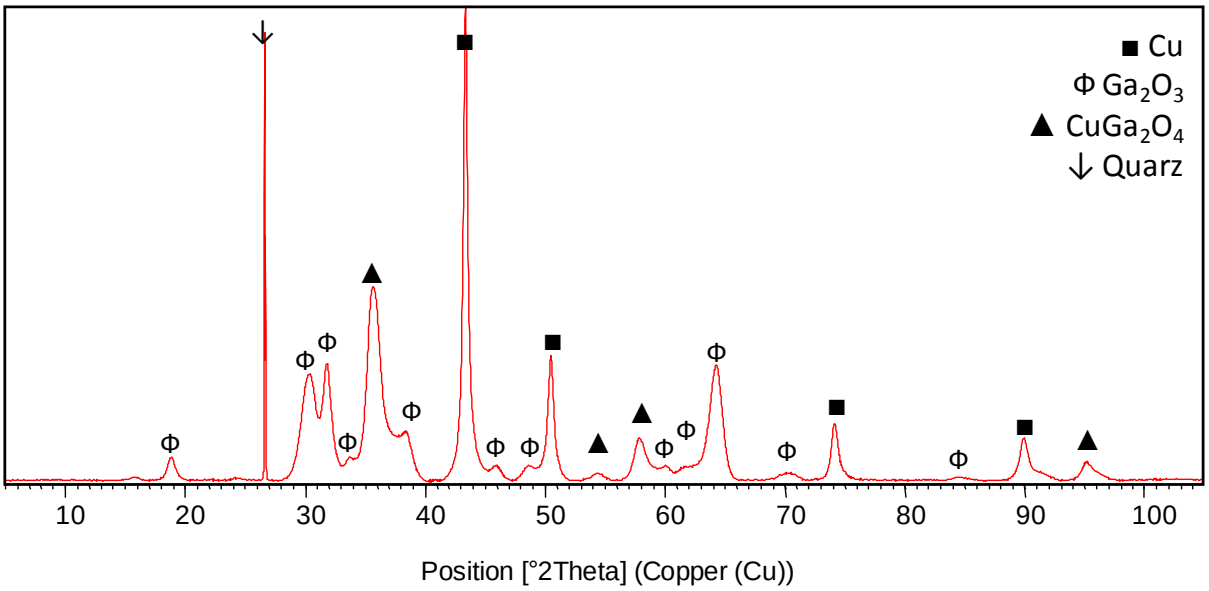

Figure 3.75 XRD pattern of spent $CuGa_2O_4$.

3.2.4 Model catalysts: modified ZAC catalysts

Starting from the reference catalysts ZAC041c and ZAC041cGa50, two model systems were synthesized:

- ZGaC: is obtained by complete substitution of Al with Ga in the ZAC041c catalyst.
- ZAGa: is obtained replacing the composition of ZAC041cGa50 catalyst but without Cu.

In the XRD patterns of both dried precursors, it is possible to see the formation of hydrotalcite-type phases (Figure 3.76). The replacement of Al with Ga give rise to a peaks shift at lower 2θ° values, given by the bigger M^{3+} ion.

After calcination, the formed phases are similar for the two systems (Figure 3.77, Figure 3.78). ZnO is observed in both materials. ZGaC catalyst shows the presence of $ZnGa_2O_4$ while ZAGa catalyst the corresponding $ZnAl_2O_4$.

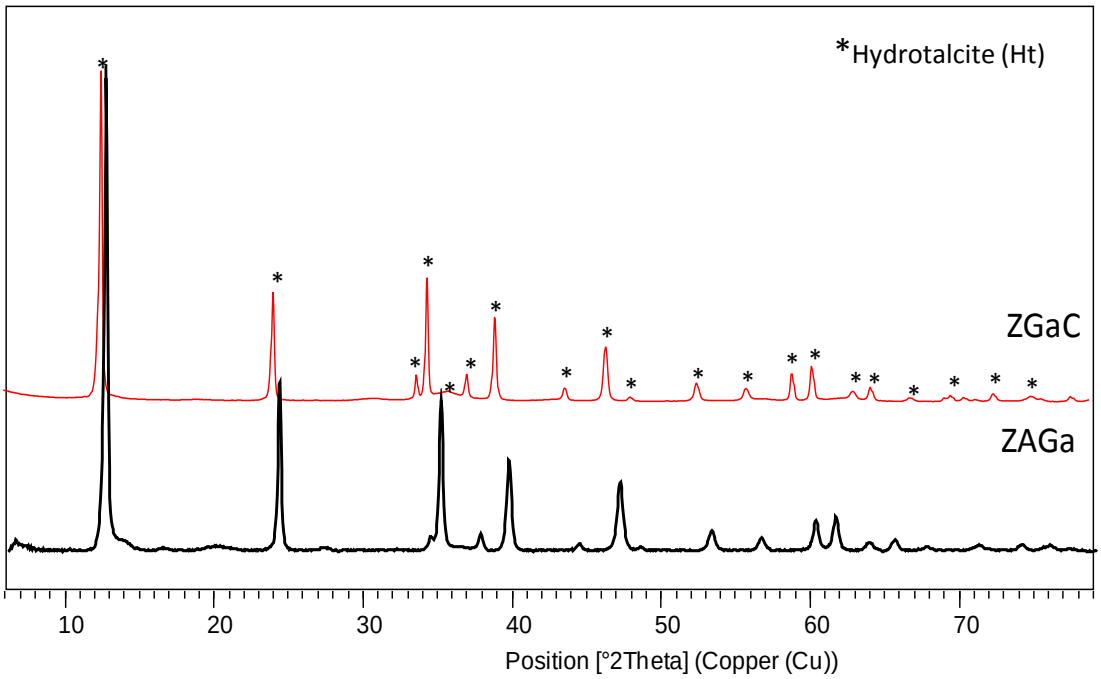

Figure 3.76 XRD pattern of ZGaC and ZAGa dried precursors.

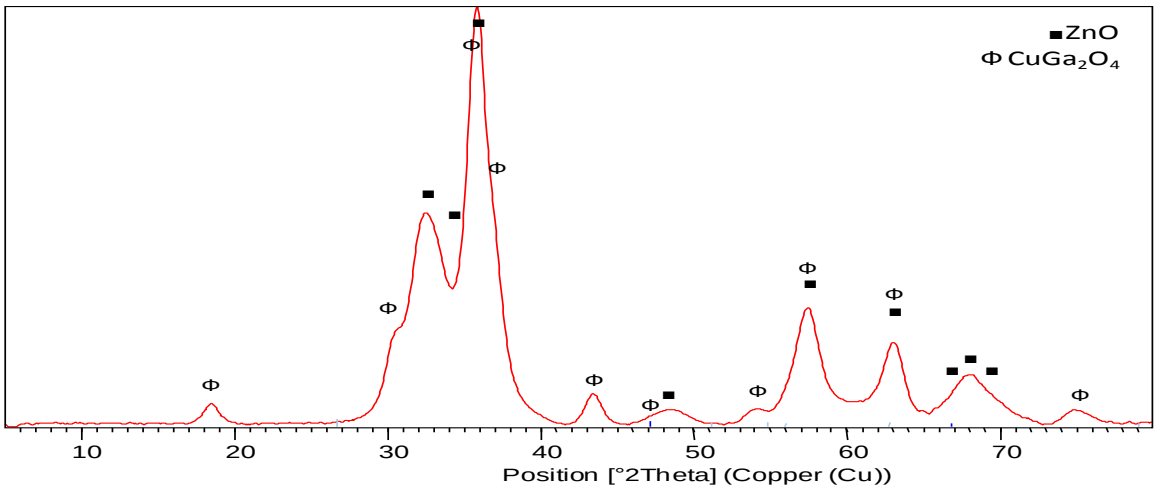

Figure 3.77 XRD pattern of calcined ZGAC catalyst.

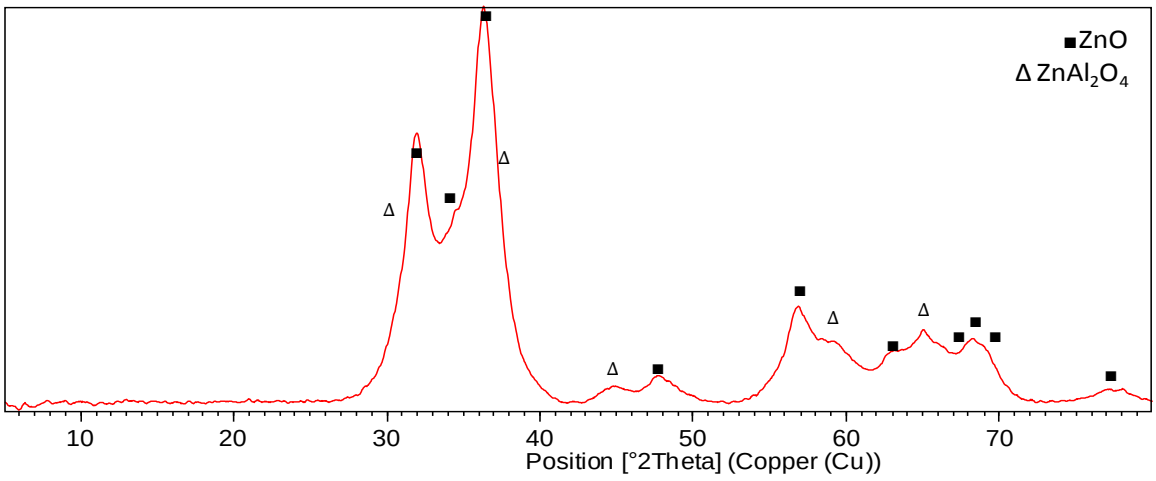

Figure 3.78 XRD pattern of calcined ZAGa catalyst.

In Figure 3.79 the reactivity of ZAC041c and ZGaC catalysts are compared. The catalytic activity of ZGaC shows an important increase; in fact, already in test 1, an increase of 30%in the CO conversion is observed. Furthermore, the Ga-containing catalyst shows a lower deactivation under HTS reaction conditions. This results is unexpected, in fact, it was previously reported that pure $CuGa_2O_4$ spinel shows a lower reactivity respect to the corresponding $CuAl_2O_4$ spinel.

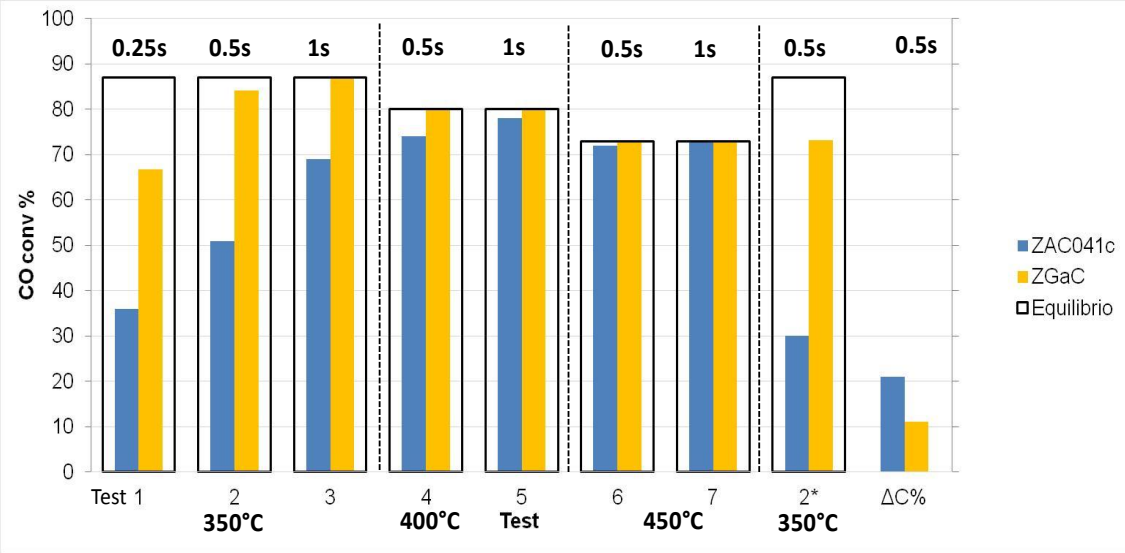

Figure 3.79 CO conversion obtained in tests performed with ZAC041c and ZGaC catalysts.

The TPR analyses performed on calcined catalysts (Figure 3.80), show that the substitution of Al with Ga gives rise to a decrease in the reduction temperature, which may be correlated to a lower interaction between the Cu^0 particles and the oxide matrix, and to their smaller size. On the contrary, after reaction, the reduction temperature of ZGaC catalyst is higher. XRD analysis performed on spent material (Figure 3.81) shows an increase of crystallinity, without the presence of Cu^0 or CuO patterns.

The higher activity may be explained considering two different aspects: i) Cu particles obtained during HTS reaction are smaller respect to those formed in the ZAC041c catalyst, more interacting with the oxide matrix; ii) the role of ZnO. As already discussed, ZnO is not active in WGS reaction itself. Its role in the reactivity is due to the spill-over phenomena that occurs on catalysts surface. As reported in literature, reaction intermediates formed on Cu surface move to ZnO before desorbing from the catalyst.

In ZGaC catalyst, the oxide matrix is modified and a high amount of $ZnGa_2O_4$ is formed. Considering the oxides reducibility, in known in literature that in $ZnGa_2O_4$ the reduction of Zn^{2+} to Zn^{+} is facilitate respect to ZnO [36]. This increased reducibility is accompanied by the

formation of vacancies. Spinel structures may also generate oxygen vacancies at high temperature or under reducing conditions, with an excess of electrons favoring the reduction of cations and forming nonstoichiometric oxide. It may be hypothesized that this spinel is active in the WGS reaction, contributing to the overall behaviors.

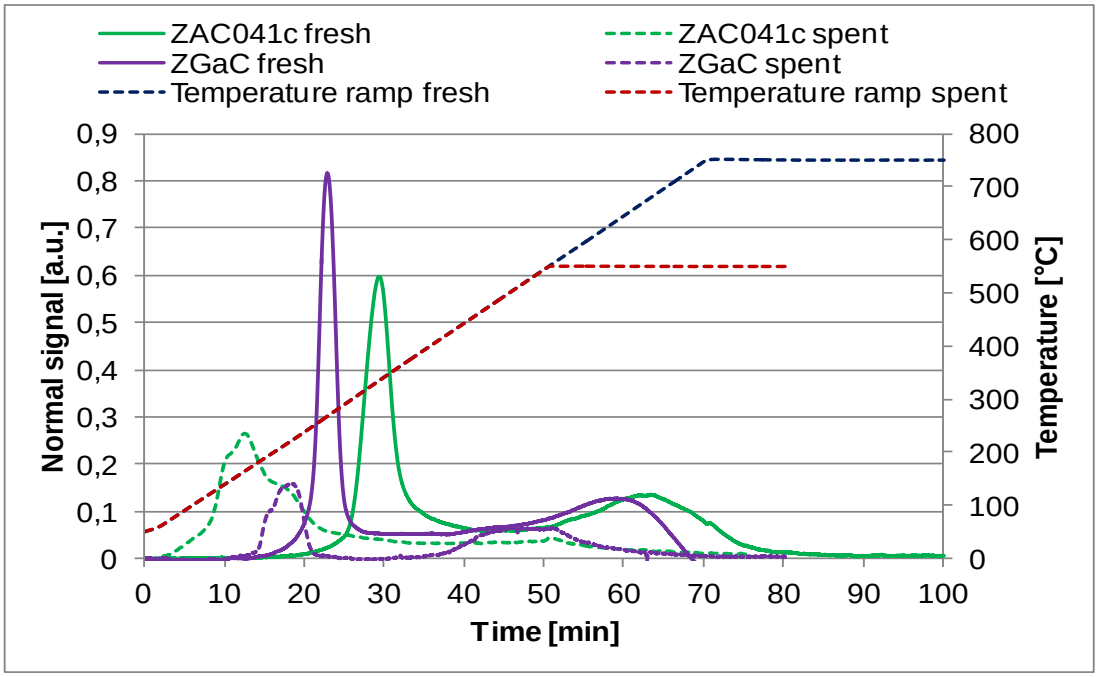

Figure 3.80 TPR analysis of fresh and spent ZAC041c and ZGaC catalysts.

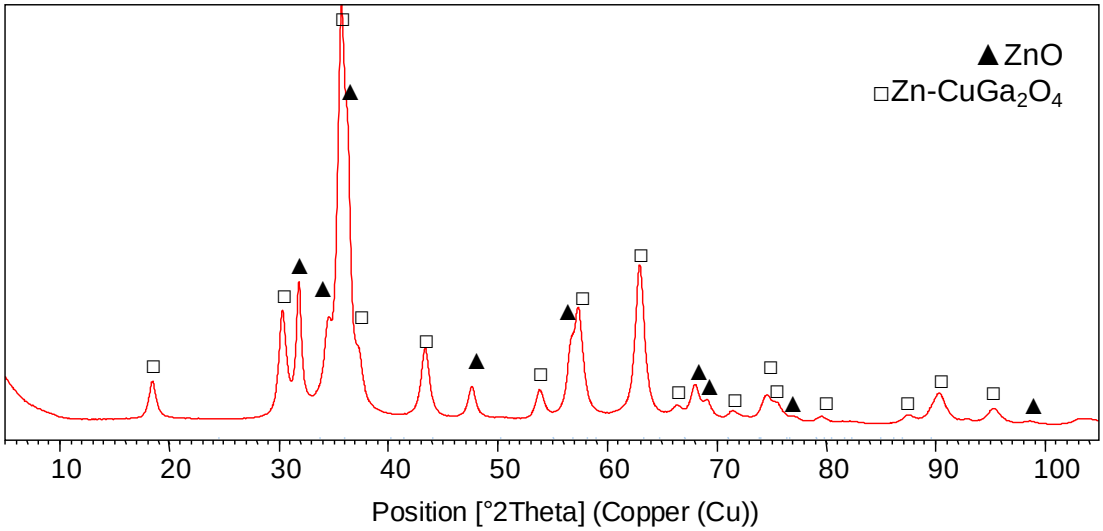

Figure 3.81 XRD pattern of spent ZGaC catalyst.

To point out the effect of Ga on the oxide phase activity, ZAGa was tested in HTS reaction conditions and compared to ZAC041c and ZAC041cGa50 (Figure 3.82). At 350°C, the activity is very low; in fact it is necessary to increase the contact time value to obtain minimum

conversion of CO. By increasing the temperature, the CO conversions increases, remaining lower than those observed for both the references systems.

The activity observed for the ZACcGa50 catalyst may not be directly assumed as the sum of the reactivity of each active phase (Cu and Ga), as it is possible to see in the CO conversion obtained in test 1 reported in Figure 3.82.

In fact, the conversion obtained with the doped ZAC catalyst is higher than to the sum of the conversion of ZAC041c and ZAGa.

Considering that ZnO, Al_2O_3 and $ZnAl_2O_4$ are not active in the WGS reaction, the observed activity may be correlated to the addition of Ga^{3+} to the oxide matrix and to the vacancies formed already discussed. At the same time the deactivation observed after reaction is higher respect to the other catalysts.

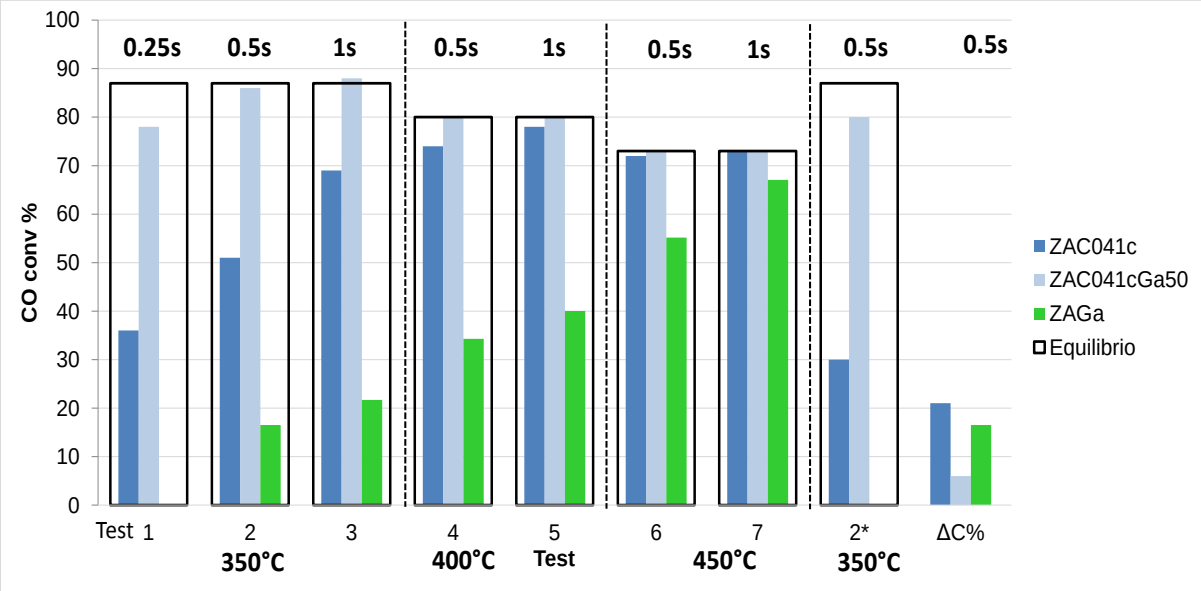

Figure 3.82 Activity of ZAGa, ZAC041c and ZAC041cGa50 in HTS reaction conditions.

ZAGa catalyst is Cu free, so the reducibility observed in TPR analysis (Figure 3.83) is very low in terms of hydrogen consumption respect to the corresponding ZAC041cGa50 catalyst. It is possible to see two peaks; the first one at 445°C and the second at 704°C, correlated to the reduction of no-stoichiometric spinel phases. After reaction a single peak centered at 550°C is observed, temperature similar to that of the second reduction peak observed in the ZGaC spent catalyst.

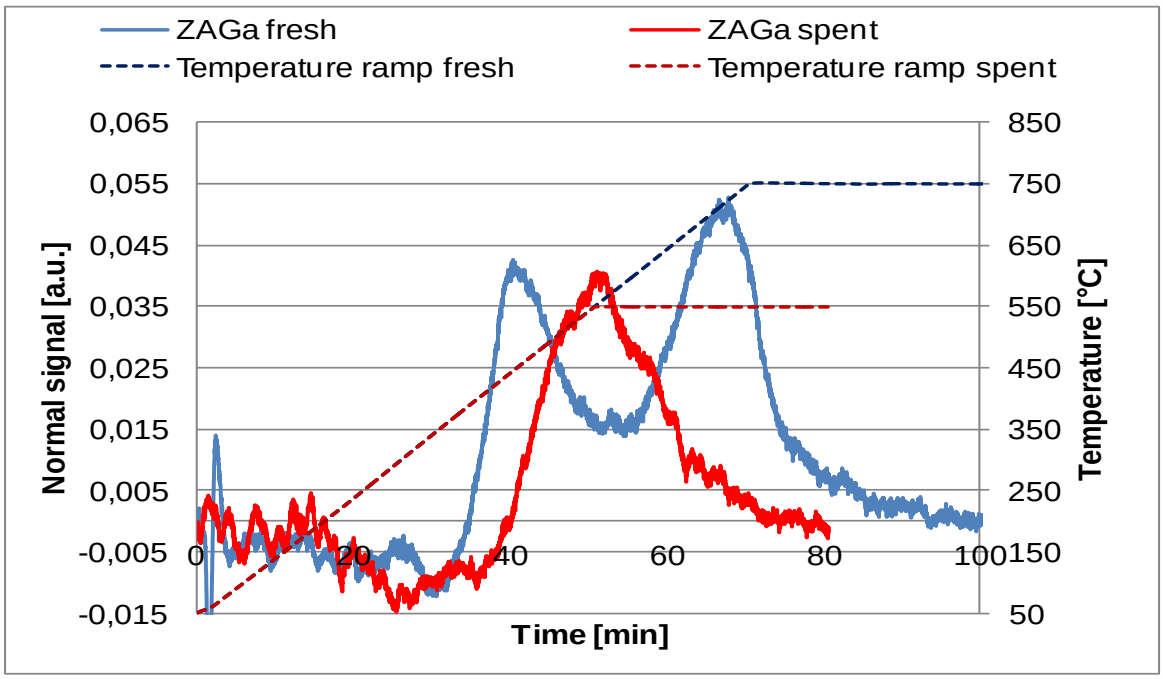

Figure 3.83 TPR analysis of fresh and spent ZAGa catalyst.

3.2.5 Conclusions

The study of an innovative formulation for the HTS was the aim of this chapter. A Cu/Zn/Al catalyst, which previously showed very interesting properties was modified in order to further improve the CO conversion and stability of the active phase. The introduction of La, In and Ga led to different catalytic behaviors; in particular, the In-modified sample showed worst catalytic performances, while doping by La and Ga allow to obtain very positive results. The structural modification induced by In resulted in a stronger interaction between Cu^0 particles and oxide matrix, leading to decrease the reducibility of the sample , with a corresponding decrease of the catalytic performances. La and Ga had positive effects in terms of particles dispersion and catalyst stability, leading to samples with improved catalytic properties. Focusing the attention on the Ga-doped sample, resulted the best formulation, a deep stydy was performed in order to identify its role in promoting stability and activity of Cu/Zn/Al type catalysts.

It was observed that Ga is able to promote the activity also in very small amount, reaching maximum that remain stable for the range of composition analyzed.

The Ga-containing sample respect to the reference catalyst showed an important increase of Cu^0 dispersion and stabilization under reaction conditions. This effect was attributed to the capacity of Ga to promote stable spinel phases that hinder the complete segregation of Cu^0 on the surface, with sintering phenomena that deactivate the catalysts. This role of Ga was

confirmed by formulating model catalysts in which resulted evident: 1) Ga-containing oxides are active in the WGS reaction; 2) pure $CuGa_2O_4$ spinel stable in reaction conditions; 3) $CuAl_2O_4$quickly decomposes to Al_2O_3 and CuO, with an initial high activity, but undergoing fast deactivation.

In conclusion, promising formulation for HTS catalyst were proposed and the role of each element was justified, although further structural analyses are in progress to confirm the results collected.

References

1 M. Paris, Master's thesis, Facoltà di Chimica Industriale, ALMA MATER STUDIORUM, 2011.

2 G. Brenna, A. Vaccari, F. Basile, G. Fornasari, R. Faure, D. Gary, European Patent Application EP11306604.7 (2011) to Air Liquide

3 R.M. Sambrook, S. England US Patent 4,835,132 (1989).

4 D. W. Jeong, W. J. Jang, J. O. Shim, W. B. Han, H. S. Roh, U. H. Jung, W. L. Yoon, *Renew Energ* **65** (2014) 102.

5 L.Z. Liganiso, G. jacobs, K.G. Azzam, U.M. Graham, B.H. Davis, D.C. Cronauer, A.J. Kropf, C.L. Marshall *Appl. Catal. A* **394** (2011) 105.

6 L. Jiang, B. Ye, K. Wei *J. Rare Earths* **29** (2008) 352.

7 K. Nishida, D. Li, Y. Zhan, T. Shishido, Y. Oumi, T. Sano, K. Takehira, *Appl. Clay Sci*. **44** (2009) 211.

8 T. Shishido, M. Yamamoto, I. Atake, D. Li, Y. Tian, H. Morioka, M. Honda, T. Sano, K. Takehira, *J. Mol. Catal.* **A253** (2006) 270.

9 Y. Okamoto, K. Fukino, T. Imanaka, S. Teranishi, *J. Phys. Chem.* **87** (1983**)** 3740.

10 W. R. A. M. Robinson, J. C. Mol, *Appl. Catal.* **60** (1990) 61.

11 G. L. Castiglioni, A. Vaccari, G. Fierro, M. Inversi, M. Lo Jacono, G. Minelli, I. Pettiti, P. Porta, M. Gazzano, *Appl. Catal.* **123** (1995) 123.

12A. Finkelstein, *Bar.* **39** (1906) 1585.

13 J.Y. Luo, M. Meng, X.G. Li, Y.Q. Zha Micropor mesopor mat **113** (2008) 277.

14 M.V Twigg, Catalyst Handbook, 2nd ed., Wolf, London (UK), 1996.

15 A.-M. Hilmen, M. Xu, M. J.L. Gines, E. Iglesia, *Appl. Catal.* **A169** (1998) 355.

16 H. Ernst, H. Pfeifer, *J. Catal.* **136** (1992) 202.

17 S.V Gredig, R. Maurer, R.A. Koeppel, A. Baiker, *J. Mol. Catal.* **A127** (1997) 133.

18 G.T. Morgan, *Proc. Royal Soc. London* **A127** (1930) 246.

19 G.T. Morgan,D.N.V. Hardy, R.H. Procter, R. H., *J. Soc. Chem*. *Ind*. (1932) 511T.

20 J. M. Campos-Martın, J. L. G. Fierro, A. Guerrero-Ruiz, R. G. Herman, K. Klier *J. Catal.* **163** (1996) 418.

21 S. V. Gredig, R. A. Koeppel, A. Baiker, *Applied Catalysis* **162** (1997) 249.

22 W. Tong, A.West, K. Cheung, K.M. Yu, S.C. E. Tsang, *ACS Catal.* **3** (2013) 1231.

23 K. Hak-joo, J. Soon-kwan, P. Ki-tae, Y. M. Hye, S. KyoungHo, KP1016579580000 (2016) to Korea Institute of energy research

24 Y. Matsumura, H. Ishibe, *J. Power Sources* **209** (2012) 72.

25 M. Wonga, N. Coville, Appl. Catal. **A377** (2010) 150.

26 J. A. Dean Lange's, Handbook of Chemistry, 15th ed., McGraw-Hill, N.Y, (2005) 43.
27 L.A. Denisenko, A.A. Tsyganeko, V.N. Filimonov, *React. Kinet. Catal. Lett.* **25** (1984) 23.
28 N.-Y. Topsøe, H. Topsøe, *J. Mol. Catal.* **A 141** (1999) 95.
29 B.H. Sakakini, J. Tabatabaei, M.J. Watson, K.C. Waugh, *J. Mol. Catal.* **A162** (2000) 297.
30 J. Pritchard, T. Catterick, R.K.Gupta, *Surf. Sci*. **53** (1975) 1.
31 Y. Tanaka, T. Utaka, R. Kikuchi, K. Sasaki, K. Eguchi *Appl. Catal.* **A242** (2003) 287.
32 O. Muller, R. Roy, The Mayor Ternary Structural Families*,* Springer-Verlag, Berlin Heidelberg New York, 1974.
33 D.W. Jeong, W.J. Jang, J.O. Shim, H.S. Roh *Intern. J.Hydrog. Energ***. 41** (2016) 3870.
34 B. K. Kwak, D. S. Park, Y. S. Yun, J. Yi *Catal. Commun.* **24** (2012) 90.
35 T.A. Zepeda, B. Pawelec, A. Infantes-Molina, R.I. Yocupicio, G. Alonso-Núñez, S. Fuentes, J.N. Diaz de León, J.L.G. Fierro, *Fuel* **158** (2015) 405.
36 W. Tong, A. West, K. Cheung, K.M. Yu, S.C.E. Tsang, *ACS Catal.* **3** (2013) 1232.